Czech Technical University in Prague
Faculty of Electrical Engineering
Department of Control Engineering

Vehicle-Road Safety and Stability Envelope Definition and Protection

Disertation thesis

Ing. Denis Efremov

Ph.D. programme: Electrical Engineering and Information Technology
Branch of study: Control Engineering and Robotics
Supervisor: Doc. Ing. Tomáš Haniš, Ph.D.

Prague, March 2024

Thesis Supervisor:
Doc. Ing. Tomáš Haniš, Ph.D.
Department of Control Engineering
Faculty of Electrical Engineering
Czech Technical University in Prague
Karlovo náměstí 13
121 35 Prague 2
Czech Republic
tomas.hanis@fel.cvut.cz

Copyright © March 2024 Ing. Denis Efremov

Declaration

I hereby declare I have written this doctoral thesis independently and quoted all the sources of information used in accordance with methodological instructions on ethical principles for writing an academic thesis. Moreover, I state that this thesis has neither been submitted nor accepted for any other degree.

In Prague, March 2024

.....

Ing. Denis Efremov

Abstract

Comparing the history of aerospace and ground vehicles, one can admit the fast growth in the complexity and computerization of aircraft during the past seven decades. This growth is based on the high cost of each aircraft and its pilot and money flow for research purposes during the Cold War. These key factors matured the aerospace industry, increasing aircraft's agility and complexity and introducing control algorithms to reduce the burden from pilots and their mistakes or failures.

On the other hand, ground vehicles have slowly started to mature in the past three decades, when the first safety algorithms, such as anti-locking braking systems, were introduced as necessary equipment for each produced vehicle. Cars are going the same way of improvement, as the aircraft did: from X-by-wire systems, through over-action of platforms (where it has more ways of actuation per degree of freedom, i.e., independent steering, braking, and driving) and definition of safety envelope (where the vehicle dynamics is not compromised and its surrounding does not make any harmful danger) to envelope protection algorithms (which enhance human operations to increase the vehicle safety and stability).

This dissertation aims at the last two steps. It defines the vehicle-road envelope and introduces control algorithms to protect its boundaries. The vehicle-road envelope is strategically divided into two main parts: driving and environmental envelopes. The former defines states in vehicle dynamics space, where each wheel will not be locked, overspun, or skidding. The latter defines safe operational positions, where each wheel can be placed to avoid road departure, collisions with other road users, and drivable road irregularities, such as potholes or small objects on the road. The envelope definition is wheel-centric, allowing the utilization of this concept for any car (or any other wheeled platform) configuration.

The driving envelope protection algorithm can be used as an integrated controller, which does the functionality of an anti-locking braking system, traction control, electronic stability program, and launch control systems. In the same way, the environmental envelope protection algorithm can be used as an integrated lane-keeping and collision-avoidance system. However, it can also be used for semi-automated driving on regular and off-road roads.

Abstrakt

Srovnáním historie leteckých a pozemních vozidel lze konstatovat rychlý růst komplexity a počítačového řízení letadel během posledních sedmdesáti let. Tento růst vychází z vysoké ceny každého letadla a jeho pilota a finančních toků na výzkumné účely během studené války. Tyto klíčové faktory v leteckém průmyslu vedly k zvyšení agilitu a složitosti letadel a zavedení řídicích algoritmů sloužících k redukci zátěže pilotů a tím redukci jejich chyb či selhání.

Na druhou stranu se pozemní vozidla začala pomalu rozvíjet v posledních třech desetiletích, kdy byly poprvé zavedeny bezpečnostní algoritmy, jako jsou antiblokovací brzdové systémy, jako nutné vybavení pro každé vyrobené vozidlo. Automobily jdou stejnou cestou zlepšení jako letadla: od X-by-wire systémů přes přeaktuované platformy (kde je počet aktuátorů větší, než je potřeba pro řízení, tj. nezávislé ovládání, brzdění a pohon kol) a definování bezpečnostní obálky (kde dynamika vozidla není ohrožena a jeho okolí nepředstavuje žádné nebezpečí) až po algoritmy ochrany obálky (které zlepšují lidské operace pro zvýšení bezpečnosti a stability vozidla).

Tato disertace si klade za cíl poslední dva kroky, definuje obálku vozidlo-silnice a zavádí řídicí algoritmy k ochraně jejích hranic. Obálka vozidlo-silnice je strategicky rozdělena do dvou hlavních částí: řídíci a dopravního prostředi. První určuje stavy v prostoru dynamiky vozidla, kde každé kolo nebude zablokováno, přetáčeno ani nebude klouzat. Druhá část definuje bezpečné operační pozice, kde lze každé kolo umístit tak, aby se předešlo vyjetí ze silnice, kolizím s ostatními účastníky silničního provozu a jízdním nepravidelnostem, jako jsou díry nebo malé předměty na vozovce. Definice obálky se provádí vzhledem ke kolům, což umožňuje využití tohoto konceptu pro konfiguraci jakéhokoli automobilu (nebo jakékoli jiné platformy na kolech).

Algoritmus ochrany řídící obálky lze použít jako integrovaný kontrolér, který plní funkci protiblokovacího brzdového systému, trakčního řízení, elektronického programu stability a systémů řízení rozjezdu. Stejně tak algoritmus ochrany obálky dopravního prostředi lze použít jako integrovaný systém udržování jízdního pruhu a vyhýbání se kolizím. Nicméně může být také využíván pro polo-automatizovanou jízdu na běžných vozovkách i v terénu.

Keywords: Anti-lock braking system, driving envelope, electronic stability control, environmental envelope, obstacle avoidance, optimal control, traction control, vehicle dynamics, vehicle safety

Klíčová slova: Protiblokovací systém, řídící obálka, elektronický stabilizační systém, obálka dopravního prostředi, vyhýbání se kolizím, optimální řízení, řízení trakce, dynamika vozidla, bezpečnost vozidla

Acknowledgements

The genesis of this dissertation sprouted from a dialogue between two individuals, Martin Hromčík and Tomáš Haniš, years ago. Their discourse revolved around aircraft safety and stability systems and the noticeable missing equivalents in the automotive sector. It was this very conversation that kindled the flame of motivation, propelling the inception of this work.

Unlike many other dissertation endeavors, this project benefited from the guidance of two supervisors: a former ex-mentor, Martin, with a keen eye on the aviation industry, and a primary supervisor, Tomáš, deeply immersed in the dynamics of today's automotive industry. I express my heartfelt gratitude to both for providing me with such a remarkable opportunity, for recognizing my potential, and for creating an environment conducive to my self-realization.

However, the lion's share of my acknowledgment goes to Tomáš as the crux of this work unfolded under his mentorship. Our initial encounter transpired when I was a student, and he was my industrial co-supervisor. Following a profound discussion about his project vision, the essence of this dissertation materialized in a laconic way: "Formulate an envelope in which the car would be safe, akin to the security measures we currently have for aircraft." I extend my sincere thanks to Tomáš for his unwavering motivation, infectious humor, and knack for being both supportive and attentive, not just as a supervisor but as a true friend.

A debt of gratitude is also owed to our co-author, Martin Klaučo, whose academic expertise significantly influenced the technical realization of this work, shaping not only its substance but also refining my academic writing.

I reserve appreciation for another individual, Michal Kvasnica, whose brief yet incredibly fruitful discussions played a pivotal role in enhancing the theoretical and mathematical understanding of the model predictive control, its basis, and genesis.

Acknowledging the indispensable role of financial support in scientific research, I extend my thanks to Toyota Motor Europe for enabling this research journey. Special gratitude is directed towards Jiří Matas from the CTU side and Nikolay Chumerin from the TME side; this research would not have been feasible without their collaboration.

No endeavor is possible without the invaluable influence and feedback of colleagues who shape one's perspective and contribute to the refinement of their work. In expressing my gratitude to my co-workers, I extend my thanks to David Vošahlík, Vít Cibulka, Jan Švancar, Jaroslav Tabaček, and the entire Department of Control Engineering, as well as the Toyota Research Lab within the Department of Cybernetics. Their collaborative efforts have prevented me from feeling isolated on this journey. A special acknowledgment is reserved for our dedicated technical and administrative staff, who navigate the intricacies of the bureaucratic and challenging world of paperwork.

A heartfelt thank you is directed towards those individuals who have played an instrumental role in shaping my identity – my family. Their unwavering educational, moral, and motivational support from the inception of my life leaves me momentarily speechless. Without their life-altering decisions, it would be inconceivable to envision the person I am, the way I think, and the life I lead. Мои дорогие мама, папа, брат, бабушки, дедушки, тётя и все мои родственники, большое вам спасибо за то, что вы есть!

Furthermore, I extend my gratitude to all my friends and close associates scattered across the globe, who have been steadfast companions throughout every phase of my life. Despite the physical distance that may separate us, their enduring presence has played a pivotal role in shaping my personality.

Last but certainly not least, I want to express a heartfelt thank you to someone I hold dear – Alina, the person I love. Your enduring presence throughout this extended period has been a source of immense gratitude. Thank you for profoundly shaping and enriching my life!

Contents

List of Tables

List of Figures

Chapter 1

Introduction

Motor vehicles, including but not limited to personal vehicles, trucks, buses, motorbikes, and other motorized vehicles, are widely used as a means of transportation worldwide. In the United States, personal transportation, which includes automobiles and light trucks, accounts for approximately 87 % of passenger miles traveled in 2020 [1]. Additionally, the vehicle miles traveled (VMT) increase linearly with population [1]. The number of produced personal cars continues to rise yearly [1]. For example, the total number of personal and commercial cars is already over 100 million registered vehicles in the United States alone in 2023 [2].

The use of motor vehicles for transporting both humans and cargo provides a high level of convenience. However, it also comes with a significant cost in terms of road accidents, human injuries, and fatalities. In the United States alone, ground vehicle accidents accounted for 95 % of the total 40851 deaths in 2020 [3]. Consequently, regulatory agencies and car manufacturers have implemented various safety measures over the past few decades to address this issue. These measures include the reduction of alcohol consumption before driving, the use of safety belts, electronic stability control, improved materials, collision avoidance, and many more. These steps aim to ensure all traffic actors' safety and can be broadly classified into three main groups: law regulations, passive safety, and active safety systems.

This thesis focuses on active safety and stability systems. Similar inspiring analogies can be found in the aerospace industry and traced back to the emergence of aircraft, particularly fighter jets, where the aircraft's dynamics became too rapid for a human to control. Concurrently, advancements in electronics and computers made it possible to delegate tasks from the pilot to the machine, combining human intelligence with the fast computational capabilities of processors. The aerospace industry and control theory's development resulted in agile aircraft and improved civil aviation safety, significantly reducing the accident rate per million flights [4].

The implementation of active safety and stability systems for regular cars can be traced back to the introduction of the first antilock braking system (ABS) in 1990 [5]. This safety system set a precedent for certification authorities to mandate car manufacturers to equip all vehicles coming off the production line with this technology in the late 1990s. While statistics show a reduction of non-fatal crashes of up to 8 % due to the implementation of ABS, at the same time, “ABS has close to a zero net effect on fatal crash involvements" [6]. The next major technological advancement in safety systems was the electronic stability program (ESP), which has been shown to significantly reduce the number of crashes by up to 36 % for passenger cars and 70 % for light trucks and vans (LTVs) [7]. Overall, ESC reduced all fatal crashes by a statistically significant 14 % for passenger cars and 28 % for LTVs [7]. The group of active safety and stability systems is not limited only to safety systems but also contains comfort-increasing assistance, for instance, such as cruise control, which was introduced in 1970 [5]. Such approaches can increase safety through the reduction of the driver's workload and fatigue using automation techniques. Today, the list of safety systems contains dozens of names and abbreviations. Each system aims at addressing a specific problem related to vehicle dynamics or interaction with the vehicle's surroundings and the driver [8].

The increasingly diverse range of advanced driver assistance systems (ADASes) presents significant challenges for control engineers regarding the integration of their functionalities. However, a novel paradigm for ADASes development, which proposes the implementation of fully software-based systems, has been suggested as a potential solution by Apex.ai company [9]. This approach would allow for the development of more sophisticated and integrated vehicle control structures directly in the software, not in separate hardware, leading to improved product performance. The objective of this thesis is to develop a universal stability and safety system architecture that encompasses the functionalities of current stability systems while enhancing driving safety. This system aims to provide a unified operational framework for cars, thus addressing the challenges of integrating multiple ADASes while improving the overall driving experience. However, before discussing such ideas in automotive, one can get inspiration from the aerospace industry.

1.1 Motivation from Aerospace Industry

The analysis of ground vehicle dynamics and the potential benefits of automation and safety systems can be inspired by examining the aerospace industry, particularly airplanes, and its historical changes. Despite the differences between cars and airplanes, there are significant similarities, such as the principles of their physical modeling. Both models

start with approximating both bodies as mass points, with the center of gravity being the first “point of interest." Additionally, the center of applying forces acting on the body is a second “point of interest," known as the aerodynamic center in the case of aircraft and the center of wheelbase in the case of cars (Fig. 1.1). The position of this second point with respect to the first affects the static stability properties of both aircraft [10] and car [11], making them either statically stable or unstable. Furthermore, both dynamics are highly nonlinear, mainly because of the highly nonlinear dependency of generated forces acting on control surfaces or wheels on the systems' state vector.

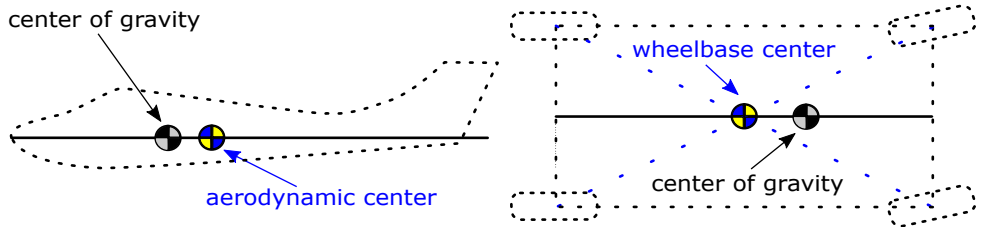

Figure 1.1: “Points of interest" for statically stable airplane and car dynamics.

However, the primary difference between those two systems is the overall simplicity of ground vehicle dynamics compared to aircraft. Ground vehicles have fewer significant degrees of freedom, with only three compared to the six for airplanes (moving in the vertical direction, rolling, and pitching are very limited for a typical car). Similarly, a common car has fewer actuators than an aircraft, with only throttle, brake, and steering, compared to an aircraft's thrust, elevators, ailerons, and rudder. This leads to a more complex control effort for a trained pilot to control the vehicle, with the human factor being a more frequent reason for crashes. Moreover, the cost of a trained pilot and an aircraft, together with the system dynamics difficulty, were two main reasons for introducing flight control strategies for active safety and stability systems of civil and military airplanes.

In the aerospace industry, a series of crucial steps were taken to introduce active safety systems into airplanes. The first step was the introduction of fly-by-wire technology, which allowed the disconnection of the mechanical connection between the airplane's actuators and control elements in the pilot cabin, wiring them through the control computer. This upgrade permitted the addition of control signals to a pilot's action, which helps in the handling of the aircraft. Fly-by-wire also allowed the addition of new control surfaces on an aircraft, making the dynamics more complex and opening other combinations of control inputs to reach the same target state of the aircraft dynamics. Such augmentation of the systems allowed control engineers to optimize the vector of control inputs, increasing the airplane's maneuverability and introducing control redundancy for the system operation.

At the same time, the theory of aircraft stability evolved with the introduction of safety

envelopes, called flight envelopes. These envelopes create boundaries on the state-space of the dynamical model of the aircraft, inside which, for the particular airplane, safety and performance margins can be guaranteed. Those envelopes must be investigated before the first flight of any new model of the aircraft to establish limits in which handling qualities, engine behavior, structural load, and many other aspects remain acceptable [12].

The last and most valuable step was the introduction of full-time-full-authority control strategies. The control computer relentlessly controls the pilot's actions and follows their command until the safety requirements of any flight envelope are not violated. If it happens, the controller will override control signals to stabilize the airplane. These steps significantly reduced failures in the aerospace industry, making civil aircraft much safer than they were a few decades ago [4].

Full-time-full-authority control is a concept that has been mainly realized through the implementation of flight envelope protection schemes in aviation. Two main strategies have been proposed to provide such protection: hard and soft. In hard protection, the control computer has full authority over the pilot's action, and the pilot cannot exceed envelope boundaries, as implemented in Airbus's airplanes [13]. In contrast, soft protection strategies allow pilots to override the signals from the control computer with extra effort, as utilized by Boeing [13]. The choice between the two strategies depends on the specific requirements of the aircraft and the level of control authority desired.

The automotive industry has also made comparable progress in improving safety. One of the crucial steps in improving automotive safety is the introduction of drive-by-wire systems. The drive-by-wire systems include steer-by-wire, throttle-by-wire, brake-by-wire, and others. These systems are already complained by the ISO 26262 standard [14], which provides guidelines for the functional safety of road vehicles. The drive-by-wire technology may be used in different production models for various active safety and stability systems, such as ESC, adaptive cruise control (ACC), and lane assist systems (LAS). Many car manufacturers have implemented over-actuation of the car, which includes but is not limited to independent braking, driving, and steering of wheels. The analogies of the flight envelope and full-time-full-authority control concepts are also described. Those crucial steps are the subject of this work and will be considered in the following sections.

The vulnerability of cars to their environment, in addition to their dynamics, presents a significant challenge to the integration of active safety measures into everyday use. Unlike airplanes, cars are heavily influenced by their surroundings, including the road, weather, and other vehicles. This challenge has led the car industry to introduce a roadmap for the development of ground vehicle automation. The Society of Automotive Engineers (SAE) has proposed a set of “Levels of Driving Automation" to guide the gradual integration of active safety measures into cars. The discussion of the SAE's Levels of Driving

Automation is presented in the following section.

1.2 About Levels of Automation in Automotive

Driving automation in vehicles has been a topic of great interest in recent years. With technological advancements, the automotive industry has been working towards achieving higher levels of automation in vehicles. The automotive industry discusses the six levels of driving automation, as defined by the Society of Automotive Engineers (SAE), depicted in Fig. 1.2.

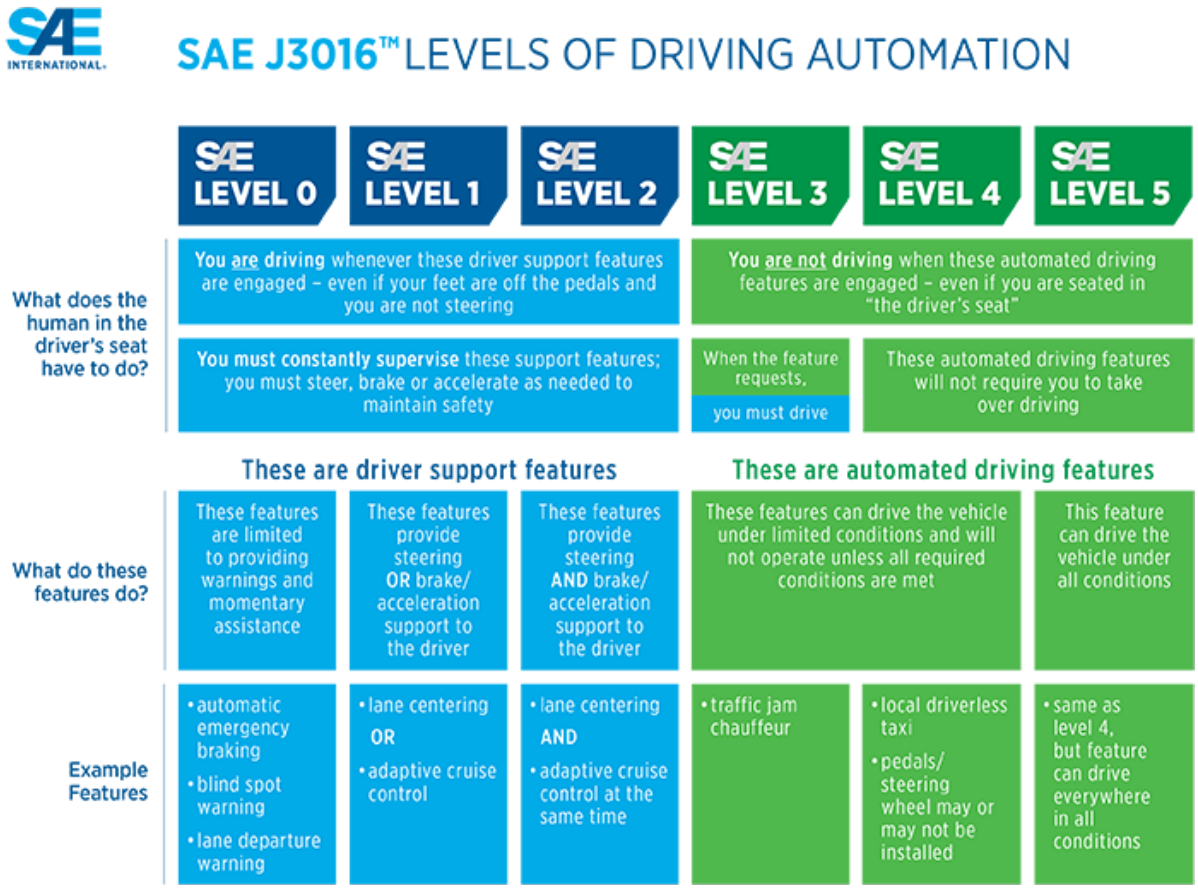

Figure 1.2: SAE J3016 standard for levels of driving automation [15].

Level 0, also known as No-Automation, is characterized by the driver having complete control over the vehicle's steering, brakes, and throttle. The driver is solely responsible for monitoring road conditions, responding to potential hazards, and ensuring safe vehicle operation. If present, any driver assistance systems are limited to warning signals sent to the driver or small control actions, which can reduce some stability issues. This level includes ABS, lane departure warning, or other simple active stability or information systems.

Level 1 of vehicle automation is characterized by partial automation of certain primary functions. This level includes the addition of different assistance systems, such as the ACC or lane-centering, but these systems are not integrated and operate independently. However, if multiple assistance systems are present, they operate only with the particular dynamics of the vehicle. For instance, cruise control would have access to change the longitudinal dynamics of the vehicle and lane-centering to the lateral. At this level, the driver still has complete control over the vehicle's inputs but can partially delegate authority to an assistance system. Nevertheless, the driver remains responsible for monitoring road situations, reacting to hazards, and ensuring the vehicle's safe operation.

Level 2 of vehicle automation is similar to Level 1, but multiple assistance systems are integrated with the operating inputs. For instance, the ACC and lane-centering can operate simultaneously with knowledge of each other. However, in Level 2, control engineers have solved a hierarchy or priority logic when both assistance systems are activated and make access to the same control elements (pedals and the steering wheel). In limited situations, a driver can delegate control authority over a vehicle's input to the assistance systems. Nonetheless, the driver is still solely responsible for monitoring road conditions, responding to hazards, ensuring safe vehicle operation, and promptly taking control of the vehicle.

Level 3 of vehicle automation involves more significant reliance on automation under certain well-defined circumstances. The assistance systems take complete control of the vehicle in specific scenarios, but the driver is expected to take control of the vehicle if certain predefined conditions are not met. For example, the latest model of the Audi A8 is equipped with a Traffic Jam Pilot [16], considered a Level 3 automation system. According to the manufacturer, this system can operate at speeds of up to $60\,\mathrm{km\,h^{-1}}$ and is designed to navigate the vehicle in traffic jams by taking actions such as starting, accelerating, and stopping the vehicle and keeping it within the lane. However, the driver must still be prepared to take control of the vehicle if the system encounters a situation it cannot handle. For such a level of automation, regulatory authorities mostly asked car manufacturers to be considered as responsible persons in the case of accidents. Therefore, the production of such systems is primarily limited because of such legislation restrictions.

Level 4 of vehicle driving automation involves a fully automated system that can operate the vehicle without needing a driver in limited-service areas. This level of automation can be found in areas outside of the automotive sector. For example, Amazon's automated warehouses [17] are an excellent example of Level 4 automation, where robots navigate the warehouse and complete tasks without human intervention. A Level 4 automation system example in the automotive sector is a driverless taxi in Singapore developed by NuTonomy (former name of Motional Inc. [18]). This taxi is designed to navigate Singapore's

small, campus-like business district without a driver. There are other examples of Level 4 automation systems worldwide, such as driverless taxis that are limited to operating in specific environments.

Level 5 of vehicle automation involves a fully automated system that can operate the vehicle in any environment and under any condition without the need for human intervention. In this level of automation, the vehicle does not require a steering wheel or any other human-operated controls. It operates entirely autonomously, and the human is merely a passenger. This level of automation is often depicted in science fiction works, where vehicles can operate without any human input and serves as the desirable but distant goal for the whole industry.

1.3 Related Existing Commercial Products

This section presents driving automation and safety systems, which are related to the topic of the vehicle-road envelope and its protection.

The list starts with the first mandatory safety system, the ABS. When a car is moving, applying the emergency brake can cause the front wheels to lock up, even if the vehicle is moving in a straight line, resulting in the car losing its steering capabilities. Conversely, if the rear wheels lock up, the car's braking stability will decrease, and even a slight lateral force can cause the car to spin out of control, as demonstrated in section 2.7. Additionally, the intense friction caused by wheel lock-up can significantly reduce the wheels' lifespan [19]. Anti-lock braking technology was developed to address these issues. The implementation of ABS systems uses different control approaches that must be robust against uncertainties associated with the varying friction properties of the drivable surface and work in real-time, as these criteria apply to any safety system used in the automotive industry. From a control theory perspective, ABS implementations are generally as simple as possible, using methods such as logic threshold value, PID or fuzzy control for slip ratio control, and sliding mode control [19], [20]. Nevertheless, scholars are implementing already more complex and challenging control structures and methods to fulfill the ABS functionality, such as model predictive control, linear quadratic regulators, and neural network controllers [21].

On the flip side, unwanted vehicle behavior can occur not only during braking but also during acceleration. When compared to the braking process, during vehicle acceleration, if the driving force is too high or the road surface's adhesion coefficient is too low, it can cause the driving torque to exceed the adhesion limit between the tire and the road surface, leading to excessive slip of the driving wheels as experimentally shown in section 2.7. If this slip phenomenon occurs, it can decrease the vehicle's driving performance, increase

the load on the transmission system, and consume more fuel while also reducing the vehicle's handling performance in the lateral direction. Traction control systems (TCS) can address these problems as an extension of the ABS concept in the car driving process. TCS aims to decrease the driving torque of the driven wheels to decrease their slip ratio. There are two main strategies to provide a functionality of the TCS systems – a reduction of the driving torque from its source (reducing fuel injection or using a clutch) or using braking torque applied by brakes (which is inefficient). The control methods used for the implementation of the traction control are mainly the same as for ABS and can be found in [19], [22].

The electronic stability program (ESP) is an extension of ABS and TCS with improved algorithms to address lateral vehicle stability issues. The first concepts enabled the direct control of vehicle yaw movement (DYC) [23]. DYC determines the driver's steering intention by collecting steering wheel angle information and handles the vehicle's yaw movement by allocating braking force or driving force to the wheels. Other implementations of ESP [24] determine the vehicle's yaw moment using the error of state feedback between the vehicle's actual and ideal motions and adjust the vehicle's yaw movement by differential braking or engine control. That strategy has become a widely used modern control method in vehicle stability control. Researchers have also tried to use modern control theory methods to control vehicle stability and have obtained some promising results. These methods include fuzzy control theory, sliding mode control, nonlinear model predictive control, and active front wheel steering control of autonomous vehicles based on the model predictive control method [19].

The previous vehicle safety and stability systems were designed to ensure the safety and stability of the vehicle. The second group of technologies focuses on driving automation, with the goal of enhancing vehicle safety in the environment. This group's first type of system is the lane-keeping assistance (LKA) system. Vision-based lane-keeping has various implementations [25]. However, the basic concept is to identify the lane markings, estimate the lane boundary, and track that boundary using steering and/or braking control laws [26]. For example, Volvo's LKA solution [27] uses a camera to read the sidelines of the road or lane. If the vehicle is about to cross a sideline, LKA applies a slight steering torque to steer the car back into the lane. If the car reaches or crosses a sideline, LKA alerts the driver through vibration in the steering wheel [27].

Collision avoidance systems are a vital component of autonomous and highly-automated vehicles. In the general robotic field [28], collision avoidance algorithms are typically divided into two stages: perception and action. During perception, data from various active and passive sensors are fused to inform the system of the surrounding environment. During the action stage, a collision avoidance algorithm determines the appropriate response

to avoid a collision. Two major collision avoidance systems have been developed within the automotive industry: brake-assist and steering-assist avoidance systems [29]. Brake-assist systems utilize the brakes to prevent collisions by stopping or slowing the vehicle, while steering-assist systems use steering to perform an evasion maneuver. Trajectory and path planning and tracking are crucial to successful collision avoidance, with the output trajectory being optimized to be safe and collision-free with other objects on the road. Various techniques have been developed to accomplish this task [30], including model predictive control techniques [31] and minimum violation planning [32]. Both approaches have their advantages and disadvantages, which are discussed in-depth in [33]. Moreover, such control techniques can be utilized not only as collision avoidance systems but as auto-pilots from the higher levels (3-4) of automation.

In the realm of commercial products, Toyota Guardian and Toyota Chauffeur systems [34] are noteworthy examples that are currently under development and still need to be made available for purchase. The Toyota Guardian system is inspired by flight envelope protection schemes and is designed as an advanced driver assistance system to enhance vehicle safety during human-operated driving. On the other hand, the Toyota Chauffeur system is Toyota's driving concept for autonomous and semi-autonomous driving. Both systems utilize the environmental and handling envelopes, which are discussed in the next section analyzing the state-of-the-art in the literature.

1.4 State-of-the-Art in the Literature

The objective of this thesis is to define the vehicle-road envelope and suggest its protection algorithms using model predictive control techniques. The concept of envelope protection was originally developed in the aerospace industry but has since been adapted for advanced driving assistance systems in the automotive control field. Scholars have made significant contributions to this area, particularly in the development of blended (shared) control and semi-autonomous driving systems. Vehicle-road envelopes can be categorized into two main groups based on the problems they address: stability envelopes and environmental envelopes.

The concept of stability envelopes was initially introduced in a study [35], which outlines a stable region in the phase plane based on vehicle states. The authors selected vehicle sideslip and sideslip rate as the phase plane variables for their analysis because these variables have relatively low variability with vehicle speed and are intrinsically linked to vehicle stability. The sideslip is defined as the angle between the vehicle's heading and velocity vector, as illustrated in Figure 2.1. The authors suggested that an open region between the saddle points of this phase plane could serve as a safe envelope for vehicle

stability. They supported this proposal with experimental results that utilized a direct yaw moment control system to enforce safe envelope protection.

In [36], several types of stability envelope definitions were mentioned. However, the most widely-used stability envelope was described in Craig Beal's doctoral dissertation from 2011. Beal's work [36] proposes different types of handling envelopes, which are produced by performing phase plane analysis on a nonlinear single-track model. The author recommends using the sideslip angle and yaw rate (planar rotational velocity around the center of gravity) to define the handling envelope. Those variables are the general states for lateral vehicle dynamics description (when the vehicle's constant speed is held fixed). The boundary of this envelope is depicted in Figure 1.3. That work also suggests a model predictive control for envelope protection. Its primary objective is the prevention of the violation of the handling envelope boundaries by using the steer-by-wire technology and augmentation of the commanded steering angle from the driver. The functionality of the suggested control law was experimentally verified.

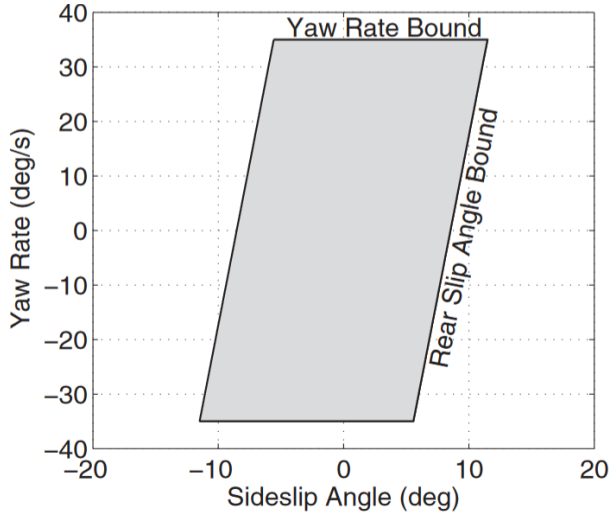

Figure 1.3: Handling envelope boundaries used in [37].

The handling envelope has found widespread use in various applications. Some researchers have combined it with rollover prevention for over-actuated platforms [38] and the environmental envelope, which is the second part of the vehicle-road envelope. The environmental envelope is designed to provide the controller with information about the surroundings, including the road and other primarily static objects. Early proposals involved creating safe trajectories for the vehicle that excluded collisions with obstacles and road boundaries. Different works have been developed for trajectory generation, with the winner of the DARPA Grand Challenge [39] being one of the earliest. Their solution attempted to minimize interference with obstacles, avoid leaving the lane, and minimize deviation from the base trajectory while adhering to the vehicle model's kinematic and dynamic constraints. The base maneuvers and final trajectory were defined as lateral offsets

from a fixed base trajectory that may not be obstacle-free. Other trajectory generation methods have used different primitives to analyze and describe safe, collision-free vehicle trajectories [40], [41]. Additionally, some approaches have moved away from the path or trajectory planning paradigm. For example, a shared control framework was introduced in [42], which divided all safe regions of the environment into homotopies. These homotopies are defined by the set of trajectories they contain, greatly facilitating trajectory generation. Although safe trajectories are generated, they are not tracked, and the controller continuously responds to the driver's inputs by computing a new trajectory at each time step. This way, the driver is not limited to a predetermined path, but they cannot move between homotopies and are restricted to operating within a single, heuristically determined homotopy.

Stephen Erlien's doctoral dissertation [43], published in 2015, introduced the concept of an environmental envelope. This envelope is defined by the obstacles and lane boundaries present in the vehicle's surroundings. Figure 1.4 from Erlien's work provides a clear illustration of this idea.

The algorithm presented below outlines the process for generating the environmental envelope. At the start, a collection of obstacles is identified along the reference line **(a)**. Next, the environment is discretized in the direction of motion s **(b)**, and objects are extended in the direction of motion to align with the discretization and identify feasible gaps between objects **(c)**. Finally, adjacent gaps are connected to form tubes (two in this example), which define the maximum and minimum lateral deviation from the reference line at each time step, k **(d)**. The resulting driving tube is then translated into the environmental envelope boundaries as the maximum possible deviations from the controller reference line inside the model predictive controller formulation.

This dissertation is inspired by previous research on the handling envelope [36] and environmental envelope [43], which aimed to define and protect these vehicle-road envelopes. The following section summarizes this thesis's specific contributions to this field.

1.5 Dissertation Contributions

Before summarizing the contribution of this dissertation, it is necessary to state its scope. The following structure of the decision-making process was admitted by analyzing a survey of motion planning and control techniques for self-driving urban vehicles [30], where most ideas can also be used for rural and highway road scenarios. The structure of overall autonomous driving can be divided into several parts, which can have some interconnections due to the way of chosen implementation, presented in Fig. 1.5. The structure contains the following four parts: route planning, behavior layer, motion planning, and local feedback

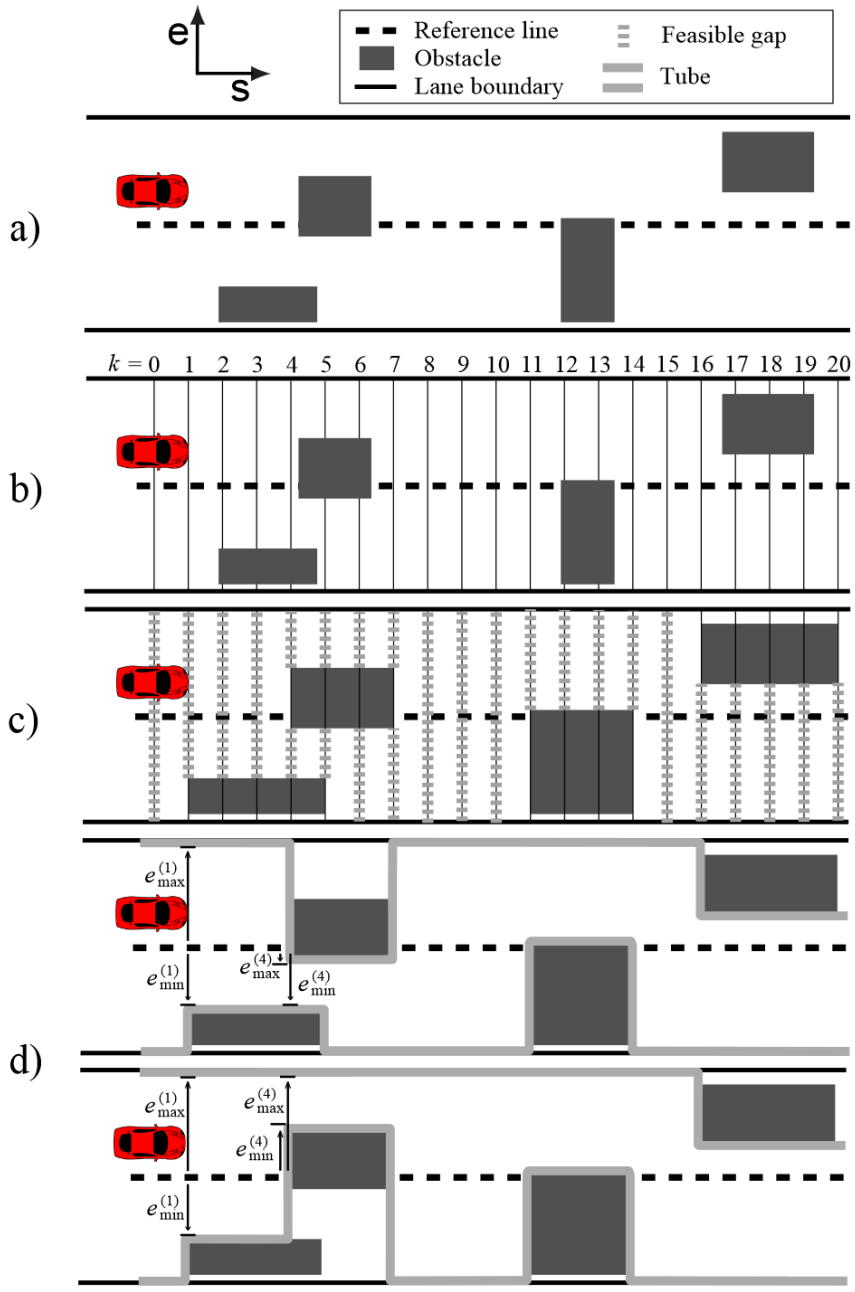

Figure 1.4: Formulation of the environmental envelope from [43].

control. Strategic planning is referred to as route planning, which determines the best route from point **A** to point **B** according to available connections, possible time and energy consumption, and many other aspects. The planned route as a sequence of waypoints is taken into account by the behavior layer, which tries to specify the vehicle motion by analyzing traffic behavior, traffic rules, signals from infrastructure, road conditions, and other effects, which are also considered by the human driver when following some route planned by the navigator (or by their head). Motion planning is responsible for generating some path or trajectory (= path, but with time specifications), which would be acceptable (feasible) for the vehicle, comfortable for passengers, and avoids collisions with obstacles.

At the bottom level, vehicle control is responsible for the execution of the reference path or trajectory dictated by the motion planning system. Typically, appropriate actuator inputs are selected by a feedback controller to carry out the planned motion and correct tracking errors, which can occur due to errors in planning (from the high-level planners) and inaccuracies of the vehicle model. Therefore, the overall robustness and stability of the closed-loop system must be increased by this level.

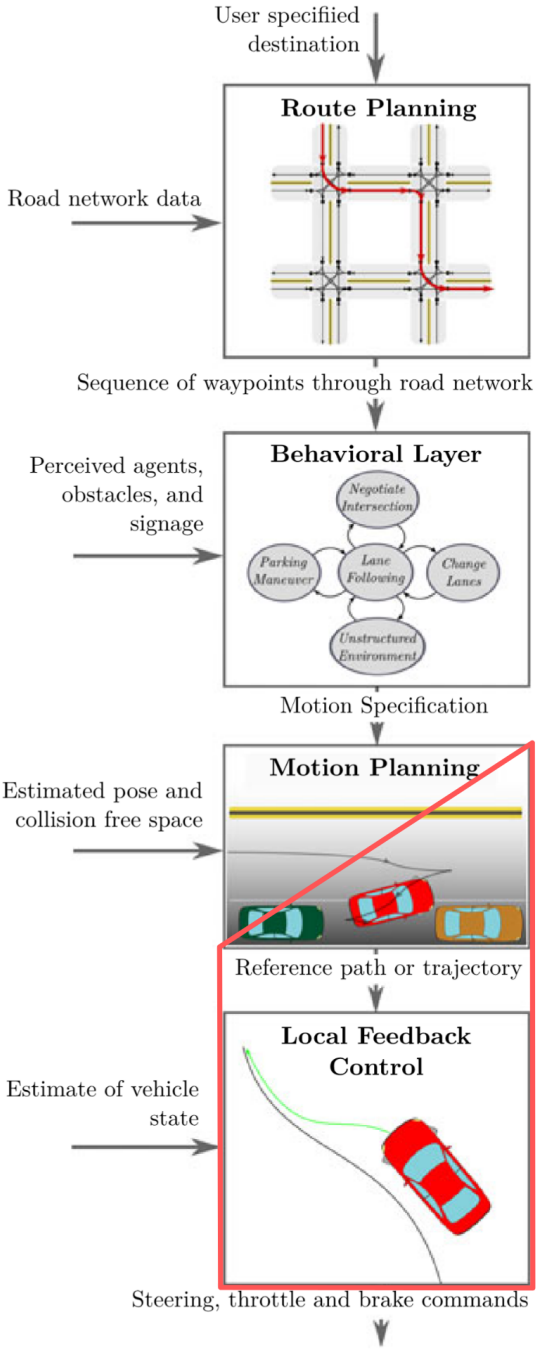

Figure 1.5: Illustration of the hierarchy of decision-making processes from [30] and the thesis's scope marked in red.

This thesis proposes control strategies suitable for local feedback control and partially

for motion planning design using terms from Fig. 1.5. The vehicle-road envelope defines vehicle stability and safety criteria in terms of wheel stability and safety, resulting in overall vehicle and maneuver safety. It is divided into stability and safety envelopes. The stability envelope, named the “driving envelope," is analogous to the “flight envelope" for aircraft. The environmental envelope, with a different definition than the one discussed in Section 1.4, is the other part of the vehicle-road envelope. Figure 1.6 schematically presents the general idea of the vehicle-road envelope.

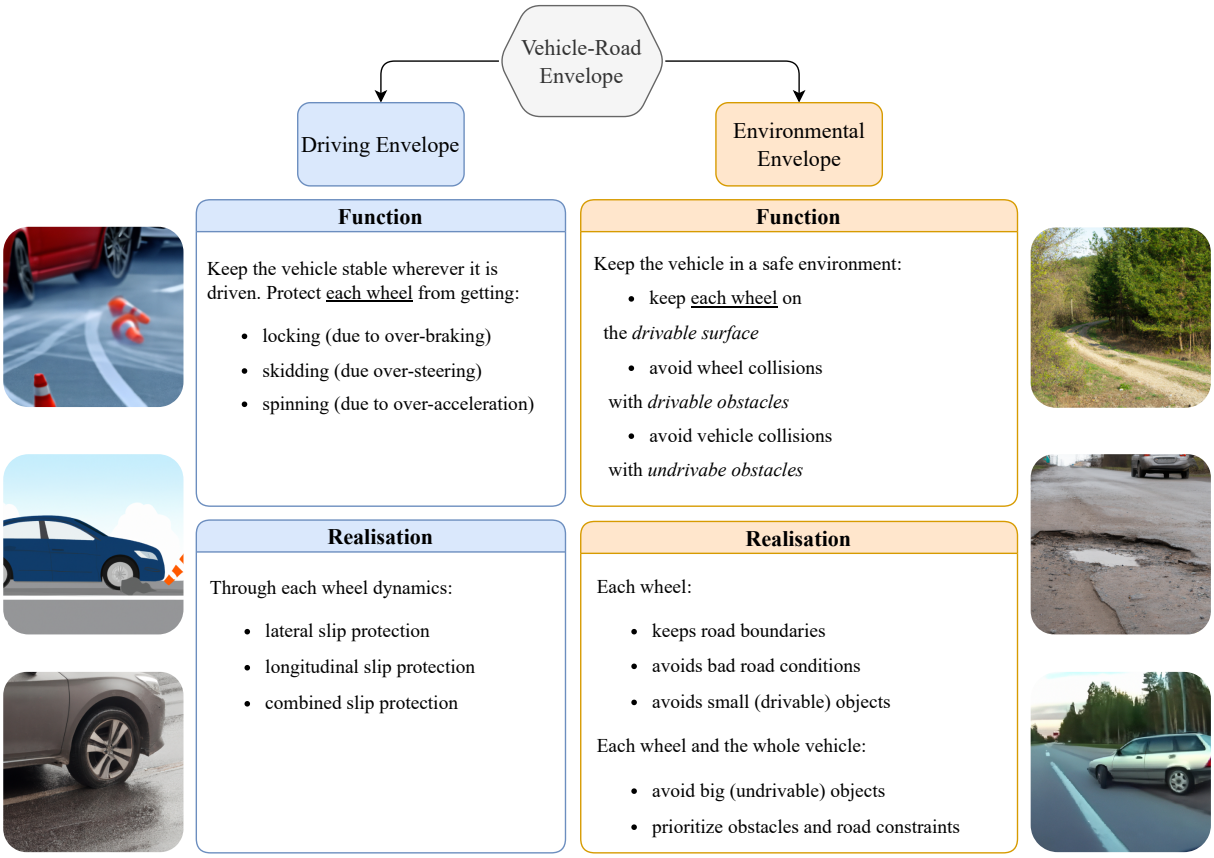

Figure 1.6: The vehicle-road envelope comprises the driving envelope, defining stability constraints, and the environmental envelope, outlining safety constraints from the surroundings. Figures are created with DALL·E 2 assistance.

1.5.1 Driving Envelope as a Definition of Vehicle Stability

The driving envelope defines stability criteria using traction limits for each subjected wheel. The constraints for vehicle dynamics are defined to ensure that each wheel’s lateral and longitudinal slip of driven and braked wheels will not exceed the traction capacities of tires. Longitudinal and lateral slip variables are combined into the combined slip to bind both dynamics in one set of equations, protecting each wheel from locking, skidding, and spinning. These effects mainly occur due to over-braking, over-steering, or

over-accelerating of a particular wheel. However, they can also result from a change in vehicle dynamics, such as a sharp turn.

According to the SAE specification, presented in Fig. 1.2, the driving envelope protection algorithm can be categorized into L1 and L2 groups, depending on its realization and dynamics, which are enhanced by it.

1.5.2 Environmental Envelope as a Definition of Vehicle Safety

In contrast, the environmental envelope defines a safe driving space for the vehicle. It utilizes the definition of a drivable road, a drivable obstacle, and an undrivable obstacle. A drivable road is a safe road where the vehicle can “put" each wheel, such as a highway lane or ruts on a rural forest road or show ruts. The drivable obstacle represents all objects that the vehicle can drive over, such as potholes, ice pads, stones, or other road irregularities that can lead to damaged wheels or discomfort for passengers. The undrivable obstacles represent all objects on the drivable road that are dangerous for the vehicle and cannot be driven over, such as other vehicles, pedestrians, and animals. This concept of obstacle definition allows for prioritizing obstacles within the control problem, making some undrivable obstacles more expensive (from the optimization point of view) than others or drivable ones. For example, a parked car must be avoided rather than a small pothole.

According to the SAE specification presented in Fig. 1.2, the environmental envelope protection algorithm can be categorized into the interval between L1 and L3, depending on its realization and dynamics, which are enhanced by it. The main realization provided in this thesis utilizes only the steering wheel; therefore, it can be addressed only as the L1 algorithm. However, both the driving and the environmental envelope protections are targeted to be parts of L4 automation systems, as they can increase the robustness and performance of the upper route, behavioral, and motion planning parts of any autonomous driving system.

1.5.3 Driving Envelope and Environmental Envelope Protection

This dissertation proposes several control architectures for driving and environmental envelope protection. These architectures include:

- Hard envelope protection strategy for combined driving envelope protection using model predictive control
- Soft envelope protection strategy for lateral driving envelope protection using model predictive control

- Control structure for hard lateral driving envelope protection using a hierarchical controller
- Strategy for hard environmental envelope protection

As mentioned, soft and hard protection strategies are commonly used in the flight industry to provide envelope protection. This work proposes mainly solutions that utilize the model predictive control approach, which is widely used in publications and has a suitable structure for defining desired behavior with various constraints on the resulting solution. The resulting controllers provide envelope protection in a hard way, where full authority is given to the control structure. Additionally, other control concepts that use different control formulations (hierarchical) or employ a soft envelope protection strategy are suggested.

The control strategies proposed in this dissertation can be used as cores for standalone advanced driving assistance systems or as a lower level of a more complex control structure. In the latter case, for example, a higher-level motion planner may suggest control inputs or a trajectory to be followed, which are then corrected by the environmental and then by the driving envelope protection algorithms before being applied to the vehicle's control system. This correction ensures that the control inputs are feasible and safe, given the current environmental and driving conditions. Moreover, both envelope protections theoretically can be combined in one optimization problem in the same way, as it was proposed for the handling and environmental envelopes in [43].

1.6 Dissertation Outline

This dissertation thesis presents the definition of the driving and environmental envelopes and introduces different possibilities for their protection. The remaining chapters are organized as follows:

Chapter 2: Driving Envelope

The driving envelope and its protection algorithms are introduced in the second chapter. The generation of traction forces, dependent on wheel dynamics and kinematics, is analyzed, and the resulting effects on vehicle dynamics are derived. The driving envelope protection is primarily provided as a hard envelope protection strategy through linear model predictive control. Additionally, other methods for driving envelope protection are described, such as the utilization of a hierarchical structure controller to safeguard the lateral driving envelope and the application of haptic torque to communicate with

the driver as part of soft envelope protection strategies. Simulation experiments using high-fidelity vehicle dynamics simulators are employed to verify each control strategy.

Chapter 3: Environmental Envelope

In the third chapter of this thesis, the environmental envelope is defined by establishing a safe space from the perspective of the wheels. Essential formulations that contribute to the definition of the envelope are presented. Additionally, the chapter introduces the concept of nonlinear model predictive control for protecting the environmental envelope. Simulation experiments utilizing a high-fidelity vehicle dynamics simulator are conducted to evaluate the performance of this control law in different driving scenarios and verify its functionality.

Chapter 4: Conclusion

In conclusion, the dissertation includes an assessment of the envelope control framework that has been introduced in the preceding chapters. Additionally, it delves into a conversation about potential future advancements and avenues for further research.

Chapter 2

Driving Envelope

This chapter introduces the driving envelope and algorithms for its protection. The driving envelope protection is mainly provided as a hard envelope protection strategy by the linear model predictive control. Although section 2.8 describes other methods for driving envelope protection. Namely, using a hierarchical structure controller to protect the lateral driving envelope and using soft envelope protection strategies to apply haptic torque to communicate with the driver. Most of this chapter was submitted and accepted in the IEEE Transactions on Intelligent Transportation Systems in 2024 [44].

2.1 Introduction

The envelope protection framework presented in this chapter uses the driving envelope stability concept. The driving envelope is a methodology of the stability boundaries definition over the vehicle state-space. Such sub-space excludes unstable vehicle maneuvers from the wheels' perspective. This envelope incorporates each tire's lateral, longitudinal, and combined slip dynamics. In other words, the driving envelope excludes vehicle states where each wheel could become locked, overspun, or skidding. Such boundaries in a finite number of steps could become the maximum control invariant set, which is shown later in this chapter. Theoretically, it can guarantee future vehicle stability by preserving driving envelope boundaries. The driving envelope concept is based on analyzing tire traction dependencies on wheel slip variables. By limiting these variables and defining a desired region for each slip variable for each wheel, the driving envelope can be designed. Those ideas were used in [45], where the author decided to create an envelope based on the limits of the sideslip angle of wheels.

The proposed envelope protection strategy follows the driver's steering wheel and throttle and brake pedals commands as closely as possible while preserving the safety limits of the driving envelope. It utilizes braking and accelerating commands with con-

stant torque distribution over wheels and front-wheel steering, representing a conventional car. However, control architecture could be easily augmented to any car configuration. The highest benefit of the presented method would be advantageous, especially as an application in over-actuated vehicle platforms, where each wheel could be driven, braked, and steered individually.

The methodology presented guarantees the preservation of vehicle stability while systematically preserving the controllability of each wheel. The control law derived in this chapter provides the functionality of an anti-lock braking system, electronic stability program, traction control, and launch control systems in one optimal control problem. Therefore, there is no need to solve any system hierarchy between those stability systems. There is only one priority, which is solved easily by changing weights between lateral and longitudinal dynamics in the MPC (how close the controller has to follow commanded steering or change in angular velocity of the driven wheels). The resulting controller allows a control engineer to adjust vehicle response by changing the driving envelope boundaries. That could be used to define different vehicle behavior for different scenarios.

The following is the structure of this chapter. Section 2.2 outlines the vehicle model used by controllers. Section 2.3 provides an analysis of tire traction forces as a prerequisite for understanding the driving envelope definition presented in section 2.4. Section 2.5 discusses how to select driving envelope boundaries. Section 2.6 presents the MPC formulation for driving envelope protection for a conventional car. Section 2.7 presents the experiments conducted and provides a detailed discussion of the results. Section 2.8 explores different possibilities for utilizing the driving envelope in various control structures. Finally, the concluding section summarizes the topic of the driving envelope.

2.2 Vehicle Dynamics

The synthesis of any model-based control relies on the dynamical model of the operational subject, which is derived in this section. As stated above, this work assumes a conventional car model with front-wheel steering, with constant braking and driving torque distribution.

A diagram of the single-track model is presented in Fig. 2.1, while all model parameters and variables are listed in Table 2.1. A second-order model of lateral vehicle dynamics is considered. It describes the vehicle's lateral and rotational planar dynamics. The model utilizes small sideslip angle $\beta \approx 0$ and constant longitudinal speed $v = \text{const}$ assumptions and lumps both wheels on each axle together. The equations of motion are given as

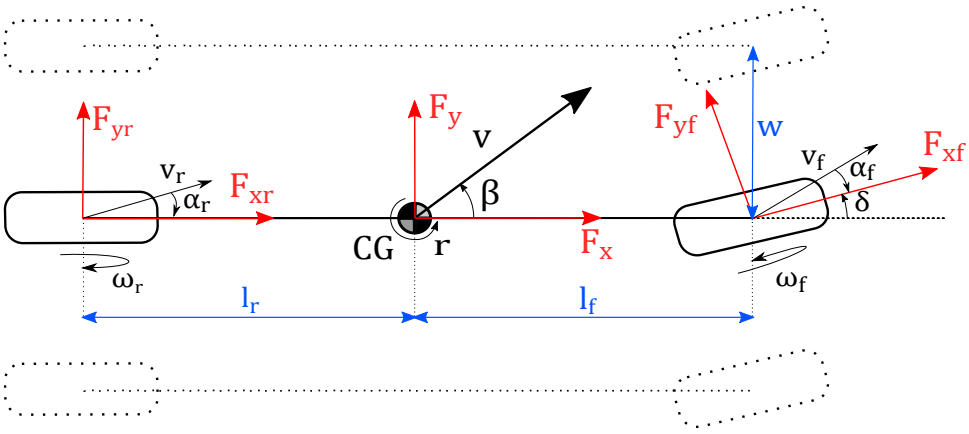

Figure 2.1: The single-track model.

follows,

$$mv(\dot{\beta} + r) = F_{\mathrm{yf}} + F_{\mathrm{yr}}, \tag{2.1a}$$

$$I\dot{r} = l_{\mathrm{f}}F_{\mathrm{yf}} - l_{\mathrm{r}}F_{\mathrm{yr}} \tag{2.1b}$$

where the right-hand side of (2.1) presents the lateral force acting on the center of gravity of the vehicle (CG) and the resulting rotational torque applied at CG. The linear single-track model assumes constant speed. Therefore, both axles' traction forces acting in the longitudinal direction are neglected ($F_{\mathrm{xr}} = F_{\mathrm{xf}} = 0$). This linear single-track prescribes only the lateral dynamics of a vehicle. However, the longitudinal dynamics of wheels is also considered in the envelope protection scheme but not in the prediction model. It is done to reduce unnecessary model computations because the utilized control strategy operates on a small prediction horizon, on which changes in the vehicle speed can be considered as model inaccuracy. The linear approximations of wheel lateral traction forces are provided using the nominal cornering stiffness of a tire $c_{\alpha i}$, load force acting on an axle $F_{\mathrm{z}i}$, and sideslip angle of an axle α_i as,

$$F_{\mathrm{y}i} = c_{\alpha i}F_{\mathrm{z}i}\alpha_i \tag{2.2}$$

for both front and rear axles, hence $i \in \{\mathrm{f}, \mathrm{r}\}$. Linear approximations of sideslip angles are given as

$$\alpha_{\mathrm{f}} = \delta - \beta - \frac{l_{\mathrm{f}}}{v}r \qquad \alpha_{\mathrm{r}} = -\beta + \frac{l_{\mathrm{r}}}{v}r. \tag{2.3}$$

The angular velocities of the front and rear wheels are added to the single-track model to consider longitudinal slips of the front and rear axles. Specifically, variables ω_{f} and ω_{r} are included in (2.1). Note that the linear lateral motion is not affected by performing this augmentation. These angular velocities are considered to be inputs to the model. Hence the vector of control variables is expanded. Therefore, the following matrix version

Table 2.1: Vehicle Model Notation

Description	Symbol	Units
Vehicle speed at CG	v	$\mathrm{m\,s^{-1}}$
Sideslip angle at CG	β	rad
Yaw rate at CG	r	$\mathrm{rad\,s^{-1}}$
Steering angle of the front axle	δ	rad
Angular velocity of [front, rear] axle	$\omega_{[\mathrm{f,r}]}$	$\mathrm{rad\,s^{-1}}$
Load force of [front, rear] axle	$F_{\mathrm{z}[\mathrm{f,r}]}$	N
Lateral tire force on [front, rear] axle	$F_{\mathrm{y}[\mathrm{f,r}]}$	N
Longitudinal tire force on [front, rear] axle	$F_{\mathrm{x}[\mathrm{f,r}]}$	N
Sideslip angle of [front, rear] axle	$\alpha_{[f,r]}$	rad
Slip ratio of [front, rear] axle	$\lambda_{[f,r]}$	–
Vehicle mass	m	kg
Yaw moment of inertia at CG	I	$\mathrm{kg\,m^2}$
Distance from CG to [front, rear] axle	$l_{[\mathrm{f,r}]}$	m
Lateral tires nominal stiffness of [front, rear] axle	$c_{\alpha[\mathrm{f,r}]}$	$\mathrm{rad^{-1}}$
The velocity vector of the center of [front, rear] axle	$v_{[\mathrm{f,r}]}$	$\mathrm{m\,s^{-1}}$
Half of axle width	w	m
Effective wheel radius	p	m

of the model from (2.1) can be considered, which boils down to

$$\dot{x}(t) = Ax(t) + Bu(t) \tag{2.4}$$

where system matrices are explicitly given by first-order Taylor expansion, as follows

$$A = \begin{bmatrix} -\dfrac{c_{\alpha\mathrm{f}}F_{\mathrm{zf}} + c_{\alpha\mathrm{r}}F_{\mathrm{zr}}}{mv} & \dfrac{l_{\mathrm{r}}c_{\alpha\mathrm{r}}F_{\mathrm{zr}} - l_{\mathrm{f}}c_{\alpha\mathrm{f}}F_{\mathrm{zf}}}{mv^2} - 1 \\ \dfrac{l_{\mathrm{r}}c_{\alpha\mathrm{r}}F_{\mathrm{zr}} - l_{\mathrm{f}}c_{\alpha\mathrm{f}}F_{\mathrm{zf}}}{I} & -\dfrac{l_{\mathrm{r}}^2c_{\alpha\mathrm{r}}F_{\mathrm{zr}} + l_{\mathrm{f}}^2c_{\alpha\mathrm{f}}F_{\mathrm{zf}}}{vI} \end{bmatrix}, \quad B = \begin{bmatrix} \dfrac{c_{\alpha\mathrm{f}}F_{\mathrm{zf}}}{mv} & 0 & 0 \\ \dfrac{l_{\mathrm{f}}c_{\alpha\mathrm{f}}F_{\mathrm{zf}}}{I} & 0 & 0 \end{bmatrix} \tag{2.5}$$

and state and input vectors are provided in the following order

$$x = \begin{bmatrix} \beta \\ r \end{bmatrix}, \quad u = \begin{bmatrix} \delta \\ \omega_{\mathrm{f}} \\ \omega_{\mathrm{r}} \end{bmatrix}. \tag{2.6}$$

The dynamics in (2.4) is continuous and must be discretized for the discrete model predictive controller. Using a discrete regulator makes it possible to work in the same manner as modern stability systems, which are operated discretely. This work assumes a

discrete model

$$x_{k+1} = A_{\mathrm{d}} x_k + B_{\mathrm{d}} u_k \tag{2.7}$$

where matrices

$$A_{\mathrm{d}} = I + T_{\mathrm{s}} A \quad \text{and} \quad B_{\mathrm{d}} = T_{\mathrm{s}} B \tag{2.8}$$

are obtained by the forward Euler discretization of (2.4). In (2.8), I is an identity matrix of size 2, and T_{s} is a discretization step on which the controller operates.

2.2.1 Wheel Dynamics

This work assumes the linear single-track model defined above as a prediction model. However, to complete the picture, slip variables must be defined formally. Those definitions will be used later in this text.

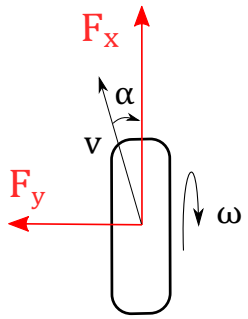

Figure 2.2: Wheel coordinate frame.

Tire forces are connected with tire sideslip angle, defined as,

$$\alpha_i = -\arctan \frac{v_{\mathrm{y}i}}{|v_{\mathrm{x}i}|} \tag{2.9}$$

where a particular i-th wheel ($i \in \{\mathrm{f}, \mathrm{r}\}$) has a velocity vector with lateral v_{y} and longitudinal v_{x} components in the wheel coordinate frame shown in Fig. 2.2. Equations (2.3) are linear approximations of the definition (2.9). Also, there is a definition of slip ratio with physical meaning, what part of the wheel's rotation is connected with its translational velocity. It is defined as,

$$\lambda_i = \frac{\omega_i p - v_{\mathrm{x}i}}{\max(|\omega_i| p, |v_{\mathrm{x}i}|)}. \tag{2.10}$$

The slip ratio value is negative when the wheel is braking and positive when an additional rotational moment is applied on the axle.

2.3 Tire Traction Forces Analysis

Tire traction forces are a natural source of vehicle movement. Generally, each tire on a flat surface produces a force vector $[F_{\mathrm{x}}, F_{\mathrm{y}}]$, generating lateral and longitudinal traction forces in the wheel's coordinate frame (Fig. 2.2.) Tire force generation is one of the most challenging topics in vehicle dynamics. From many trials and errors, automotive engineers connected the produced force vector with wheel slip units [46]. When the tire or wheel performs only longitudinal slip λ, it generates only the longitudinal component F_{x}. The same can be stated for the lateral dynamics. Those two separate cases can be mathematically described in many ways [47]. However, in normal operation conditions, wheels produce combined force in both directions. In this case, physical restrictions start to play their roles.

A tire cannot generate a combined force greater than it "has" – a load force F_{z} the car applies to the particular tire. It creates a natural boundary for the magnitude of the traction force vector, named the traction ellipse. This restriction can be mathematically written as,

$$\sqrt{\left(\frac{F_{\mathrm{x}}}{c_{1\mathrm{x}}}\right)^2 + \left(\frac{F_{\mathrm{y}}}{c_{1\mathrm{y}}}\right)^2} \leq \mu F_{\mathrm{z}} \tag{2.11}$$

where parameters $c_{1\mathrm{x}}$ and $c_{1\mathrm{y}}$ are friction coefficients between the tire and the surface in longitudinal and lateral directions, respectively. Those parameters depend on particular tires and are the reason for the shape of the traction ellipse for a given surface. Parameter μ represents the friction coefficient between the particular tire and the driving surface. The graphical representation of an example of such an ellipse is shown in Fig. 2.3.

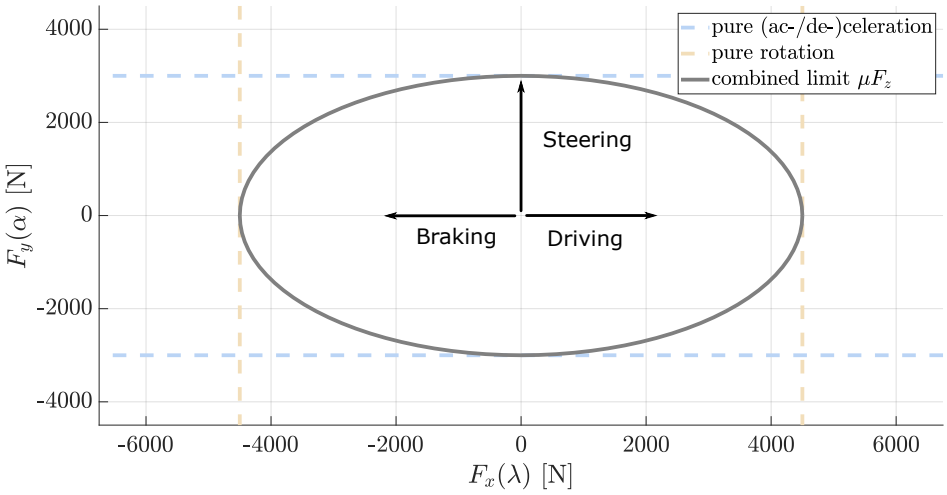

Figure 2.3: Tire traction limits in the form of traction ellipse.

There is a plenty of different tire models [47]. The simplest way to model tire behavior is through statistical models. One of them, used for tire traction force analysis in this

work, is the Pacejka Magic formula [46] (its name speaks for itself). The core function (also known as the Simplified Pacejka Magic formula) connects a slip variable with a force component in one direction and has the following nonlinear form:

$$F(s) = c_1 F_z \sin[c_2 \arctan(c_3 s - c_4(c_3 s - \arctan(c_3 s)))] \tag{2.12}$$

where c_i are shaping coefficients and s is a slip ratio λ, in case of longitudinal traction force F_x, and sideslip angle α for lateral traction force F_y. Function (2.12) with appropriate shaping coefficients for a typical lateral and longitudinal tire force is depicted in Fig. 2.4.

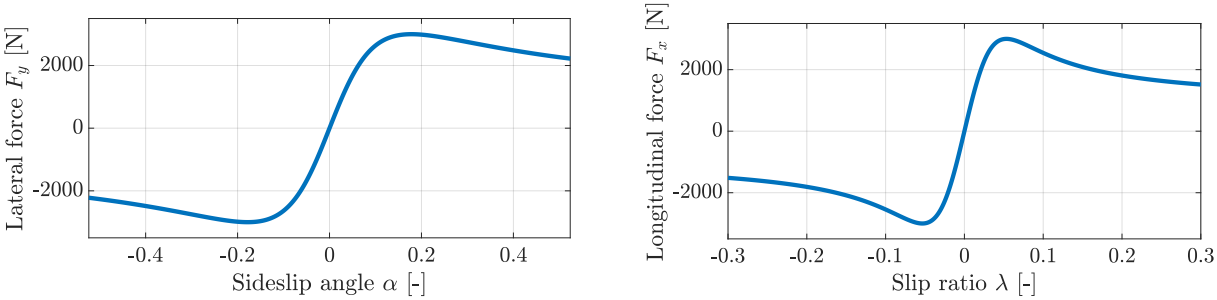

(a) Lateral force. (b) Longitudinal force.

Figure 2.4: Example of lateral and longitudinal forces acting on a tire with dependency on slip variables.

The Simplified Pacejka Magic formula's approximation is valid only for pure wheel acceleration, deceleration, and rotation. However, in reality, each component in the force vector depends on both slip variables simultaneously. While a wheel slips on a side, the longitudinal force generation is reduced, and vice versa. That dependency is represented in the (non-simplified) Pacejka Magic formula, which is omitted in this text for its size and complexity and can be found in [46]. Nevertheless, its graphical representation is depicted in Fig. 2.5. Its shape results from the work of the physics standing behind the traction ellipse concept.

Analyzing those shapes, one can admit the following idea of "safe" or "optimal" driving, which can be stated in the following way: "Do not overslip too much." These "optimal" zones are visualized in yellow in Fig. 2.5. When slip variables are going from the middle zone between two peaks of graphs Fig. 2.4, the tire produces less force. At the same time, when slip variables pass those peaks simultaneously – the tire starts to lose traction, which makes the tire almost "useless" in changing vehicle dynamics. As an illustrative example, the reader can imagine what happens with the lateral dynamics of a wheel when the wheel is blocked due to over-braking. In that case, the tire will not grip and will not produce almost any side traction force when the wheel is steered. The same problem is valid for the whole corner cases when the limits of the traction ellipse are reached. Those limits

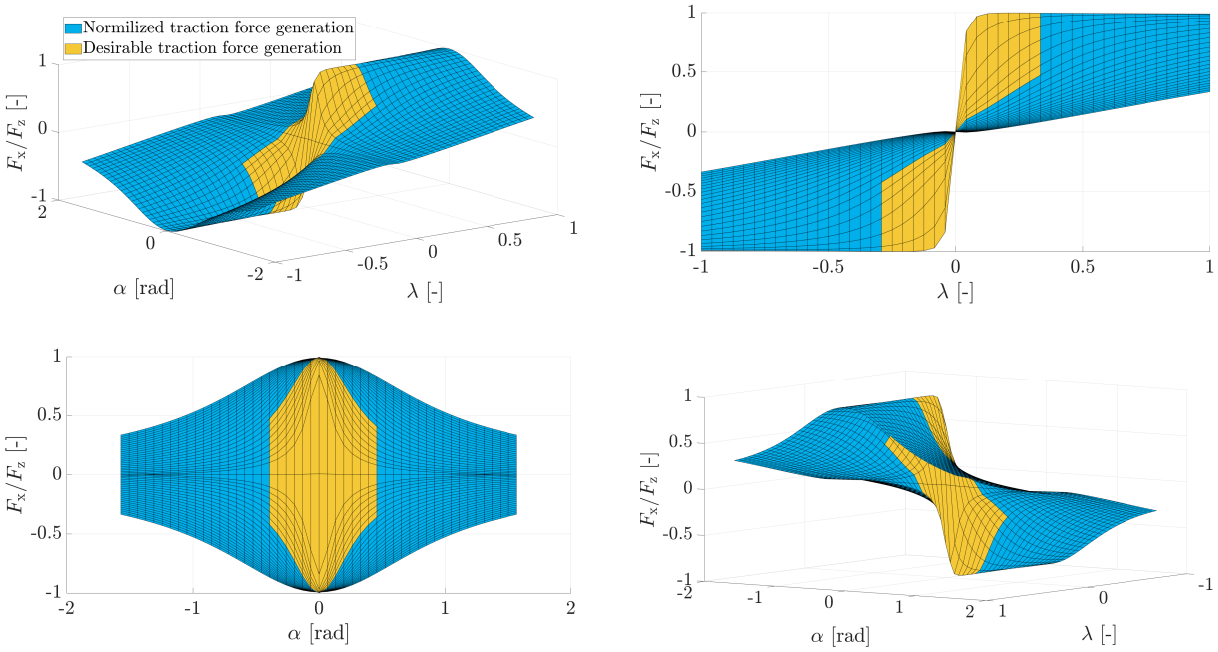

Figure 2.5: Normalized longitudinal tire traction force dependency on both slip variables. Visualization of the Pacejka Magic formula (full version).

make the vehicle dynamics vulnerable for an inexperienced (or even for the experienced) driver. Ideas described here made the basement of the driving envelope concept.

2.4 Definition of the Driving Envelope

The driving envelope combines all wheels' physical limits projected onto the vehicle model variables. It utilizes ideas described during tire traction limits analysis. First, each wheel has the maximum possible lateral and longitudinal force (peak values in Fig. 2.4), which can be generated. After those peaks, there is a plateau or lack of the generated force. Secondly, when combined force is generated – when the wheel generates lateral force and longitudinal force simultaneously – each force vector component restricts the maximal value of the other.

Those physical boundaries are straightforward to express on wheel level dynamics. However, expressing them on the vehicle level is complex but intuitive for an experienced driver. Considering only the wheel level boundaries is insufficient to guarantee vehicle maneuverability and stability. Per each wheel, three kinds of dynamics are considered. Each tire dynamics contributes to vehicle variables constraints (defining the driving envelope). The boundaries come from:

- lateral dynamics → limits of the sideslip angle of a wheel;
- longitudinal dynamics → limits of the slip ratio of a wheel;

- combined dynamics → limits of the combined slip of a wheel.

Preserving the driving envelope limits guarantees the stability of vehicle maneuvers and the controllability of wheels. The stability is defined with a hypothesis (which will be proven experimentally below) that the vehicle maneuver is stable while wheels are not blocked, overspun, or skidding. The controllability is defined similarly but considering the combined dynamics. While the wheel is not blocked or overspun, it can generate lateral force and change the lateral vehicle dynamics. Analogically, while the wheel is not skidding on a side, it can generate longitudinal traction force to increase or decrease the wheel's translation velocity (and the translation velocity of the vehicle.)

For the sake of simplicity, symmetrical tire characteristics will be considered in the rest of this work. However, the approach described here can be adapted for any tire configuration.

2.4.1 Lateral Driving Envelope

The relation between the sideslip angle and the generated lateral force is highly nonlinear. The graphical representation, slip curve, has three major parts (Fig. 2.6). The central part, with the almost linear dependency of F_{y} on α. Secondly, there are two highly nonlinear shoulders where the traction capacity of a tire is depleted, the wheel starts to skid to a side, and the resulting lateral force is limited or reduced. Thus, it brings an idea for the strategy of the driving envelope concept. When the sideslip angle of the wheel is restricted, the wheel will be operated in the desired middle part of its traction characteristics. Therefore, mathematically it can be defined using maximal and minimal possible sideslip angles in the following way:

$$-\alpha_{i,\max} \leq \alpha_i \leq \alpha_{i,\max}, \quad i \in \{\mathrm{f}, \mathrm{r}\}. \tag{2.13}$$

Theoretically, the boundary values must be defined precisely at the peak. However, the previously provided experiments in [36] and [48] show that manipulating envelope boundaries can be determined with a slight overcome of the peak value to allow the driver drifting actions during cornering maneuvers. When the boundaries are defined precisely at the peak force values, the resulting response would be too conservative and less comfortable for an untrained (unprofessional) driver. The second reason to overcome peak a bit is that the predictive model is mainly inaccurate (it would never precisely match the actual vehicle behavior.)

In [36], the envelope limits were referred to as "an envelope defined by tire grip." This envelope allows for a wider range of lateral vehicle dynamics than the handling envelope presented in the same work. However, the author notes a drawback: the actuator and

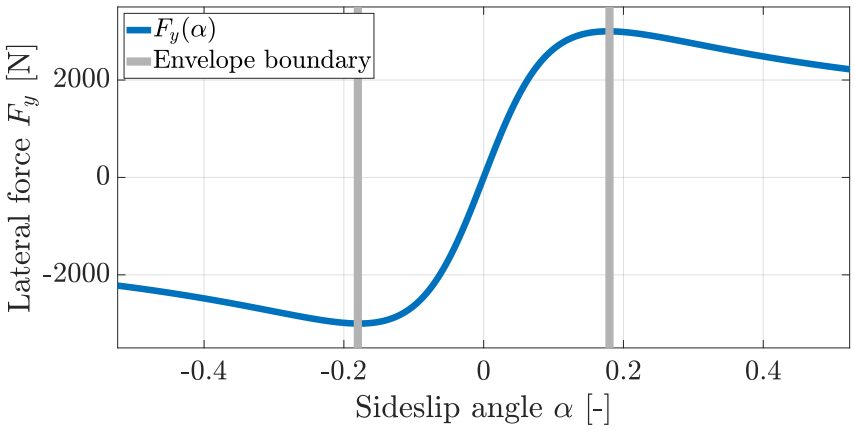

Figure 2.6: Lateral tire force and example of envelope boundary.

state limits are coupled together (due to the dependency of the sideslip angle of the front axle on the steering angle (2.3)). This coupling could limit the amount of countersteer allowed by the controller in situations where the steering angle must be rapidly changed to stabilize the vehicle. Nevertheless, this limitation can be overcome by tuning the resulting controller appropriately, ensuring that it is not overly conservative and has the ability to exceed the defined limits.

2.4.2 Longitudinal Driving Envelope

The principal relationship between the slip ratio and the generated longitudinal force at the tire-road contact point is the same as for the lateral part. The absolute value of the slip ratio reaches zones where the wheel is locking (in case of braking), or the wheel gets more wheelspin concerning the traveling velocity due to a loss of traction with a drivable surface (in case of accelerating). Therefore, the slip ratio can be constrained in the same way by maximum and minimum values to avoid wheelspin and wheel-locking situations:

$$-\lambda_{i,\max} \leq \lambda_i \leq \lambda_{i,\max}, \quad i \in \{\mathrm{f}, \mathrm{r}\}. \tag{2.14}$$

Choosing those limits rhymes with the strategy described for the lateral driving envelope part. When limits are wider, the controller would be less conservative, the lack of the generated force would be more significant, and the time for the wheel to return to the “safe" operation region (the middle part of the traction force graph) would be longer.

In [49], it was demonstrated using trimmed twin-track model root locus analysis that when slip variables exceed the peak values of maximum (or minimum) possible traction force, the trimmed system becomes unstable. However, this instability can be mitigated using feedback control that maintains longitudinal slip at a reference value, even if this value was chosen as unstable (behind the peak value).

2.4.3 Combined Driving Envelope

The combined driving envelope is introduced to define an envelope boundary, which combines both dynamics. This boundary is derived due to traction limits, which were called above as traction ellipse (2.11).

A wheel affects the motion of the car body, and the car body can act on the wheel (Fig. 2.3). The maximum possible force, which can be generated and translated to the vehicle body, is restricted on each wheel. Because of this force, the vehicle is moving. However, it works in the other way too. The car can transfer the force vector to the wheel with a magnitude bigger than the wheel can transfer to the surface. When it happens, the tire loses its grip on the surface, leading to dangerous situations in cases of lack of control. When the driver keeps the car moving so that one or more wheels lose the grip and get it back with frequent changes between those two states, people can find this behavior “fun" and “interesting." A specific term, “drift," is even created for such vehicle motion.

There are two ways to represent the combined driving envelope boundary. One uses the resulting combined forces obtained using the Simplified Pacejka Magic formula (2.12) and restricts its maximum value using inequality (2.11). The other uses one of the combined slip definitions and restricts the magnitude of the resulting vector. The prior can be mathematically stated as,

$$P_{\mathrm{x}}^2(\lambda_i) + P_{\mathrm{y}}^2(\alpha_i) \leq 1, \quad i \in \{\mathrm{f}, \mathrm{r}\} \tag{2.15}$$

where $|P_{\mathrm{x}}^2(\lambda_i)| \leq 1$ and $|P_{\mathrm{y}}^2(\alpha_i)| \leq 1$ are normalized (load and friction independent) curves of tire traction forces in both, longitudinal and lateral directions. The inequality (2.15) creates an ellipsoidal boundary of the total normalized generated force vector.

The former needs a definition of the combined slip. This definition will be used later in this text in the model predictive control formulation because it will reduce the necessity of nonlinear controller implementation. Also, this choice makes the controller independent of the changes in the driving surface (which will be discussed later in the text below).

The combined slip is a vector with two components: longitudinal and lateral slips. Slip ratio and sideslip angle have different units, and they need to be scaled to be combined into one vector. There are several ways to do that, listed in [47]. This work assumes the following definition:

$$\overline{\sigma} = [\sigma_{\mathrm{x}} \quad \sigma_{\mathrm{y}}] = \begin{bmatrix} \dfrac{\lambda}{1-\lambda} & \dfrac{\tan\alpha}{1-\lambda} \end{bmatrix} \tag{2.16}$$

where $\overline{\sigma}$ is a combined slip vector for a particular wheel. Using combined slip definition and the prior envelope's notation, the point at which traction forces in both directions

reach their maximum values can be defined as,

$$\sigma_{\mathrm{x}}^{*} = \frac{\lambda_{\max}}{1-\lambda_{\max}} \qquad \sigma_{\mathrm{y}}^{*} = \frac{\tan\alpha_{\max}}{1-\lambda_{\max}}. \tag{2.17}$$

The restriction of the traction ellipse is then can be reformulated as a boundary for the magnitude of the normalized slip vector as,

$$|\sigma_{\mathrm{N}}| = \left|\begin{bmatrix}\frac{\sigma_{\mathrm{x}}}{\sigma_{\mathrm{x}}^{*}} & \frac{\sigma_{\mathrm{y}}}{\sigma_{\mathrm{y}}^{*}}\end{bmatrix}\right|_{2} = \sqrt{\left(\frac{\sigma_{\mathrm{x}}}{\sigma_{\mathrm{x}}^{*}}\right)^{2} + \left(\frac{\sigma_{\mathrm{y}}}{\sigma_{\mathrm{y}}^{*}}\right)^{2}} = \frac{1-\lambda_{\max}}{\lambda_{\max}\tan\alpha_{\max}} \frac{\sqrt{\lambda^{2}\tan^{2}\alpha_{\max} + \lambda_{\max}^{2}\tan^{2}\alpha}}{|1-\lambda|} \leq 1. \tag{2.18}$$

Providing the transformation done in (2.18), the “traction circle" restriction is obtained, which will be called normalized traction ellipse in this work.

2.4.4 Linearization of Driving Envelope Components

The previously defined constraints of the driving envelope can be used for envelope protection in nonlinear model predictive control. However, linear model predictive control would work faster with less computational consumption, and experiments show that the linear version is sufficient to cover all “safe" vehicle maneuvers. This section derives linear approximations of the envelope constraints (2.13), (2.14), and (2.18). To do so, let the author answer the question: “Is it sufficient to assume general single-track with lumped wheels?" The short answer is: “Not exactly."

Single-track model corrections

The single-track model is sufficient to analyze the lateral and longitudinal dynamics separately. However, operating with a car involves simultaneous intervention into both dynamics under normal operating conditions. The influence of yaw rate on the difference between slip variables of wheels on the same axle (left and right) is represented only in the twin-track model. The sideslip angle and slip ratio are dependent on the wheel's velocity ((2.9), (2.10)). The components of the velocity vector are defined as,

$$\begin{pmatrix} v_{\mathrm{xf}j} \\ v_{\mathrm{yf}j} \end{pmatrix} = \begin{pmatrix} \cos\delta & \sin\delta \\ -\sin\delta & \cos\delta \end{pmatrix} \cdot \begin{pmatrix} v\cos\beta \mp wr \\ v\sin\beta + l_{\mathrm{f}} r \end{pmatrix}, \quad j \in \{\mathrm{l},\mathrm{r}\} \tag{2.19}$$

where the term wr, which has a different sign for a different side of an axle, has a low influence on the lateral velocity of a wheel due to the effect of $-\sin(\delta)$. On the other hand, the influence of this term on the longitudinal velocity of the same axle is high due

to the effect of $\cos(\delta)$.

While looking at the definition of sideslip angle (2.9) stated here again,

$$\alpha = -\arctan\frac{v_{\mathrm{y}}}{|v_{\mathrm{x}}|}, \tag{2.20}$$

one can admit that differences in the sideslip angles of wheels placed on the same axle are small and can be neglected. On the other hand, the dependency of the slip ratio on the longitudinal velocity component is non-neglectable because this component is presented on both parts of the fraction

$$\lambda = \frac{\omega p - v_{\mathrm{x}}}{\max(|\omega|p, |v_{\mathrm{x}}|)}. \tag{2.21}$$

Some maneuvers can lead to a dramatic difference between slip ratios of wheels placed on the same axle due to the vehicle's rotation around its vertical axis. There are even cases when one wheel of the axle can have a slip ratio around zero. At the same time, another wheel can be locked or overspun due to the rotation (this "feature" of vehicle dynamics is widely used nowadays in stability systems such as electronic stability programs).

Therefore, providing the linearization of the sideslip angle, one can use the same linear approximation (2.3) for both wheels of one axle. However, linear approximations of slip ratios have to provide information about their dependency on the yaw rate of a vehicle.

Linear driving envelope components

Following the idea described above, the linear approximation of the lateral driving envelope can straightforwardly use equations used to derive the linear vehicle dynamics:

$$\alpha_{\mathrm{f,lin}} = \delta - \beta - \frac{l_{\mathrm{f}}}{v}r \qquad \alpha_{\mathrm{r,lin}} = -\beta + \frac{l_{\mathrm{r}}}{v}r \tag{2.22}$$

where v is a non-zero constant vehicle speed at the moment of the controller initialization, then inequality (2.13) can be applied to linear approximations of sideslip angles to create a linear constraint of the lateral driving envelope.

Slip ratios have to be linearized concerning saving their dependency on the lateral dynamics of a vehicle and have to be considered for each wheel and not for each axle:

$$\begin{aligned} \lambda_{\mathrm{fl,lin}} &= \frac{p\omega_{\mathrm{f}} - wr}{v} - 1 \qquad & \lambda_{\mathrm{fr,lin}} &= \frac{p\omega_{\mathrm{f}} + wr}{v} - 1 \\ \lambda_{\mathrm{rl,lin}} &= \frac{p\omega_{\mathrm{r}} - wr}{v} - 1 \qquad & \lambda_{\mathrm{rr,lin}} &= \frac{p\omega_{\mathrm{r}} + wr}{v} - 1. \end{aligned} \tag{2.23}$$

Thus, the linear longitudinal driving envelope constraints can be obtained by applying the inequality (2.14) per each linear slip ratio.

The normalized combined slip (2.18) could be linearly approximated as follows,

$$\frac{1-\lambda_{\max}}{\lambda_{\max}\tan\alpha_{\max}}\frac{\sqrt{\lambda^2\tan^2\alpha_{\max}+\lambda_{\max}^2\tan^2\alpha}}{|1-\lambda|}=\frac{1-\lambda_{\max}}{|1-\lambda|}\sqrt{\frac{\lambda^2\tan^2\alpha_{\max}+\lambda_{\max}^2\tan^2\alpha}{\lambda_{\max}^2\tan^2\alpha_{\max}}}$$
$$\approx(1-\lambda_{\max})\sqrt{\frac{\lambda^2}{\lambda_{\max}^2}+\frac{\tan^2\alpha}{\tan^2\alpha_{\max}}}\approx\frac{1-\lambda_{\max}}{\lambda_{\max}}|\lambda|+\frac{1-\lambda_{\max}}{\tan\alpha_{\max}}|\alpha|$$

where the term $|1-\lambda|$ was approximated by 1, a square root of the sum was approximated by the sum of square roots, and the tangent was approximated by its argument. Hence, the linear version of normalized combined slip can be defined as,

$$\sigma_{ij,\mathrm{N,lin}}=\frac{1-\lambda_{\max}}{\lambda_{\max}}|\lambda_{ij,\mathrm{lin}}|+\frac{1-\lambda_{\max}}{\tan\alpha_{\max}}|\alpha_{i,\mathrm{lin}}|,\quad i\in\{\mathrm{f},\mathrm{r}\},\ j\in\{\mathrm{l},\mathrm{r}\}. \tag{2.24}$$

Therefore, to stay inside the traction ellipse, the value of the normalized combined slip has to be limited by 1:

$$\sigma_{ij,\mathrm{N,lin}}\leq 1. \tag{2.25}$$

A constant vehicle speed is assumed for the linearization because the controller for the driving envelope protection will be running at high frequency, similar to, for instance, the anti-lock braking system.

2.4.5 Graphical Meaning of the Driving Envelope

When the envelope constraints are calculated using the standard nonlinear definitions of slip variables, it is impossible to transform envelope boundaries to the vehicle state-space analytically. To investigate how each part of the driving envelope constraints could affect the resulting “safe" subspace in the vehicle state-space, one can iteratively evaluate each state of the state-space and check if those envelope components are fulfilled. This simulation used vehicle parameters listed in Table 2.2. The same analysis could be provided for different car configurations or driving conditions. However, outcomes are expected to have equivalent results.

The dimension of vehicle state space equals six: three states and three inputs, which is impossible to visualize. Therefore, the following figures present the most valuable variables from the state space for the following visual analysis: β, r, and ω_{f}.

Figure 2.7 shows sets of all three nonlinear driving envelope boundaries for each wheel projected onto the vehicle state space separately. Figure 2.8 presents sets of linear driving envelope boundaries projected onto the vehicle state space separately.

The linear combined envelope boundary forms a diamond-like set in the $(\beta,\omega_{\mathrm{f}},r)$-space, shown in red in Fig. 2.8. At this point, it may not be evident that this boundary

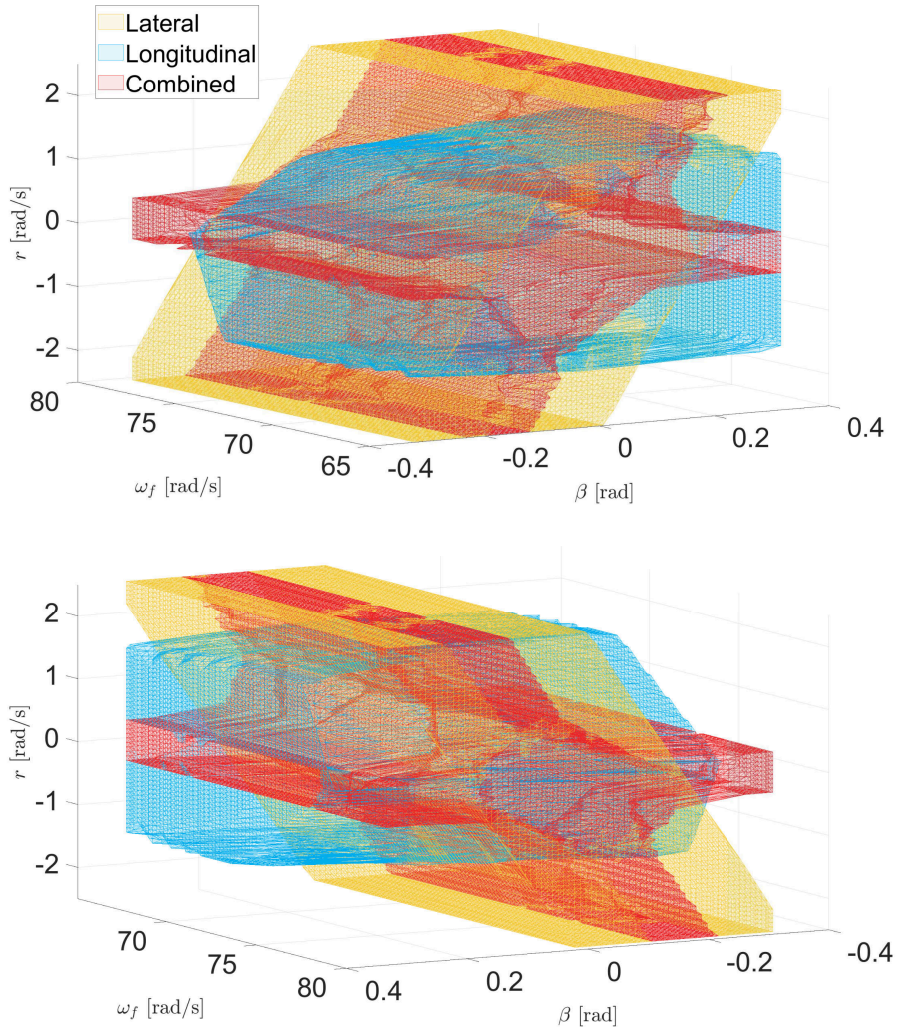

Figure 2.7: Nonlinear driving envelope applied on vehicle dynamics shown for the front axle. The envelope is depicted for constant velocity v.

is enough to cover all “safe" vehicle states for the linear case. However, it is evident from the graphical representation presented in Fig. 2.9, where the intersection of three envelope boundaries is illustrated. The fact that the combined driving envelope equals the intersection of all three envelope parts shows that the number of conditions can be reduced to one (2.25) per wheel.

The intersection of all three nonlinear driving envelope sets from Fig. 2.7 also forms a diamond-like shape, presented by the blue color in Fig. 2.9. The set, obtained by applying three linear driving envelope boundaries, sufficiently matches its nonlinear analog. This fact suggests that only a linear combined driving envelope boundary (2.25) is sufficient to define all “safe" vehicle states for a wheeled vehicle.

The linear lateral driving envelope (yellow in Fig. 2.7) perfectly matches the nonlinear set (yellow in Fig. 2.8). Therefore, the lateral driving envelope protection controller could be linear for all regions, nearly without performance loss. The obtained set looks familiar

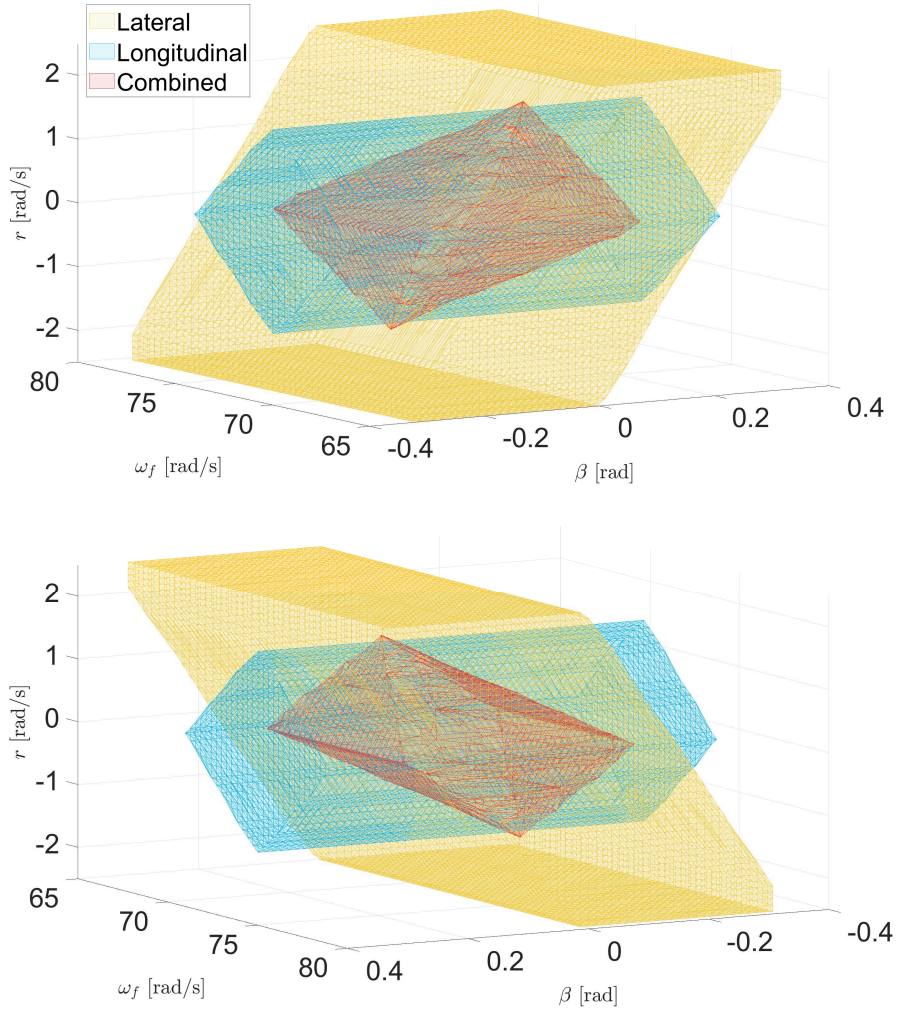

Figure 2.8: Linear driving envelope applied on vehicle dynamics shown for the front axle. The envelope is depicted for constant velocity v.

after the handling envelope presented in [37], which is analyzed in the next section.

2.4.6 Comparing Driving and Handling Envelopes

A comparison between the boundaries created by the driving envelope and handling envelope [37] in vehicle dynamics would be interesting. Figure 2.10 presents such a comparison, revealing four white pyramid-like spaces that are included in the handling envelope but excluded from the driving envelope. This results from applying the longitudinal and combined driving envelope constraints, which can be seen in Fig. 2.7 and 2.8. In these zones, the produced traction force is already saturated, and the tire reaches its traction capacity. Despite being controllable in a controllable drift, this behavior can lead the vehicle into undesired unstable maneuvers. On the other hand, the driving envelope offers a wider range of possible yaw rate generation with a smaller sideslip angle. This occurs when the car is slipping in one direction, but it could generate more yaw rate in the same

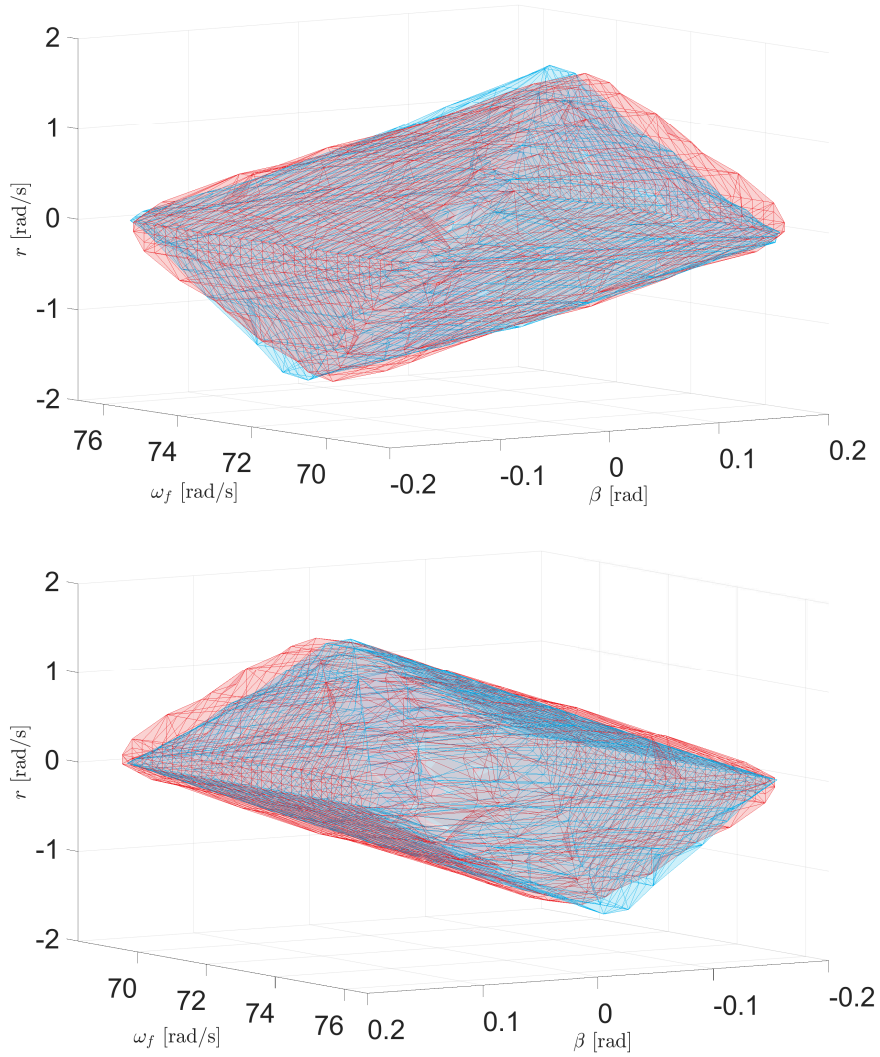

Figure 2.9: Comparison of resulting nonlinear (blue) and linearized (red) driving envelopes applied on vehicle dynamics for the same constant velocity.

direction, reducing the vehicle's sideslip angle amplitude with time (see (2.5)). However, the handling envelope restricts these states since it utilizes a steady-state formulation of boundaries for the yaw rate, resulting in a restriction for lateral acceleration in the center of gravity.

In Figure 2.10, the system trajectories from different states are depicted after applying all available inputs, including steering and angular velocities. These states are selected inside both envelopes, out of one of them and out of both. The simulation aims to determine if it is possible to return from those states within the predefined constraints, or in other words, if those sets are feasible. The figures demonstrate that both sets are feasible – if a state is inside the envelope, a control input exists that returns the system to that particular envelope. Similarly, when the system is in a state that is close to the boundary but outside of the envelope, it can also be returned to the envelopes.

Table 2.2: Used Simulation Parameters

Description	Symbol	Value	Units
Vehicle mass	m	942	kg
Yaw moment of inertia	I	1297	$\mathrm{kg\,m^2}$
Constant vehicle speed at CG	v	20	$\mathrm{m\,s^{-1}}$
Distance from CG to front axle	l_f	1.35	m
Distance from CG to front axle	l_r	1.023	m
Effective wheel radius	p	0.2765	m
Maximum possible steering angle	δ_max	0.35	rad
Half of axle width	w	0.68	m
Load force of the front axle	F_zf	5257	N
Load force of the rear axle	F_zr	3984	N
Shaping coefficients for lateral tire dynamics	c_1y	1.1	-
	c_2y	1.3	-
	c_3y	4	-
	c_4y	-20	-
Shaping coefficients for longitudinal tire dynamics	c_1x	1.4	-
	c_2x	1.3	-
	c_3x	16	-
	c_4x	-10	-

However, when the car is skidding with a high sideslip angle and its yaw rate goes in the opposite direction, the trajectories would not return inside the envelopes. Such behavior is dangerous and undesired for the car.

The feasibility of the driving envelope using the invariant set theory is discussed in the next section.

2.4.7 Feasibility of Linear Driving Envelope

Whereas there is a limited possibility of proving the nonlinear driving envelope's feasibility (2.13), (2.14), and (2.15), it is still possible to provide proof for the linear case, which yields satisfactory results in the closed-loop implementation.

To use algorithm 11.2 for the maximum control invariant set calculation from [50], an autonomous system from the discretized linear single-track needs to be constructed as follows,

$$x_{k+1}^{'} = A^{'} x_k^{'}, \text{ where} \tag{2.26}$$

$$A^{'} = \begin{pmatrix} A_\mathrm{d} & B_\mathrm{d} \\ 0 & 0 \end{pmatrix} \text{ and } x^{'} = \begin{bmatrix} x_k \\ u_k \end{bmatrix}. \tag{2.27}$$

The algorithm calculates intersections of the polytope $\mathcal{P}$ from (2.35) (which include all boundaries applied on the linear system) with future control boundaries (obtained by

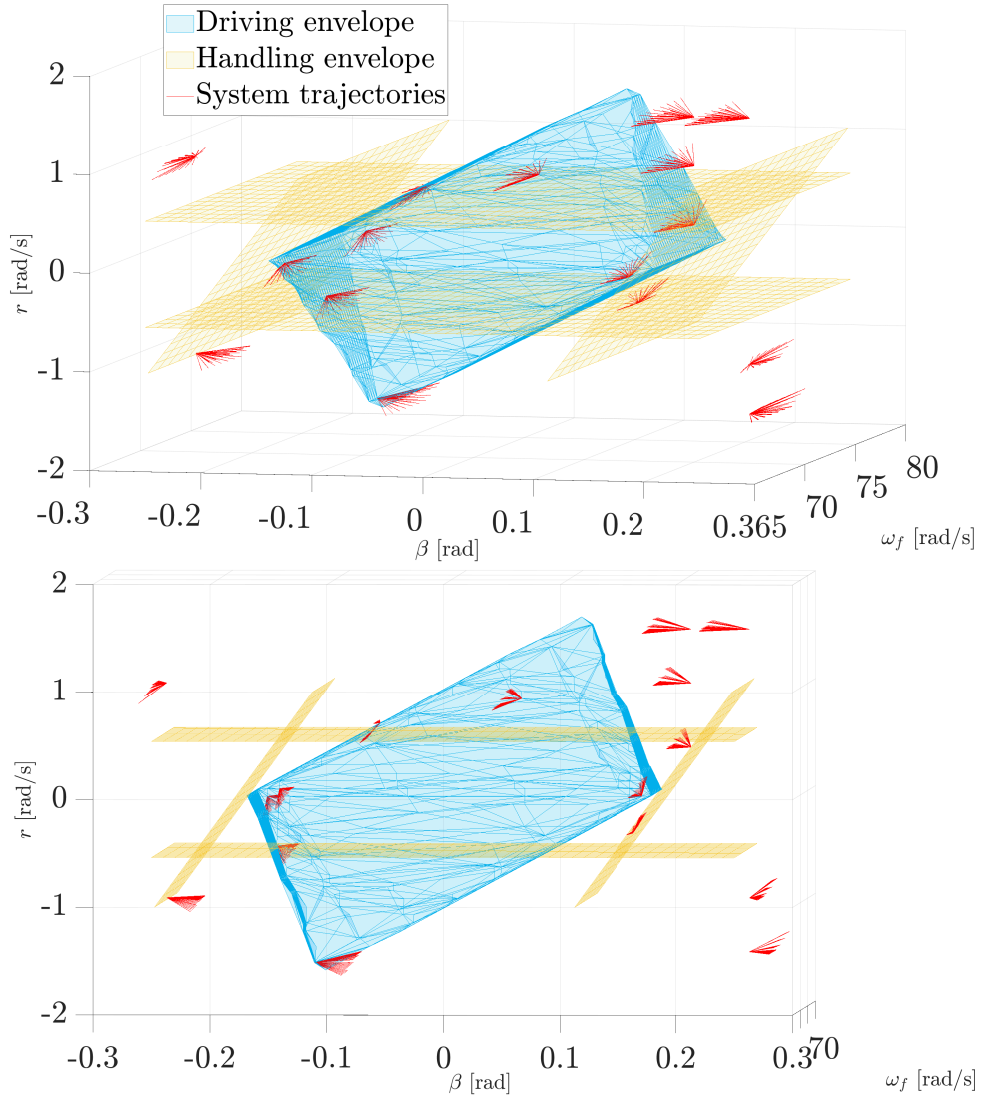

Figure 2.10: Comparison between nonlinear driving and handling envelopes [37] in vehicle dynamics at constant velocity. The red lines represent system trajectories that depend on the chosen control input. For any state within both envelopes, a combination of inputs returns the system to the corresponding envelope. Furthermore, it is possible to return to the safety envelopes from outer states as well, except for two quadrants.

linear mapping of the polytope $\mathcal{P}$ and autonomous discretized linear single-track dynamics $A^{'}$) until the resulting intersection stop changing. The resulting intersection is the maximum control invariant set $\mathcal{C}_{\infty}$. The term is defined in Chapter 3 of [50].

The driving envelope constraints over a 6-dimensional state-space (2.26) are defined, including constraints that combine states and inputs of the original system (2.7).

This derivation considers only the combined driving envelope part (2.25). As it was discussed earlier, only that boundary combined for each wheel in the system is sufficient to cover the whole “safe" sub-space. Nevertheless, the feasibility of other envelope parts ((2.13) and (2.14)) can be checked in the same manner.

Input constraints and constraints based on the linearization assumption are defined

over the augmented system as,

$$G_{\text{in}} x' \leq f_{\text{in}}, \text{ where} \tag{2.28}$$

$$G_{\text{in}} = \begin{pmatrix} 0 & 0 & 0 & 0 & 0 & 1 \\ 0 & 0 & 0 & 0 & 0 & -1 \\ 0 & 0 & 0 & 1 & 0 & 0 \\ 0 & 0 & 0 & -1 & 0 & 0 \\ 0 & 0 & 0 & 0 & 1 & 0 \\ 0 & 0 & 0 & 0 & -1 & 0 \\ 0 & 1 & 0 & 0 & 0 & 0 \\ 0 & -1 & 0 & 0 & 0 & 0 \end{pmatrix}, \; f_{\text{in}} = \begin{pmatrix} \delta_{\max} \\ -\delta_{\min} \\ \xi/p \\ -\xi/p \\ \xi/p \\ -\xi/p \\ \xi \\ \xi \end{pmatrix}, \tag{2.29}$$

and parameter ξ defines some region around vehicle speed v, where the linearization is assumed to be trustful. For instance, this value can be set to $\xi = 1 \text{ m s}^{-1}$.

Furthermore, constraints based on the normalized combined slip boundaries (2.25) are derived from its linear approximation (2.24) as,

$$a \left|\lambda_{ij,\text{lin}}\right| + b \left|\alpha_{ij,\text{lin}}\right| \leq 1, \text{ where} \tag{2.30}$$

$$a = \frac{1 - \lambda_{\max}}{\lambda_{\max}} \text{ and } b = \frac{1 - \lambda_{\max}}{\tan \alpha_{\max}} \tag{2.31}$$

and using linear approximations for the sideslip angle of the particular axle (2.22) and slip ratio of the particular (front left in this case) wheel (2.23),

$$\lambda_{\text{fl,lin}} = \frac{p\omega_{\text{f}} - wr}{v} \qquad \alpha_{\text{fl,lin}} = \delta - \beta - \frac{l_{\text{f}}}{v} r. \tag{2.32}$$

Thus, the set of constraints for the front left wheel can be written for the autonomous system as

$$G_{\text{fl}} x' \leq f_{\text{fl}}, \text{ where} \tag{2.33}$$

$$G_{\text{fl}} = \begin{pmatrix} b & 0 & \frac{aw + bl_{\text{f}}}{v} & \frac{-ap}{v} & 0 & -b \\ -b & 0 & \frac{-aw - bl_{\text{f}}}{v} & \frac{ap}{v} & 0 & b \\ -b & 0 & \frac{aw - bl_{\text{f}}}{v} & \frac{-ap}{v} & 0 & b \\ b & 0 & \frac{-aw + bl_{\text{f}}}{v} & \frac{ap}{v} & 0 & -b \end{pmatrix}, \; f_{\text{fl}} = \begin{pmatrix} 1 \\ 1 \\ 1 \\ 1 \end{pmatrix}. \tag{2.34}$$

Analogously, constraints for the other three wheels can be derived similarly.

Combining all constraints together, the polytope would be defined as

$$\mathcal{P} = \left\{ x' \in \mathbb{R}^6 : \begin{pmatrix} G_{\text{in}} \\ G_{\text{fl}} \\ G_{\text{fr}} \\ G_{\text{rl}} \\ G_{\text{rr}} \end{pmatrix} x' \leq \begin{pmatrix} f_{\text{in}} \\ f_{\text{fl}} \\ f_{\text{fr}} \\ f_{\text{rl}} \\ f_{\text{rr}} \end{pmatrix} \right\}. \tag{2.35}$$

The polytope creation and subsequent numerical operations were performed via the

MPT3 toolbox [51] in MATLAB.

A set in the augmented autonomous vehicle state-space (2.26) is represented by the polytope $\mathcal{P}$. Within this set, each point simultaneously satisfies combined driving envelope restrictions for each wheel and physical limits for control inputs. The calculation of a maximum control invariant set $\mathcal{C}_\infty$ is enabled by the definition of the set $\mathcal{P}$, which is a necessary step in the design of any advanced control theory strategy for vehicle operation. The control strategy will ensure each wheel's stability boundaries once the control invariant set is a subset of the polytope $\mathcal{P}$. It is acknowledged that this approach yields conservative restrictions on vehicle operation due to the linearization step. However, it ensures that the physical limitations of vehicle operations are aligned with the stability and feasibility guarantees given by any advanced control strategy.

The maximum control invariant set $\mathcal{C}_\infty \subseteq \mathcal{P}$ can be iteratively calculated for the resulting polytope combined with linearized vehicle dynamics for each constant velocity using the algorithm 11.2 in [50]. Unfortunately, a calculation can be provided only numerically for any reasonable v and T_s. Figure 2.11 shows the determinedness index of the maximum control invariant set, dependent on the constant velocity and sampling period used for the model linearization and discretization. This value tells how many steps the model predictive control needs to reach the control invariant set. If the system remains in the maximum control invariant set, the controller will always be able to find at least some control input, which will keep the system inside the maximum control invariant set.

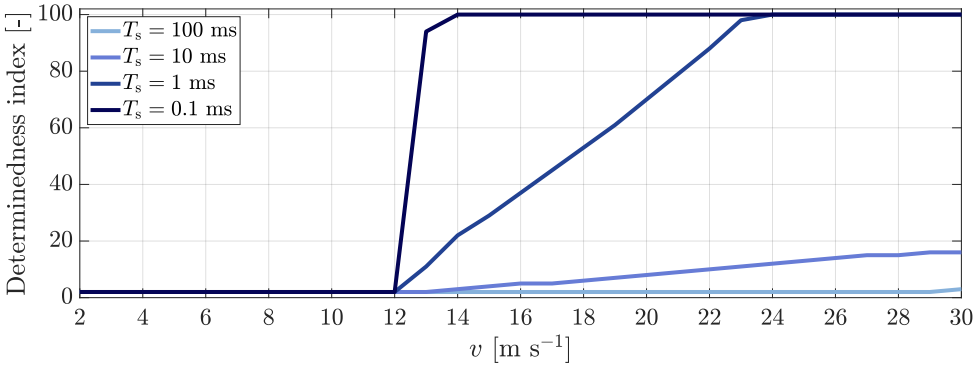

Figure 2.11: Determinedness index of the maximum control invariant set with dependency on the constant velocity and sampling period used for the model linearization and discretization. Maximum iterations are bounded by 100.

The maximum control invariant set is nonzero for each polytope defined for a particular velocity. Its determinedness index is equal to some bounded value (for instance, for low velocity, it equals 2). That has the following two outcomes:

- Each polytope $\mathcal{P}$ defines the feasible set suitable for any model predictive control algorithms using Theorem 12.2 from [50].

- That model predictive control has to have the prediction horizon equal to at least two steps (with dependency on a chosen sampling time T_s and vehicle constant speed v).

It is to be recalled that physical restrictions applied to the rate of change of the control inputs were omitted due to the significantly fast dynamics of the steering, powertrain, and braking systems. However, these restrictions can be incorporated into the definition of the polytope (2.35).

Figure 2.12 compares the polytope $\mathcal{P}$ defined for a constant velocity v from Table 2.2, the maximum control invariant set $\mathcal{C}_\infty$, and the iteratively calculated linearized driving envelope for the same velocity setting.

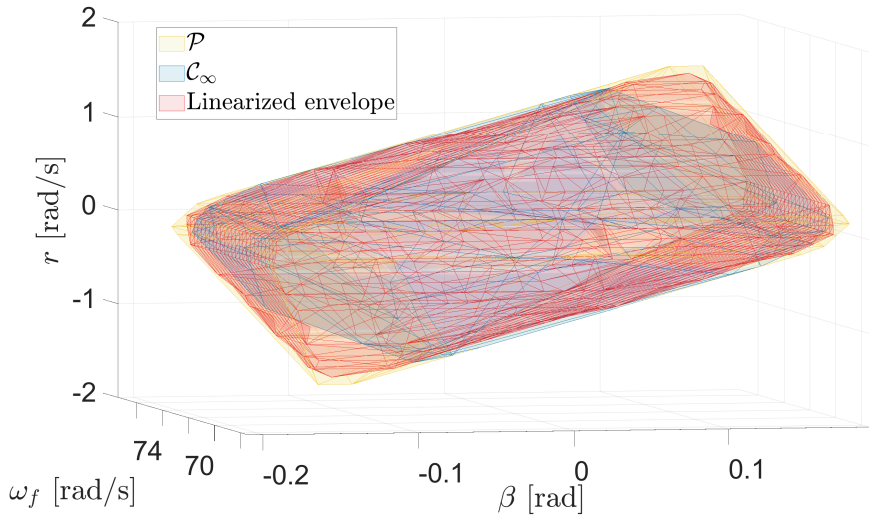

Figure 2.12: Comparison between projections of polytope $\mathcal{P}$ and the maximum control invariant set $\mathcal{C}_\infty$ on $(\beta, r, \omega_\mathrm{f})$-space with the linearized driving envelope applied on non-linear single-track model for the same velocity setting.

The maximum control invariant set $\mathcal{C}_\infty$ for the linearized single-track model primarily matches the set obtained by constraining the nonlinear vehicle state-space by a linearized combined driving envelope 2.25. Although graphs for a specific vehicle cannot guarantee that the controller for driving envelope protection will always be feasible, they suggest the possibility of successful application. The graphs indicate that the controller developed to protect the linear combined driving envelope boundary will primarily keep the vehicle within the envelope and have a feasible solution. However, it is recommended to use soft constraints for the driving envelope constraints to ensure the persistent feasibility of the controller.

Comparing sets $\mathcal{P}$ and $\mathcal{C}_\infty$, it can be observed that projecting the driving envelope boundaries through the vehicle dynamics to infinite time requires cutting corners, wherein the vehicle skids and increases rotational speed in the same direction. This state is

dangerous from a linear model perspective. However, nonlinear vehicle and tire dynamics might permit such actions, which are shown in the experiments below.

2.5 On Selection of Envelope Boundaries

The driving envelope definition heavily relies on maximum slip values. According to the Magic Formula for combined slip [Chapter 4 in [46]], the value varies depending on operation conditions, mainly with a change of complimentary slip variable (e.g., in the case of the longitudinal force, the sideslip angle dramatically changes the shape of the curve). Other factors are the driving surface, tire types, temperature, and many other aspects.

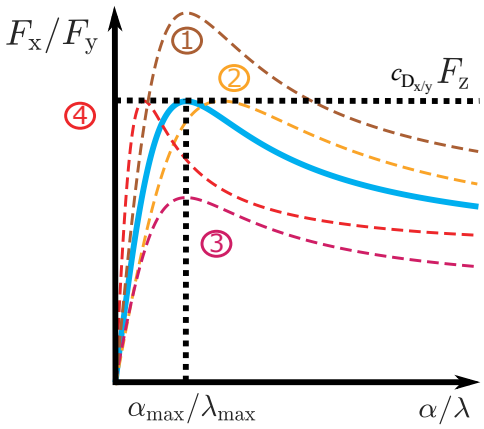

Figure 2.13: Relationship of the traction force on slip variable (blue color) and possible curve changes during driving.

The envelope definition itself is robust with respect to a variation of the road/tire contact interface friction coefficient or the wheel's load force (for illustration, consider cases 1 and 3 in Fig. 2.13). When tire parameters change in the way the peak value passes the predefined boundary (case 2), the control law, based on the initial definition, would not fully utilize the maximum tire capacity. However, the vehicle stability would not be compromised. Conversely, when parameters change so the peak value shifts to the "left" (case 4), the envelope protection algorithm will allow for controlled wheel traction loss. However, experiments with real drivers [37] and simulated drivers (section 2.7) show that skilled drivers prefer a slight "overestimation of maximum slip value"-strategy. In these cases, the resulting controller is less aggressive and conservative and allows pushing the car into controlled drifting maneuvers.

In the control strategies described below, the envelope boundaries α_{max} and λ_{max} are typically fixed pre-selected nominal values. However, they can also be used as tuning parameters to achieve better adjustability for the specific vehicle, driver, and driving

scenario. The selection of these boundaries is subjective and not a straightforward process. Nonetheless, this flexibility allows control engineers to adjust the parameters to suit the specific use case, including factors such as the car, tires, surface, and driving maneuvers. For example, a *sport* regime could increase the allowed slip limits $\lambda_{\max}$ and $\alpha_{\max}$, enabling the driver to operate closer to the limits of tire capacities and perform drifting maneuvers. In contrast, a *highway* setting could be defined with less allowed sideslip values $\alpha_{\max}$ to optimize for driver comfort and increase safety at higher velocities. A *city* mode could have wider sideslip boundaries $\alpha_{\max}$ to allow for short turning at low speeds. Modern car manufacturers already attempt to offer different driving settings, but they typically only involve suspension changes or different gains from pedals to the drivetrain, brakes, and steering wheel. The proposed strategy would be more natural concerning the actual driving physics behind it.

2.6 Control Strategy for Driving Envelope Protection Based on Model Predictive Control

There are many ways to implement a control structure to protect the driving envelope constraints. Presented here is the baseline control strategy (below, mostly called DEP from driving envelope protection) that aims at a conventional car, mainly presented worldwide on roads, equipped with a combustion engine, front-wheel driven, and steered only by the front axle. Therefore, angular velocity for the rear axle ω_r will be omitted in this derivation. Nevertheless, the presented DEP could be easily augmented for over-actuated vehicle platforms, which, for example, use independent motors and/or brakes and possible steering.

The proposed implementation has been verified using the high-fidelity vehicle dynamics simulator IPG CarMaker.

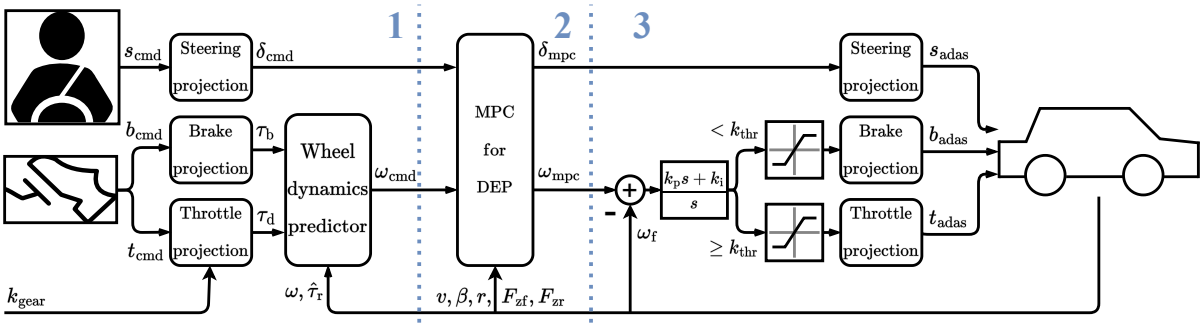

Figure 2.14: Schematic representation of the control strategy.

Three important parts of the operation are accounted for in the overall control strategy's organization.

1 the **projection of the driver's inputs** from the steering wheel and braking and throttle pedals to the commanded steering angle and angular velocities of the front wheels;

2 **MPC for DEP**, which tracks the commanded inputs while subject to constraints defined by the driving envelope;

3 the **projection of the MPC output** in the form of the steering angle and angular velocities of the front wheels to the steering wheel angle and braking and throttle pedals application.

The control strategy is visualized in Fig. 2.14. The individual definitions and mathematical concepts are presented later in this section. Steps 1 and 3 are introduced to significantly reduce the computational difficulty of the MPC in Step 2.

To avoid any numerical issues due to division by zero, it is suggested to switch the controller on when the vehicle speed exceeds some predefined limit (for instance, 1 - 4 [$\mathrm{m\,s^{-1}}$]) or to use other prediction model and slip definition for low velocities.

2.6.1 Driver's Inputs Projection

This part contains steering s_{cmd}, brake b_{cmd}, and throttle t_{cmd} projection on commanded control variables δ_{cmd} and ω_{cmd} used in (2.4). All of the units are completely adjustable to fit any car configuration.

For this work, a linear steering projection defined as,

$$\delta_{\mathrm{cmd}} = k_{\mathrm{steer}} s_{\mathrm{cmd}} \tag{2.36}$$

is used.

The brake projection part from Fig. 2.14 serves to map the brake pedal application to braking torque applied on the front wheels given by

$$\tau_{\mathrm{b}} = k_{\mathrm{brake}} b_{\mathrm{cmd}}. \tag{2.37}$$

The throttle projection part maps the throttle pedal depression and selected gear through the known engine characteristics function to the drive torque applied on the front wheels. The setting "Gas Interpreter" was used for the powertrain control in the CarMaker environment, which allows assuming linear characteristics between the throttle pedal and generated engine torque. The whole function of the block can be modeled as

$$\tau_{\mathrm{d}} = k_{\mathrm{gear}}(k_{\mathrm{eng},1} t_{\mathrm{cmd}} - k_{\mathrm{eng},2}), \tag{2.38}$$

Table 2.3: Control Variables Description

Description	Symbol	Units
Commanded rotation of the steering angle	s_{cmd}	rad
Commanded suppression of brake pedal	b_{cmd}	%
Commanded suppression of throttle pedal	t_{cmd}	%
Commanded steering angle	δ_{cmd}	rad
Commanded brake torque	τ_{b}	%
Commanded drive torque	τ_{d}	%
Estimated or measured wheel reaction torque	$\hat{\tau}_{\text{r}}$	N m
Predicted commanded angular velocity of the front axle	ω_{cmd}	rad s^{-1}
Optimized steering angle	δ_{mpc}	rad
Optimized angular velocity of the front axle	ω_{mpc}	rad s^{-1}
Decision threshold for braking by the engine	k_{thr}	N m
Optimized rotation of the steering angle	s_{adas}	rad
Optimized suppression of brake pedal	b_{adas}	%
Optimized suppression of throttle pedal	t_{adas}	%
Steering column gain	k_{steer}	-
Braking system gain	k_{brake}	N m
Engine control unit's linear gain	$k_{\text{eng,1}}$	N m
Engine control unit's affine parameter	$k_{\text{eng,2}}$	N m
Drivetrain gear coefficient	k_{gear}	-
Drivetrain moment of inertia	I_{w}	kg m^2
Prediction horizon	N	-
Sampling time	T_{s}	s
Reference tracking linear weight	R_1	-
Reference tracking quadratic weight	R_2	-
Fast input change penalty	R_{du}	-
Slew slack penalization	Q_{i}	-
Envelope slack penalization	Q_{e}	-
Rear axle sideslip angle boundary	$\alpha_{\text{r,max}}$	rad
Front axle sideslip angle boundary	$\alpha_{\text{f,max}}$	rad
Front wheels slip ratio boundary	$\lambda_{\text{f,max}}$	-
Slew rate limit for steering angle	$\Delta u^{(1)}_{\text{max}}$	rad s^{-1}
Slew rate limit for angular velocity	$\Delta u^{(2)}_{\text{max}}$	rad s^{-2}
Maximum steering angle	$u^{(1)}_{\text{max}}$	rad
Proportional parameter of PI regulator	k_{p}	-
Integral parameter of PI regulator	k_{i}	-

where k_{gear} represents the transmission with dependency on the selected gear.

This work assumes linear dependency of steering projection, driving, and braking torque generation with dependency on control interface interaction. However, equations (2.36)-(2.38) can be changed and become nonlinear for other characteristics.

The wheel dynamics predictor calculates the angular velocities of the front wheels,

commanded by the driver, as

$$\omega_{\mathrm{cmd}} = \omega + T_{\mathrm{s}} \cdot (\tau_{\mathrm{d}} - \tau_{\mathrm{b}} + \hat{\tau}_{\mathrm{r}})/I_{\mathrm{w}}. \tag{2.39}$$

where front wheel tire reaction torque $\hat{\tau}_{\mathrm{r}}$ is assumed to be measured (or estimated) [52]. For example, this work utilizes the following estimation based on a two-line tire model [11] with simplistic rescaling of the moment based on the wheel's sideslip angle to create similar behavior to Fig. 2.5:

$$\hat{\tau}_{\mathrm{r}} = \begin{cases} -0.1 \cdot p\hat{F}_{\mathrm{fx}}, & 1 - 5\,|\alpha_{\mathrm{f}}| < 0.1 \\ -p\hat{F}_{\mathrm{fx}} \cdot (1 - 5\,|\alpha_{\mathrm{f}}|)\,, & \text{otherwise} \end{cases} \tag{2.40}$$

where the estimation of the traction force is provided as,

$$\hat{F}_{\mathrm{fx}} = \begin{cases} -1.48 \cdot F_{\mathrm{zf}}, & \lambda_{\mathrm{f}} > 0.096 \\ 1.48 \cdot F_{\mathrm{zf}}, & \lambda_{\mathrm{f}} < -0.096 \\ 15.4 \cdot \lambda_{\mathrm{f}}, & \text{otherwise.} \end{cases} \tag{2.41}$$

The implementation of braking, driving, and reaction torque is designed to limit alterations in the driver's perceptual experience. Various methods can be employed to achieve this objective; for example, the act of depressing the brake pedal might cause a reduction in angular velocity, while pressing the throttle pedal could result in an increase.

2.6.2 Synthesis of the Model Predictive Control

The crucial part of the presented DEP is an optimization of control variables utilization with respect to the vehicle physics and driving envelope constraints. To solve this task, model predictive control is defined. The MPC is formulated as a linear convex constrained finite time optimal control problem (OCP). The OCP is solved repeatedly in the receding

horizon fashion [53]. Specifically, the following formulation is considered

$$\min_{u_0,\dots,u_{N-1}} \sum_{k=0}^{N-1} \Big(R_1 \left|\rho - u_k\right| + (\rho - u_k)^\intercal R_2 (\rho - u_k) + (u_k - u_{k-1})^\intercal R_{du} (u_k - u_{k-1}) \Big) \quad (2.42a)$$

$$+ \sum_{k=0}^{N} [s_{\mathrm{i},k}^\intercal Q_\mathrm{i} s_{\mathrm{i},k} + s_{\mathrm{e},k}^\intercal Q_\mathrm{e} s_{\mathrm{e},k}]$$

$$\text{s.t.} \quad x_{k+1} = A_\mathrm{d} x_k + B_\mathrm{d} u_k, \quad (2.42b)$$

$$|u_k - u_{k-1}| \leq \Delta u_\mathrm{max} + s_{\mathrm{i},k}, \quad (2.42c)$$

$$|u_k| \leq u_{\mathrm{max},k}, \quad (2.42d)$$

$$s_{\mathrm{i},k} \geq 0, \quad (2.42e)$$

$$|\sigma_{\mathrm{fl},k}| \leq 1 + s_{\mathrm{e},k}^{(1)}, \quad (2.42f)$$

$$|\sigma_{\mathrm{fr},k}| \leq 1 + s_{\mathrm{e},k}^{(2)}, \quad (2.42g)$$

$$|\alpha_{\mathrm{r},k}| \leq \alpha_\mathrm{r,max} + s_{\mathrm{e},k}^{(3)}, \quad (2.42h)$$

$$s_{\mathrm{e},k} \geq 0, \quad (2.42i)$$

$$x_0 = x(t),\ u_{-1} = u(t - T_\mathrm{s}) \quad (2.42j)$$

with a linear-quadratic objective function (2.42a), defined over the prediction horizon N, where k is a prediction step. Variable t stands for the time of initialization. Variable ρ represents a reference vector $\begin{bmatrix}\delta_\mathrm{cmd} & \omega_\mathrm{cmd}\end{bmatrix}^\intercal$.

The primary goal of the controller (2.42) is to closely track commanded inputs. To achieve this, the objective function (2.42a) comprises quadratic and absolute value terms simultaneously. The quadratic term penalizes significant deviations from the commanded signals ρ, while the linear term penalizes even the slightest deviations from the reference and aids in precise tracking when envelope boundaries are not violated. Using both terms concurrently may increase the computational burden of the solver, leading to longer computation times and higher costs. Additional tests were conducted to investigate this potential issue. Surprisingly, results indicated that using both terms decreased the mean computation time by 5-51 % (depending on the specific test scenario from the experiments section and the term used in the objective function). The quadratic term allows for fast convergence of the optimization problem from a high error, while the linear term enables fast convergence from small errors. To ensure the convexity of the OCP, strictly positive definite factors R_1 and R_2 are enforced. Additionally, inequality constraints are augmented with slack variables $s_\mathrm{i} \in \mathbb{N}_+^2$ and $s_\mathrm{e} \in \mathbb{N}_+^3$ to avoid infeasibility, entering the objective function with high penalties Q_i and Q_e as it is suggested in [54]. The term R_{du} penalizes fast changes of the control variables to make the driving process smoother.

The model predictive control formulation is subject to certain conditions that must be

met. Constraints (2.42b)-(2.42e) are applied for $k = 0, \ldots, N-1$, while constraints (2.42f)-(2.42i) are applied for $k = 0, \ldots, N$. Constraint (2.42b) reflects the discretized linear single-track dynamics from (2.7), whereas inequalities (2.42c) and (2.42d) establish physical limits on control variables, such as slew protection and maximum values. Constraints (2.42f) and (2.42g) delineate the traction rhombus boundaries for the front left and right wheels, respectively, based on linear normalized combined slip definition (2.24) and linear approximations for slip variables (2.22) and (2.23). Constraint (2.42h) sets the boundary for the sideslip angle of the rear wheels, with the sideslip angle defined as (2.22). Only the lateral envelope part is constrained for the rear axle because the objective car is front-wheel driven, and brakes are mostly applied on the front axle. Constraints (2.42f)-(2.42i) are applied to the final state to ensure persistent feasibility. The input vector u_N is set to the previous input u_{N-1}, while the slack variables in (2.42i) and (2.42e) are always non-negative. The OCP problem is initialized with the initial condition in (2.42j), where $x(t)$ represents the state measurement, and $u(t - T_\mathrm{s})$ denotes the control action in the previous sampling instant.

All parameters used for the control strategy are listed in Table 2.3. The maximal angular velocity for the front wheels $u^{(2)}_{\max}$ is time-variant and depends on actual wheel angular velocity and its slew rate setting as:

$$u^{(2)}_{\max,k} = \omega + (k+1) \cdot \Delta u^{(2)}_{\max}. \tag{2.43}$$

Each discrete model predictive control has two key designed parameters: the sampling time T_s and the prediction horizon N. Tuning them is always a tradeoff between having a short prediction window (to prevent long computations) and sufficiently long to cover the dynamics of the system. Compared with the vehicle's rigid body (100-2000 ms), a wheel has significantly fast dynamics (1-10 ms). The sampling time T_s must be short to work with extremely short wheel dynamics. On the other hand, the prediction horizon N must be long enough according to the short sampling period to operate with slow vehicle dynamics. This controller focuses on a short prediction horizon N to reduce computation time and a short sampling period T_s to make a controller fast enough to operate with fast braking and accelerating dynamics. Moreover, applying the theory of invariant sets, it could be numerically shown for the chosen linear vehicle model that for small velocities (under 12 $\mathrm{m\,s^{-1}}$), the maximum control invariant set could be reached in two steps (see section 2.4.7). However, with increasing velocity, the number of steps needed to reach the maximum control invariant set increases. The used sampling period also makes a vast difference in the determinedness index (see Fig. 2.11). Thus, the prediction horizon could be variable and dependent on the current velocity of the controlled vehicle. It could

increase the comfort of the resulting response for the price of the needed computational capacity. The controller, which was used in simulations, had the prediction horizon constantly equal to three steps. Provided experiments show that chosen number of prediction steps is sufficient to ensure the functionality of the driving envelope protection for tested maneuvers.

Remark 1. Soft constraints are utilized to ensure the feasibility property of the controller (2.42), as the driving envelope encompasses the maximum control invariant set for linear vehicle dynamics within its interior 2.12. This approach permits drivers to exceed stability boundaries, particularly with regard to lateral vehicle dynamics. To eliminate soft constraints from the control law, the maximum control invariant set $\mathcal{C}_\infty$ can be computed using algorithm 11.2 from [50], along with inequalities (2.42c), (2.42d), and (2.42f)-(2.42h), and the resulting polyhedron $\mathcal{C}_\infty$ can be employed instead of inequalities (2.42c)-(2.42i). However, based on provided driving simulator experiments, the closed-loop response would be significantly more conservative than the presented solution.

Remark 2. In the event of a change in vehicle configuration, such as switching to a rear-wheel-driven car, the envelope constraints must be modified accordingly. Inequalities (2.42f) and (2.42g) can remain unchanged, as braking torque is primarily applied to the front wheels. However, the lateral envelope constraint (2.42h) must be replaced with the linearized normalized combined slip envelope constraints (2.24) for both rear wheels. Additionally, the wheel dynamics predictor needs to be adjusted to enable predictions for the angular velocities of both axles.

2.6.3 Projection of the Controller's Output

To translate the calculated physical control inputs derived from the optimal control problem into the steering wheel angle, brake, and throttle pedal application, the MPC output is projected. Specifically, the output is projected using inverse functions of the steering projection, which is a straightforward process. The inverse function is obtained by inverting function (2.36) and expressed as,

$$s_{\text{adas}} = \frac{\delta_{\text{mpc}}}{k_{\text{steer}}}. \tag{2.44}$$

The PI controller is utilized to track the angular velocity of the front wheels while preventing output saturation and applying a clamping anti-windup method. The target torque τ_{trg} required by the powertrain or braking system is generated by the PI controller. To approximate the maximum possible braking:

$$\tau_{\text{trg,min}} = -100 \cdot k_{\text{brake}} \tag{2.45}$$

and driving:

$$\tau_{\text{trg,max}} = k_{\text{gear}}(100 \cdot k_{\text{eng},1} - k_{\text{eng},2}) \tag{2.46}$$

torques that can be produced, the torque output of the controller is limited.

To track the target torque by two pedals, a threshold parameter is defined as:

$$\tau_{\text{thr}} = -k_{\text{eng},2} \cdot k_{\text{gear}}. \tag{2.47}$$

The boundary for generating the target torque is defined by the value of τ_{thr}, which determines whether the brake or throttle must be utilized. The value of τ_{thr} is dependent on the current gear ratio and is set slightly negative to enable braking by the engine when a small braking moment is required. Thus, braking pedal application can be defined as

$$b_{\text{adas}} = \begin{cases} 0, & \tau_{\text{trg}} > \tau_{\text{thr}} \\ -\frac{\tau_{\text{trg}}}{100 \cdot k_{\text{brake}}}, & \tau_{\text{trg}} \leq \tau_{\text{thr}}. \end{cases} \tag{2.48}$$

In the same way, the throttle pedal application can be defined as

$$t_{\text{adas}} = \begin{cases} 0, & \tau_{\text{trg}} \leq \tau_{\text{thr}} \\ \frac{1}{100 \cdot k_{\text{eng},1}}\left(\frac{\tau_{\text{trg}}}{k_{\text{gear}}} + k_{\text{eng},2}\right), & \tau_{\text{trg}} > \tau_{\text{thr}}. \end{cases} \tag{2.49}$$

To ensure wheel and vehicle stability in each control operation iteration, the driver's commands $s_{\text{cmd}}, b_{\text{cmd}}, t_{\text{cmd}}$ are replaced by control signals $s_{\text{adas}}, b_{\text{adas}}, t_{\text{adas}}$ from the advanced driver assistance system. Validation of the proposed control strategy using IPG CarMaker is presented in the following section, along with results from experiments conducted.

2.7 Experimental Validation

For validation of the proposed control structure, IPG CarMaker software [55] was used to simulate vehicle dynamics in different driving scenarios. The controller structure from the previous section was implemented in Simulink. The qpOASES [56] solver was used to solve the OCP (2.42) problem and obtain optimal control inputs. Values for parameters used during simulations are presented in Table 2.4.

Due to the highly nonlinear nature of vehicle and tire dynamics, theoretical proof of the stability of the whole closed-loop system is hard or even impossible to provide. However, stability analysis of vehicle trajectories near the edge of tire capacities is possible. Therefore, experimental means of verification of the control concept were selected with four driving scenarios reflecting corner cases of the envelope boundaries. Vehicle maneu-

vers that can excite different vehicle dynamics: lateral, accelerating, and combined lateral and decelerating, were chosen. Those tests were designed to bring the vehicle dynamics close to the driving envelope boundaries (tire traction limits, represented as normalized traction ellipses for subjected (front) wheels in Fig. 2.15) and to provide data to analyze the functionality of the proposed control strategy. The proposed controller was designed to prevent dangerous situations (from the vehicle dynamics point of view) and simultaneously provide functionality similar to ABS, TCS, and ESC systems. Four test scenarios were provided with a comparison to an uncontrolled car.

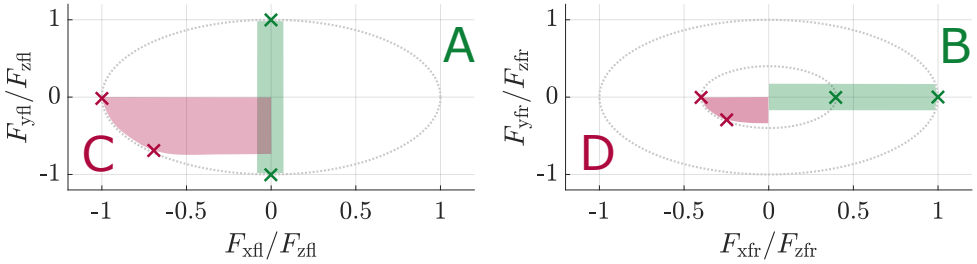

Figure 2.15: Normalized traction ellipses during experiments: Case A - sine with dwell test; Case B - acceleration on slippery surface; Cases C and D - full stops during cornering maneuvers, with and without a friction slip pad.

The goal was to demonstrate the performance of a controlled vehicle compared to an uncontrolled one whose dynamics are pushed to the limit at the driving envelope boundaries. Unfortunately, there is no available widely accepted benchmark for traditional vehicle stability systems like ABS, TCS, and ESC, making it impossible to provide reproducible performance comparisons. Each test result and discussion is presented in a particular subsection. At the end of this section, the time consumption of the experiments provided on Raspberry Pi 4 is shown to discuss the algorithm's potential to work in real-time.

The test vehicle used was "DemoCar," which is the most commonly utilized test vehicle in the CarMaker environment, for the purpose of reproducibility. Table 2.4 lists the general parameters of the car and control parameters. The project used in this thesis, which contains the implementation of a control strategy in the MATLAB/Simulink environment as well as in C++, is available on GitHub [57]. The basic programmed driver in the CarMaker software operated the test vehicle. All ride test videos have been made available on the YouTube channel of the author's research group [58] to facilitate a better understanding of vehicle motion during provided experiments.

Table 2.4: “DemoCar" and Control Parameters

Parameter	Symbol	Value	Units
Vehicle mass	m	1463	kg
Vehicle moment of inertia	I	1968	$\mathrm{kg\,m^2}$
Distance from CG to front axle	l_f	0.97	m
Distance from CG to rear axle	l_r	1.57	m
Maximum possible steering angle	δ_max	0.65	rad
Front tire lateral nominal stiffness	$c_{\alpha\mathrm{f}}$	15.4	rad^{-1}
Rear tire lateral nominal stiffness	$c_{\alpha\mathrm{r}}$	17.6	rad^{-1}
Half of axles width	w	0.789	m
Effective wheel radius	p	0.306	m
Drivetrain moment of inertia	I_w	2.4	$\mathrm{kg\,m^2}$
Steering column gain	k_steer	0.065	-
Braking system gain	k_brake	30	-
Engine control unit's linear gain	$k_{\mathrm{eng},1}$	1.95	-
Engine control unit's affine parameter	$k_{\mathrm{eng},2}$	10	-
Drivetrain gear coefficients from 1st to 5th gears	k_gear	$[12.92, 7.22, ...$ $5.13, 3.99, 3.04]$	-
Prediction horizon	N	3	-
Sampling time	T_s	0.005	s
Reference tracking linear weight	R_1	$[20,\ 8 \cdot 10^{-3}]$	-
Reference tracking quadratic weight	R_2	$\mathrm{diag}([20,\ 8{\cdot}10^{-3}])$	-
Fast input change penalty	R_{du}	$\mathrm{diag}([20,\ 0.45])$	-
Slew slack penalization	Q_i	$10^3 \cdot I_3$	-
Envelope slack penalization	Q_e	$10^4\mathrm{diag}([1,\ 1,\ 10^2])$	-
Rear axle sideslip angle boundary	$\alpha_{\mathrm{r,max}}$	0.4	rad
Front axle sideslip angle boundary	$\alpha_{\mathrm{f,max}}$	0.4	rad
Front wheels slip ratio boundary	$\lambda_{\mathrm{f,max}}$	0.3	-
Slew rate limit for steering angle	$\Delta u^{(1)}_\mathrm{max}$	$\frac{2\pi}{3} \cdot T_\mathrm{s}$	$\mathrm{rad\,s^{-1}}$
Slew rate limit for angular velocity	$\Delta u^{(2)}_\mathrm{max}$	$1000 \cdot T_\mathrm{s}$	$\mathrm{rad\,s^{-2}}$
Maximum steering angle	$u^{(1)}_\mathrm{max}$	0.65	rad
Proportional parameter of PI regulator	k_p	150	-
Integral parameter of PI regulator	k_i	1500	-

2.7.1 Sine with Dwell

Description

The sine with dwell experiment is a widely accepted method employed to assess the effectiveness of electronic stability control systems. This test deliberately induces oversteering maneuvers in the vehicle's dynamics, pushing its lateral capabilities to the absolute limits. Throughout this experimental setup, both the front and rear wheels of the vehicle actively generate the maximum lateral forces possible, as indicated by “case A" in Fig. 2.15. Ex-

ecuted on a standard road surface with an assumed friction coefficient of $\mu = 1$, the experiment initiates once the vehicle reaches a predetermined speed of $80\,\mathrm{km\,h^{-1}}$. This specific speed is chosen due to the tendency of an uncontrolled vehicle at this velocity to exhibit oversteering behavior. During the experiment, the driver disengages from the pedals and performs sinusoidal steering wheel movements, alternating between left and right. At the peak of the rightward position, there is a momentary pause of 0.5 s seconds before returning to the neutral position. The steering wheel motion is visually depicted in the reference signal presented in Fig. 2.16.

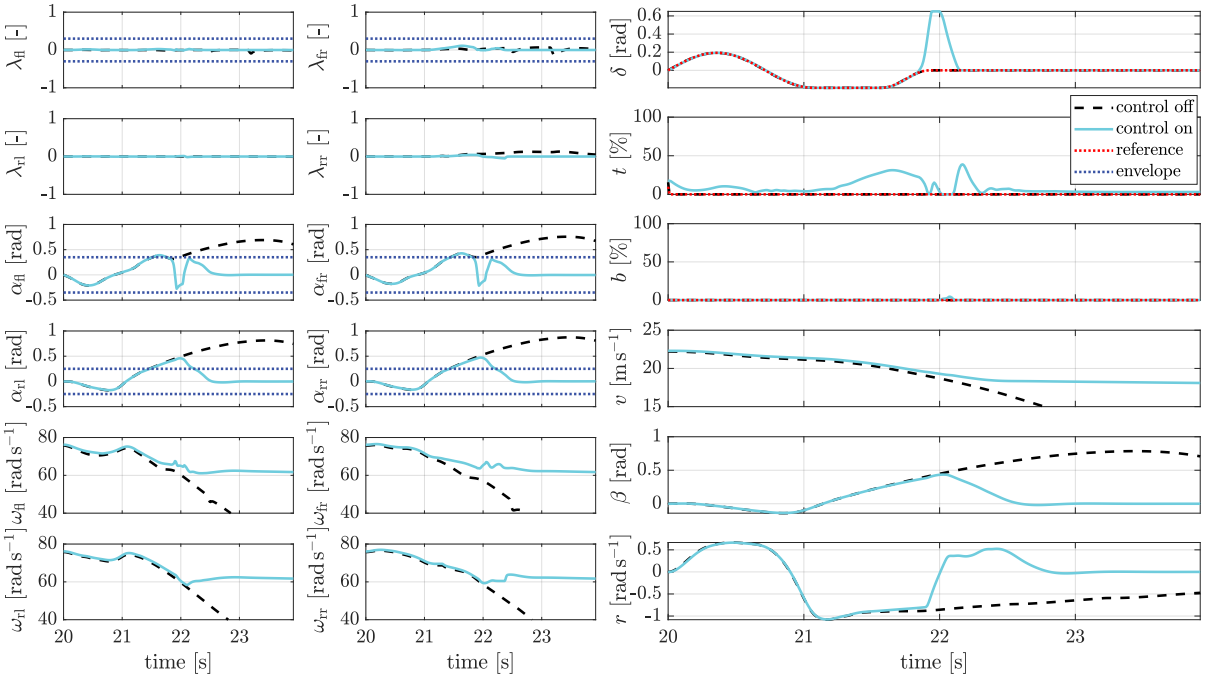

Figure 2.16: Sine with dwell at $80\,\mathrm{km\,h^{-1}}$. The DEP prevented a driving envelope violation with quick steering angle action in the direction of the skid. The baseline vehicle went to an uncontrolled skid.

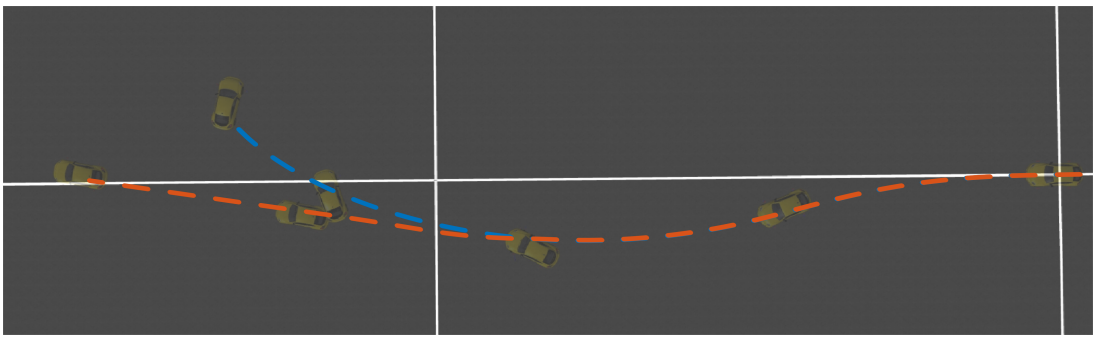

Figure 2.17: Vehicle trajectory during the sine with dwell test. Blue represents the trajectory of the uncontrolled vehicle, and orange represents the vehicle with DEP.

Discussion

Figure 2.16 illustrates crucial observations derived from the conducted experiment. It discloses the test failure of the uncontrolled vehicle, leading to a perilous skid. The trajectory of the skid is visually represented in Fig. 2.17. This undesirable outcome occurred as a consequence of the steering wheel turning left, causing the tires on both axles to approach their maximum leftward cornering capacities. Swiftly altering the vehicle's direction towards the opposite side induced a rapid change in force generation direction across both axles. Maintaining this position caused the vehicle to continue rotating, escalating the sideslip angle and diminishing traction on all wheels. Even returning the steering wheel to a neutral position did not stop this rotation due to inertia. The vehicle's dynamics required time to stabilize, introducing potential risks, especially at higher speeds.

To tackle this issue, instead of waiting for stabilization, the DEP promptly intervened by making adjustments to the steering wheel to control the sideslip angles, employing techniques akin to those taught in driving lessons. This rapid adjustment proved to be effective in stabilizing the car, aligning both the sideslip and yaw rate.

The dashed lines depicted in Fig. 2.16 delineate the boundaries within which the vehicle should ideally operate. Briefly surpassing these boundaries occurred due to the presence of soft constraints in the controller (2.42) and reliance on approximate vehicle dynamics. Nevertheless, subsequent experiments, as presented below, emphasize that occasional breaches of these boundaries can be deemed acceptable. This allowance is made to avoid unnecessary interventions by the controller, provided the driver possesses a deep understanding of the vehicle's dynamics.

2.7.2 Acceleration on a Slippery Surface with Instant μ Change

Description

Considering the practical aspect of this driving scenario, initiating movement from a standstill through acceleration is a common action for drivers. However, this seemingly routine maneuver has the potential to either compromise vehicle dynamics or markedly improve performance. To illustrate, an experiment was conducted, specifically addressing acceleration on a slippery surface. The goal was to highlight how the proposed controller adeptly mitigates wheelspin, all without the need for prior knowledge of low-friction conditions.

This specific evaluation replicates common testing scenarios for traction control systems. It entails the driving wheels applying maximum forward force, experiencing loss of traction on a slippery surface, and subsequently regaining traction on a dry asphalt section (referred to as "case B" in Fig. 2.15). The test initiates on a surface with significantly

reduced friction, approximately 60 % lower than the modeled asphalt value ($\mu = 0.4$). This low-friction surface spans 20 meters before transitioning to normal conditions with a friction coefficient of $\mu = 1$). On this latter segment of the road, a vehicle equipped with sufficient engine power can accelerate smoothly without any apparent issues. Figure 2.19 presents the experiment track from the bird-eye view, comparing both vehicles' trajectories.

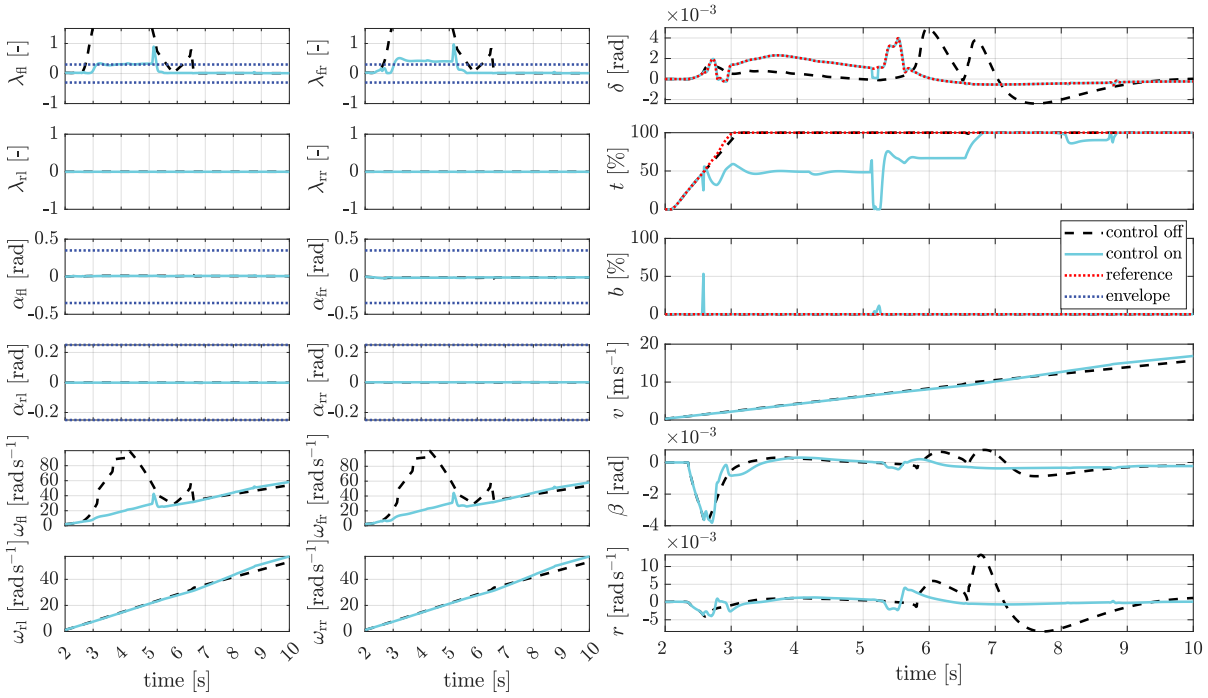

Figure 2.18: Acceleration on a slippery surface ($\mu = 0.4$) transitioning to asphalt ($\mu = 1$) at approximately 6.5 s. The DEP controller effectively reduced the wheelspin on the slippery surface, resulting in a significantly higher final velocity at the end of the experiment.

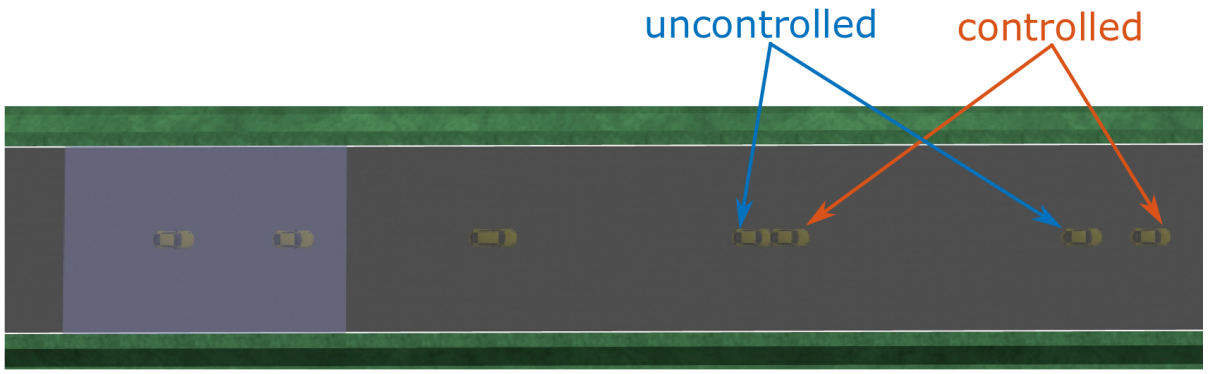

Figure 2.19: Vehicle trajectory during the acceleration test. Each pair of cars is presented after 2 seconds of motion.

Discussion

Figure 2.15 presents essential information derived from the simulation. The uncontrolled vehicle encountered a challenge involving excessive engine torque, leading to the front axle overspinning. As a result, the slip ratio of the driven wheels reached its peak, signifying a complete loss of traction. Despite this, these wheels retained some traction to propel the car forward, transitioning to a dry asphalt surface around 6.5 seconds into the experiment. A decrease in wheelspin occurred between 4 seconds and 5.5 seconds due to gear switching, during which the engine briefly disengaged, dissipating energy from the system. However, following the gear shift, the slip ratio increased again, persisting until the conclusion of the slippery surface segment.

Conversely, the vehicle equipped with the DEP controller managed to stay within the designated slip threshold by making throttle adjustments. There was only a single occurrence of exceeding the boundary, attributed to gear switching. Interestingly, during acceleration on the slippery surface, both vehicles exhibited minimal velocity disparities, while the angular velocity of the driven wheels fluctuated considerably. A significant contrast became evident when both cars regained traction on the dry asphalt surface.

Initially, the uncontrolled vehicle produced a lower longitudinal force as the driven wheels required time to synchronize their speed with the vehicle. In contrast, the vehicle under control promptly generated maximum traction force upon reaching the asphalt, resulting in a substantial speed advantage for the controlled vehicle beyond the 7-second mark.

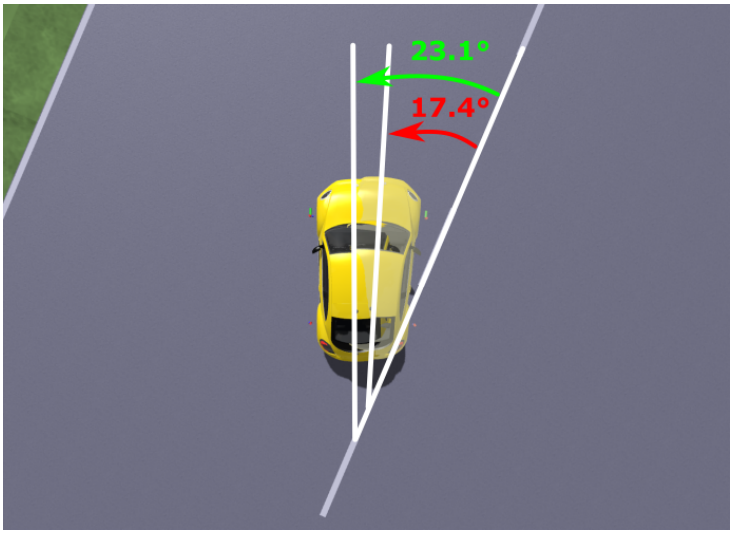

Figure 2.20: Lateral response of the vehicle with fully applied acceleration pedal. Unnecessary wheelspin reduces the baseline car's lateral maneuverability (ghost vehicle). The controlled vehicle (standard color) produced more lateral deviation on the same command from the steering wheel.

Unnecessary wheelspin reduces the vehicle's lateral maneuverability and can signifi-

cantly reduce the handling quality of the front wheels in the lateral direction once the slip ratio of the front wheels passes its peak value, as their lateral traction capabilities become exhausted. This can create dangerous situations if any lateral maneuver or disturbance occurs. Figure 2.20 presents the car's heading deviation after a step-like change of the steering wheel position during acceleration on a slippery surface. The vehicle equipped with the proposed DEP remained laterally controllable throughout the experiment and could produce more significant lateral deviations for the same amount of steering angle input due to the utilization of the combined slip for front wheels.

2.7.3 Full Stop during Cornering Maneuver

Description

A critical examination in validating the interplay between ABS and ESC systems involves a complete stop during a cornering maneuver. This test is designed to assess the vehicle's ability to steer the vehicle while executing sharp braking within a corner, as illustrated in "case C" in Fig. 2.15. The baseline test is executed on dry asphalt, taking into account the anticipated friction value of $\mu = 1$.

In this scenario, the vehicle initiates a consistent rightward cornering maneuver (see Fig. 2.22). Suddenly, at the commencement of the experiment, the driver promptly engages the brake pedal for abrupt braking. Owing to the vehicle's rotation, the inner side produces more longitudinal traction force compared to the outer side. This disparity in force arises from a higher slip ratio (correlated with the yaw rate) on the inner side and the effects of dynamic load transfer. This situation poses a risk of the inner wheel locking up and losing control, rendering it unable to generate the essential side force needed to maintain the vehicle on the intended path through steering wheel input.

Discussion

Figure 2.15 presents vital insights derived from the experiment. In the uncontrolled scenario, the right rear wheel experienced initial locking, followed by the left rear wheel after a short duration. Once the rear axle locks, even minor modifications in steering input can induce oversteering, rendering it exceptionally difficult to manage the vehicle's lateral dynamics solely through the steering wheel. Consequently, this led to the car spinning out of control towards the left side of the road, posing a significant risk of an accident, especially if other vehicles were approaching from the opposite direction.

Preventing such accidents entails slip management, achieved through the regulation of brake application. This is precisely the action taken by the DEP algorithm. It strategically eased off the brake to avert the locking of the right front wheel. This intervention

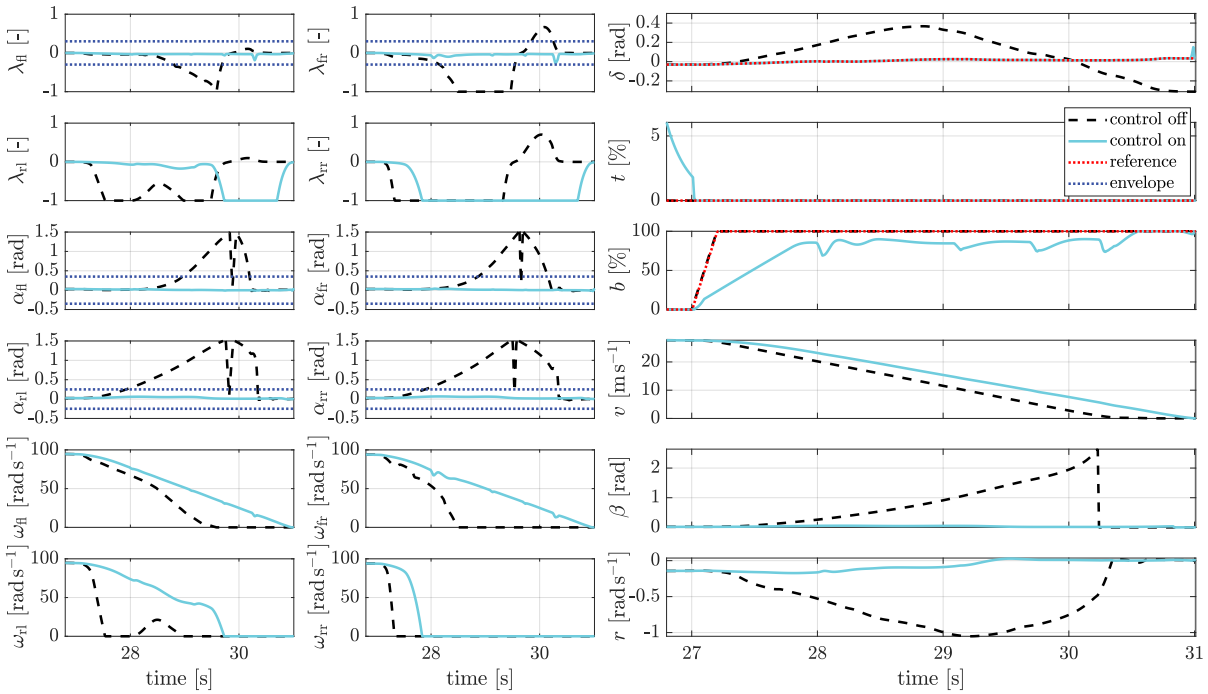

Figure 2.21: Braking test on asphalt from 120 km h^{-1} during cornering maneuver. The DEP controller maintained vehicle control by modulating braking. The uncontrolled baseline vehicle spun out of control due to the locked rear wheels.

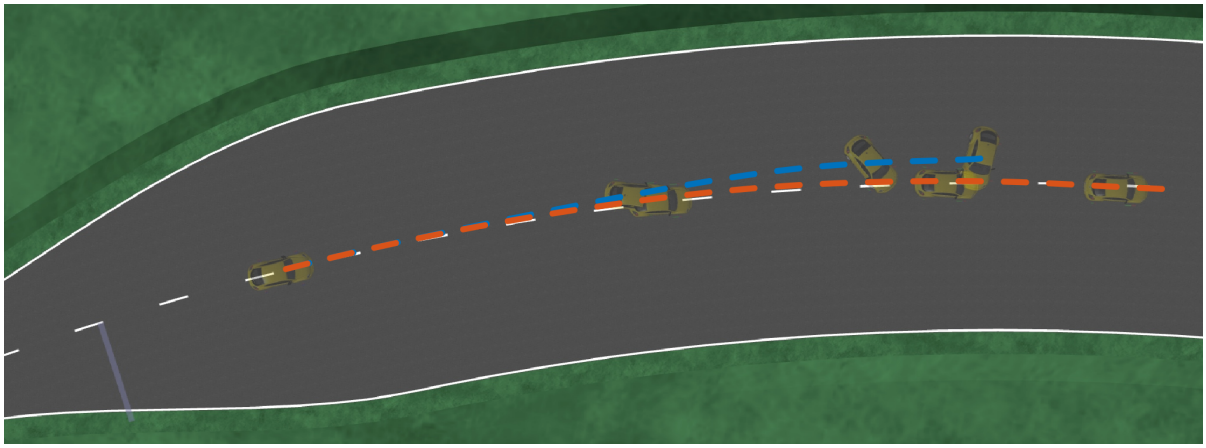

Figure 2.22: Vehicle trajectory during the braking test. Blue represents the trajectory of the uncontrolled vehicle, and orange represents the vehicle with DEP.

empowered the driver to steer the car in the correct direction and gradually stabilize it, even with the right rear wheel locked (while the left rear wheel remained unlocked, almost till the end of the experiment due to braking compensation during the experiment, capable of generating side force).

In the employed driving envelope protection method (2.42), the intentional exclusion of boundaries for the rear wheel slip ratio in the optimal control problem was done for simplicity. The aim was to demonstrate that, despite the vital role played by rear wheel slip ratio in ensuring vehicle stability, the showcased control approach can consistently ensure maneuver stability. This assertion remains valid even in the most challenging scenarios where data regarding the longitudinal slip of the rear wheels is not accessible. In instances where one of the rear wheels becomes locked, the vehicle equipped with this controller remains controllable and steerable by the driver.

2.7.4 Full Stop during Cornering Maneuver with μ-Split

Description

The optimal configuration for the controller presented assumes a foreknowledge of friction or load force. However, this experiment serves a twofold purpose: firstly, to delineate the constraints of the utilized control architecture, and secondly, to investigate a situation of complete frictional mismatch. To test the robustness of the controller and address these concerns, added complexity was introduced to the preceding corner braking test by employing a friction split pad. Deliberately diminishing friction on the crucial right side of the road heightened the traction capacity difference between the vehicle's left and right sides, resulting in a substantial 60 % reduction in potential traction. This experimental scenario corresponds to "case D" in Fig. 2.15. The experiment's test track can be observed in Fig. 2.24.

Typically, ABS implementations demonstrate a saw-like action during braking when wheel locking is detected [59]. This strategy aims to enhance the algorithm's robustness, especially when the traction limits of the specific road surface are unknown. By utilizing this behavior, the algorithm can effectively estimate road friction under the wheels over several saw-like periods, using it as a threshold to activate ABS operation. However, it's essential to highlight that the presented controller does not involve surface friction estimation; all controller parameters remain constant, and the overall control structure assumes a standard asphalt friction ($\mu = 1$). This prompts an intriguing question about how the controller would respond in such a scenario.

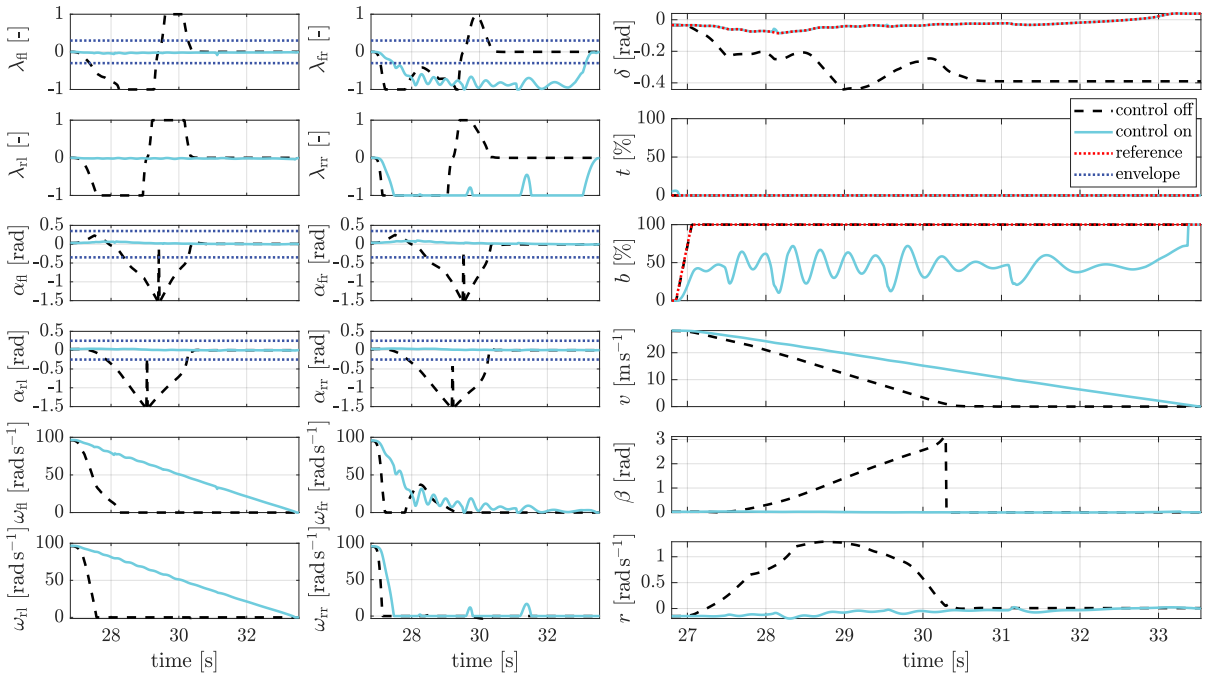

Figure 2.23: Braking on μ-split surface from 120 km h^{-1} during cornering maneuver. The right side of both vehicles was on a slippery road with $\mu = 0.4$. The left side remained on asphalt ($\mu = 1$.) The uncontrolled vehicle went into an uncontrolled spin. The controller had no information about the traction of the surface. However, it robustly protected the vehicle from losing maneuverability by reducing the brake pedal application.

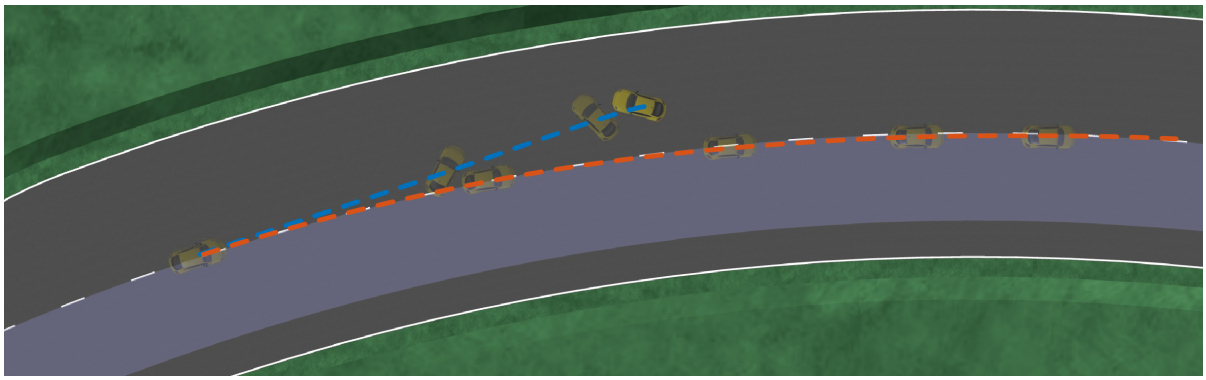

Figure 2.24: Vehicle trajectory during the braking with a split test. Blue represents the trajectory of the uncontrolled vehicle, and orange represents the vehicle with DEP.

Discussion

Figure 2.23 presents the results of the conducted experiment. The uncontrolled vehicle encountered a failure akin to the preceding test. However, in contrast, even in the face of the road's unmodeled and unknown friction properties, the demonstrated control framework successfully averted the full locking of the right front wheel – an integral element of this maneuver.

The braking duration of the controlled vehicle was prolonged because of the diminished longitudinal force capacity on the right side. An examination of Fig. 2.25, depicting the normalized traction ellipses during this experiment, reveals a reduced braking capability due to lower traction capacities on the car's right side. Although the controlled vehicle did not violate the traction ellipse boundaries, it exerted less braking force on the slippery surface. In contrast, the uncontrolled vehicle applied force beyond the tire's traction limits, surpassing the traction ellipse boundary and resulting in an uncontrollable spin.

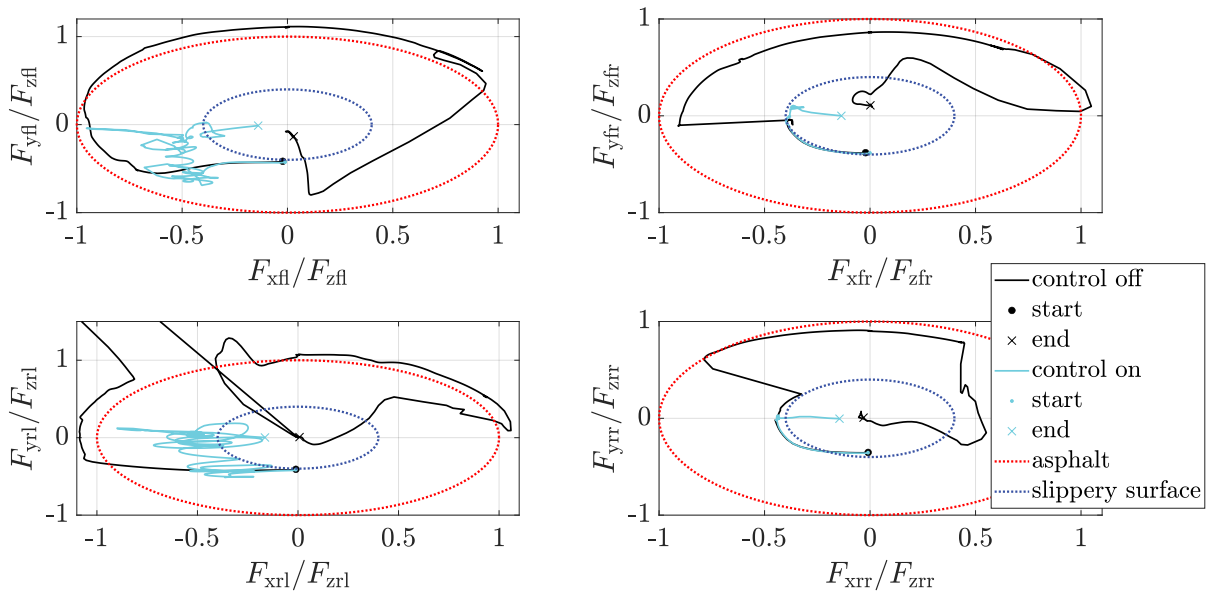

Figure 2.25: Normalized traction ellipses on wheels during μ-split braking experiment (time-series shown in Fig. 2.23). The right wheels were on the slippery surface, and the left wheels were on the asphalt. The uncontrolled vehicle initially lost traction on the right front wheel, which caused a loss of the vehicle's maneuverability. During cornering braking, the DEP protected wheel locking and kept the right wheels on the edge of their traction capacities.

An examination of Fig. 2.23 brings to light a breach of the driving envelope boundaries concerning the front right wheel. An investigation into the root cause of this infringement, as depicted in Fig. 2.26, unveils a notable constraint arising from the utilization of the single-track model within the MPC framework. This model, functioning based on mean values of angular velocities, may introduce disparities between wheels on the same axle, leading to deviations from real-world conditions.

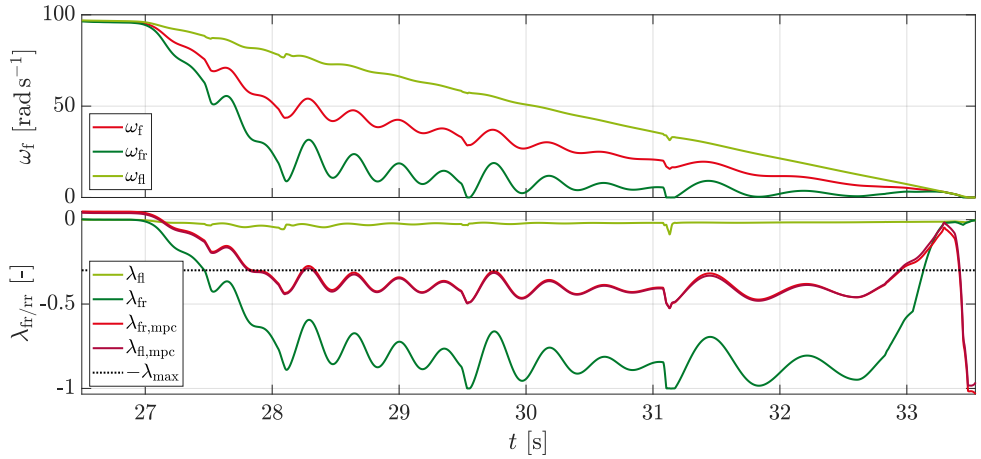

Figure 2.26: Wheel speeds and slip ratios during braking test on the split friction surface.

When the vehicle's sides encounter surfaces with differing traction properties, particularly during abrupt braking or rapid acceleration, the angular velocities of wheels on the same axle – such as the front left and right wheels – may exhibit significant divergence (in the presence of a differential). However, the single-track model operates based on mean values. This can lead to situations where, for example, the left wheel experiences almost negligible slip while the right wheel slips on a slippery surface, resulting in a mean value that remains permissible within the MPC's scope. In the context of this experiment, the controller's operation with the mean value, along with the soft constraints allowing slight traversal of the slip ratio boundary, contributed to this discrepancy. In reality, the right wheel was nearly locked.

Despite these discrepancies, which might be disconcerting for both the vehicle and the controller, they played a role in the vehicle's stabilization and the driver's retention of control. The current approach employs a global brake and accelerator strategy, but enhancing the controller for independent wheel braking/driving could significantly enhance performance, especially in scenarios with varied driving conditions like this experiment.

2.7.5 Time Consumption of the Experiments

The time for each iteration in the previously mentioned test scenarios was measured to evaluate the real-time suitability of the proposed algorithm on embedded hardware. These measurements serve as indicators of the algorithm's problem definition robustness and the solver's ability to handle numerical challenges, especially in complex scenarios.

The computationally demanding segments of the algorithm, involving the formulation of OCP matrices and the execution of the solver, were coded in C++. The complete implementation is available on GitHub [57]. Evaluations used closed-loop precomputed data from the earlier simulations implemented in Simulink. Raspberry Pi 4 executed this

code designed for embedded systems.

Throughout the assessments, the entire algorithm operated on a single thread on a CPU with a maximum frequency of 1.5 GHz. The elapsed time for each iteration was recorded and the resulting data is visually presented in Fig. 2.27, with statistical details available in Table 2.5.

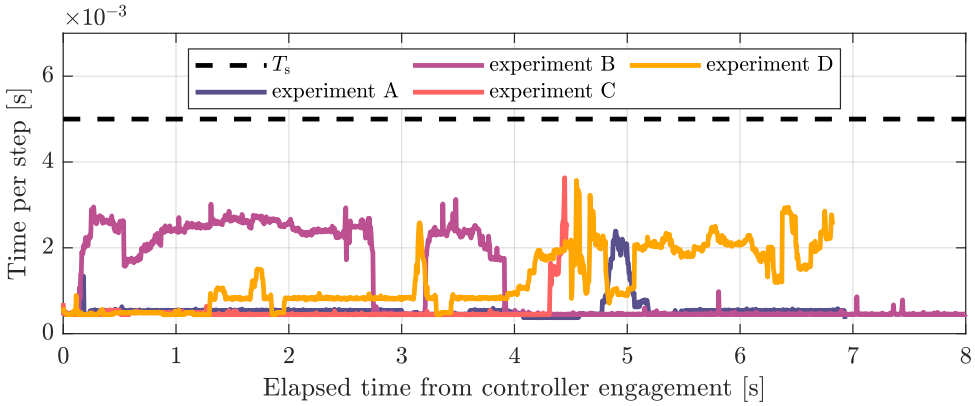

Figure 2.27: Individual step solution times of MPC for driving envelope protection across corresponding experiments.

Table 2.5: Statistics on Time Consumption

	Mean [s]	Median [s]	Max [s]
Experiment A	0.0006	0.0005	0.0024
Experiment B	0.0010	0.0005	0.0031
Experiment C	0.0005	0.0005	0.0036
Experiment D	0.0012	0.0008	0.0036

Upon initial examination, it becomes evident that every iteration required a duration shorter than the prescribed sampling period T_s, which is set at 0.005 s. This observation highlights the clearly defined nature of the OCP, indicating that the solver swiftly converges to an optimal solution without prolonged computational endeavors. Notably, both the mean and median time values are even more diminutive, signifying the rapid convergence of the solver, even when dealing with envelope boundaries that are either unviolated or closely approached.

Further scrutiny into the start of the acceleration experiment and the conclusion of braking experiments suggests that the solver necessitates increased computational resources when the vehicle's speed significantly diminishes, i.e., falls below $4\,\mathrm{m\,s^{-1}}$. This phenomenon is logically understandable since lower speeds intensify lateral vehicle dynamics, influencing the position of poles [60] and resulting in higher eigenvalues in matrix A_d in (2.7). Nonetheless, the expended time remains within reasonable limits and stays

below the sampling period. This ensures the derivation of new control values well in advance of their practical application.

2.8 Other Methods for Driving Envelope Protection

The primary solution for driving envelope protection presented earlier in section 2.6 is the focus of this work. It involves the use of linear model predictive control to protect the envelope constraints in a hard way, having complete control authority over the vehicle. However, there are alternative ways to protect the driving envelope, which are briefly discussed in this section.

2.8.1 Soft Envelope Protection of the Lateral Driving Envelope

This control architecture was presented at the IEEE Intelligent Vehicles Symposium in 2020 [61]. The main idea is to use haptic torque on the steering wheel, which is felt by the driver, to communicate the suggested control action from the model predictive control, which protects the lateral driving envelope.

In general, while driving, the driver mainly perceives the self-aligning torque on the steering wheel (as seen in Fig. 2.28), which results from the tension of the front tires and has a non-linear relationship with the sideslip angle of the front wheels. This relationship is illustrated in Fig. 2.29 and can be described using the simplified Pacejka Magic formula (2.12). The self-aligning torque provides drivers with additional information about their vehicle, particularly regarding the understanding of traction limits for the front tires, as its peak values occur around the same sideslip angles where the tire generates the maximum lateral traction force. However, this information does not provide insight into the rear axle's sideslip.

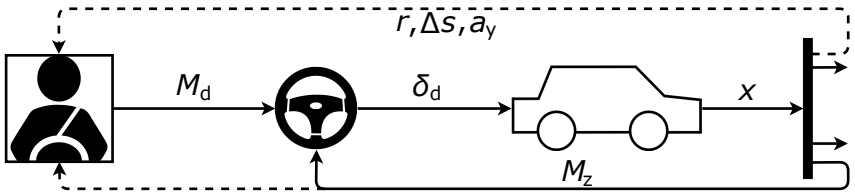

Figure 2.28: Standard platform configuration. The driver perceives vehicle response in the form of yaw rate r, lateral displacement of the vehicle Δs, and lateral acceleration a_y using the brain and feels self-aligning torque M_z on the steering wheel by their hands while commanding the steering angle δ_d applying steering torque M_d.

In contrast, the lateral driving envelope concept is developed based on the sideslip angles of the axles, making it possible to provide drivers with information about it. Furthermore, the haptic torque can be used to communicate how close the driver is to the

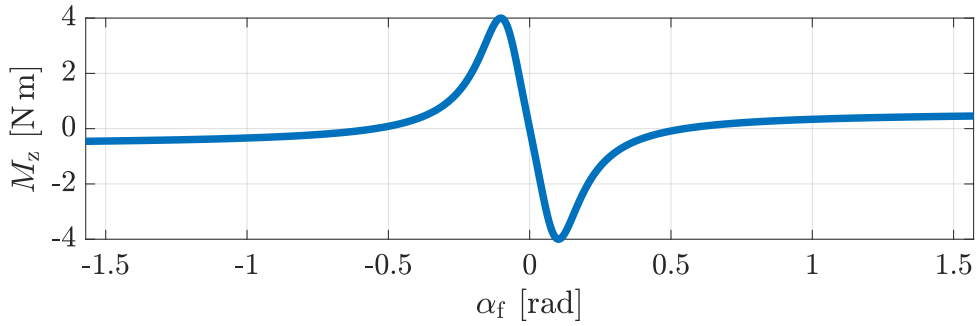

Figure 2.29: Dependency of produced self-aligning torque on the sideslip angle of front wheels.

envelope boundaries. As shown in Fig. 2.30, a feedback loop can be established where the envelope protection controller suggests “more suitable" steering angles based on vehicle dynamics and predefined constraints. The difference between the commanded and MPC steering angles is scaled by a linear parameter and sent to the steering wheel’s force feedback after limiting the rate of the signal and its amplitude.

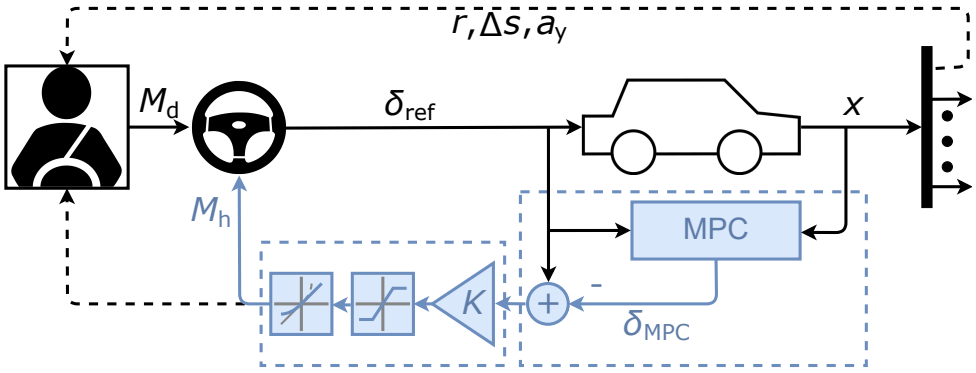

Figure 2.30: Proposed control architecture platform. The force feedback signal M_h is felt by the driver instead of self-aligning torque M_z. It is produced based on the guidance generated by the MPC, which is based on the actual steering angle of front wheels δ_{ref}, vehicle dynamics, and stability boundaries defined by the lateral driving envelope.

In [61], the model predictive control generates the steering angle. It is formulated as a constrained finite time OCP with quadratic objective function and linear constraints.

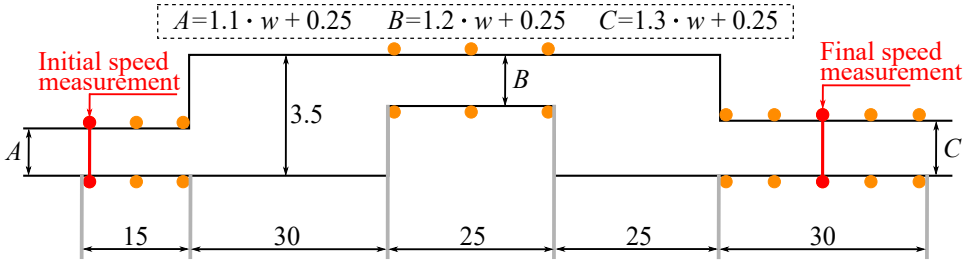

Figure 2.31: ISO 3888-1 double-lane change test specification [62]. All units are presented in meters. Parameters A, B, and C are linearly dependent on car width w.

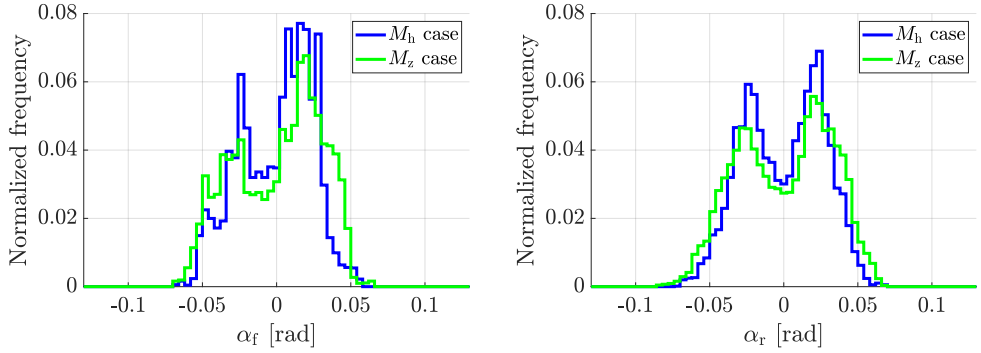

Figure 2.32: Histograms showcase the sideslip angles of the front (to the left) and rear (to the right) axles. The data was collected from the second and fourth parts of the double-lane change path, where the vehicle executes cornering maneuvers. The histogram demonstrates that with the M_h mode, drivers experienced a smaller variation in the sideslip angles of both axles.

Specifically, the MPC is given by

$$\min_{u_0,\dots,u_{N-1}} \sum_{k=0}^{N-1} x_k^\intercal Q_x x_k + (\delta_k - \delta_{\text{ref}})^\intercal Q_u (\delta_k - \delta_{\text{ref}}) \tag{2.50a}$$

$$\text{s.t.} \quad x_{k+1} = A_\text{d} x_k + B_\text{d} \delta_k, \tag{2.50b}$$

$$|\delta_k - \delta_{k-1}| \leq \Delta\delta_{\max}, \tag{2.50c}$$

$$|\alpha_{\text{f},k}| \leq \alpha_{\text{f,max}}, \tag{2.50d}$$

$$|\alpha_{\text{r},k}| \leq \alpha_{\text{r,max}}, \tag{2.50e}$$

$$x_0 = x(t), \; u_{-1} = u(t - T_\text{s}) \tag{2.50f}$$

where only the lateral dynamics of vehicle is considered with state vector $x = [\beta \quad r]^\intercal$, control input δ and matrices A_d and B_d were obtained by discretization (2.8) of matrix A and first column of matrix B from (2.5).

Upon comparing this MPC with the MPC for hard envelope protection (2.42), it is noticeable that the constraints for the combined slip are absent. Furthermore, there is no need to limit the maximum angle as the OCP aims to follow the commanded angle

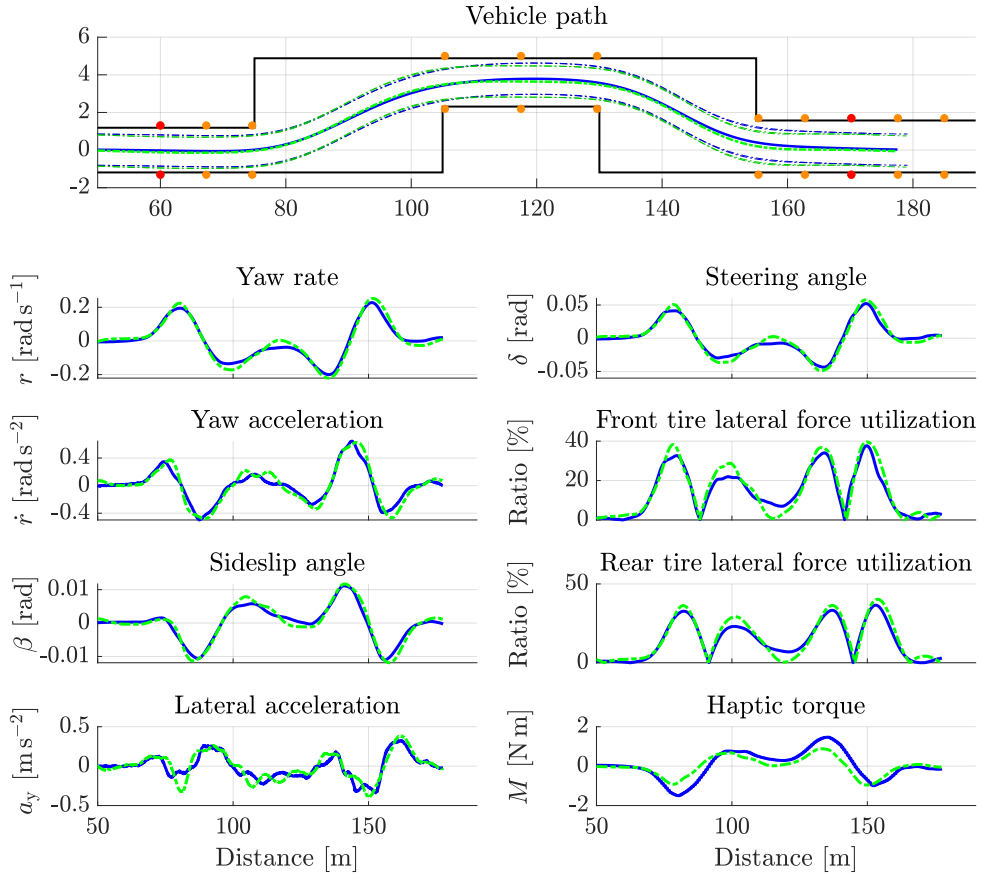

Figure 2.33: A comparison of mean successful rides started with the same initial velocity provided by all drivers for both modes. The solid blue line represents data from the ride with M_h mode, dashed green line – M_z.

closely, and if the OCP generates a more extensive suggested steering input, it would only increase the haptic torque for the driver. The objective function solely consists of a quadratic term for the reference track as there will always be a minor deviation from the reference signal that produces a small resistance torque on the steering wheel, providing the driver with some tactile feedback.

The algorithm was tested using a simulation environment and ten subjects who were briefly acquainted with the vehicle behavior, specifically on the double-lane change test depicted in Fig. 2.31. Two cases were compared: self-aligning torque M_z and haptic driver guidance torque M_h. Despite the uncommon feeling of such steering wheel behavior for test subjects, there was an overall increase in lateral tire utilization. This increase was due to smaller sideslip angles of both axles, resulting in greater margins concerning the driving envelope concept, as seen in Fig. 2.32. Furthermore, there was an increase in peak lateral tire force utilization, resulting in more agile vehicle behavior during the test evaluation, as shown in Fig. 2.33.

2.8.2 Lateral Driving Envelope Protection Using Cascade Control

The protection of driving envelope constraints can be achieved using various techniques, including the powerful model predictive control approach as was presented above. However, this method has limitations, as it requires robust hardware to calculate the optimal solution in each iteration. Flight envelope structures utilize hierarchical or structural control schemes, where each cascade part addresses a specific task, such as maintaining acceleration tracking or providing stability protection, as defined in [63]. This same concept can be applied to driving envelope protection. At the International Conference on Control, Automation, and Systems in 2021, a novel control scheme was presented, which changed the conventional driver sense [64]. Drivers generated a lateral acceleration of the vehicle using a steering wheel, which was tracked in the outer control loop. The inner control loops consisted of logic and feedback control that protects the lateral driving envelope constraints. Figure 2.34 schematically illustrates this concept.

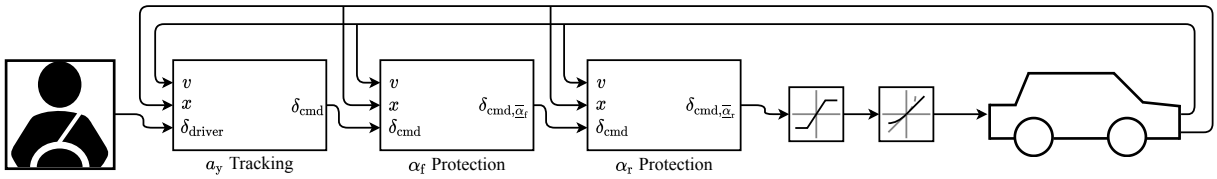

Figure 2.34: Schematic representation of the closed loop for cascade control. The primary objective of the outer loop is to generate and track a reference for lateral acceleration. Meanwhile, two inner loops are implemented to ensure that the sideslip angles of both axles remain within the driving envelope constraints. The output steering angle and its rate are limited before applying to the vehicle.

In the steering control system, the outer loop, presented in Fig. 2.35, has the responsibility of converting the commanded steering angle δ_{driver} from the steering wheel into the lateral acceleration at the vehicle's center of gravity a_{ref}. The maximal range of this conversion is determined by a tuning parameter $a_{\text{y,max}}$, which was set to the doubled gravitational acceleration 2g for the experiments conducted to make the dynamics fast. The lateral acceleration is subsequently converted into a reference for the yaw rate, as these two values are mathematically dependent on each other in a steady state as

$$r_{\text{ref}} = \frac{a_{\text{ref}}}{v}. \tag{2.51}$$

A PI controller then tracks the yaw rate reference, which generates the corresponding steering angle command δ_{cmd}.

In the α_{f} protection loop, the sideslip angle is calculated using a nonlinear formula

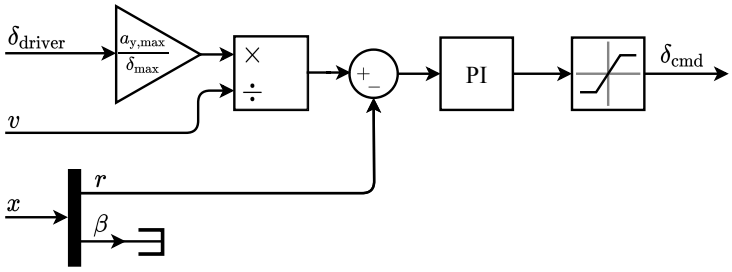

Figure 2.35: Lateral acceleration tracking block structure.

from [48], defined as,

$$\alpha_{\text{f,cmd}} = -\arctan \frac{(v \sin\beta + l_{\text{f}} r)\cos\delta_{\text{cmd}} - v\cos\beta\sin\delta_{\text{cmd}}}{|(v\sin\beta + l_{\text{f}} r)\sin\delta_{\text{cmd}} + v\cos\beta\cos\delta_{\text{cmd}}|}. \tag{2.52}$$

Suppose the estimated value of the sideslip angle exceeds the upper bound set by the driving envelope. In that case, the protection system will kick in and take over the control of the steering angle. This prevents the vehicle from violating the front sideslip angle envelope. In this case, the new steering angle is calculated using

$$\delta_{\overline{\alpha}_{\text{f}}} = \begin{cases} \delta_{\text{cmd}} & \text{, if } \alpha_{\text{f,cmd}} \leq \alpha_{\text{f,max}} \\ \alpha_{\text{f,max}} + \beta + \frac{l_{\text{f}}}{v} r & \text{, otherwise} \end{cases} \tag{2.53}$$

which involves using inverse linear kinematics to derive the control input at the edge of the envelope. Such a step is possible because the front sideslip angle directly depends on the steering angle without going through the vehicle dynamics. The same strategy can be used for the other side of the envelope to protect the minimal possible value of the sideslip angle.

On the other hand, the sideslip angle of the rear axle is dependent only on the vehicle dynamics states:

$$\alpha_{\text{r}} = -\arctan \frac{v\sin\beta - l_{\text{r}} r}{|v\cos\beta|} \tag{2.54}$$

and must be controlled using feedback control techniques. Suppose the value of α_{r} exceeds the upper limit. In that case, the protection system will activate and take over the steering angle command to prevent a violation of the rear wheel sideslip angle envelope. In this case, the steering angle is calculated using the following rule:

$$\delta_{\overline{\alpha}_{\text{r}}} = \begin{cases} \delta_{\text{cmd}} & \text{, if } \alpha_{\text{r}} \leq \alpha_{\text{r,max}} \\ k_{\text{r}}\alpha_{\text{r,max}} - Kx & \text{, otherwise} \end{cases} \tag{2.55}$$

where Kx is state feedback with a gain vector K, and k_r is a feed-forward term that sets the steady-state gain. The overall structure works in the same way as in the front wheel

case, where the rear wheel sideslip angle is kept on the envelope's edge to prevent it from violating the maximum allowable restriction.

To compute the state feedback gain vector K, the poles of the closed-loop are placed in desired positions on the stable half-plane. The feed-forward term is calculated using the state space matrices A_d and B_d, which are also used in (2.50), as

$$k_\mathrm{r} = -1/(C(A_\mathrm{d} - B_\mathrm{d}K)^{-1}B_\mathrm{d}). \tag{2.56}$$

Here, $C = [-1, \frac{l_\mathrm{r}}{v}]$ is used to follow the linear approximation of the rear wheel sideslip angle. The lower limit is protected in the same way.

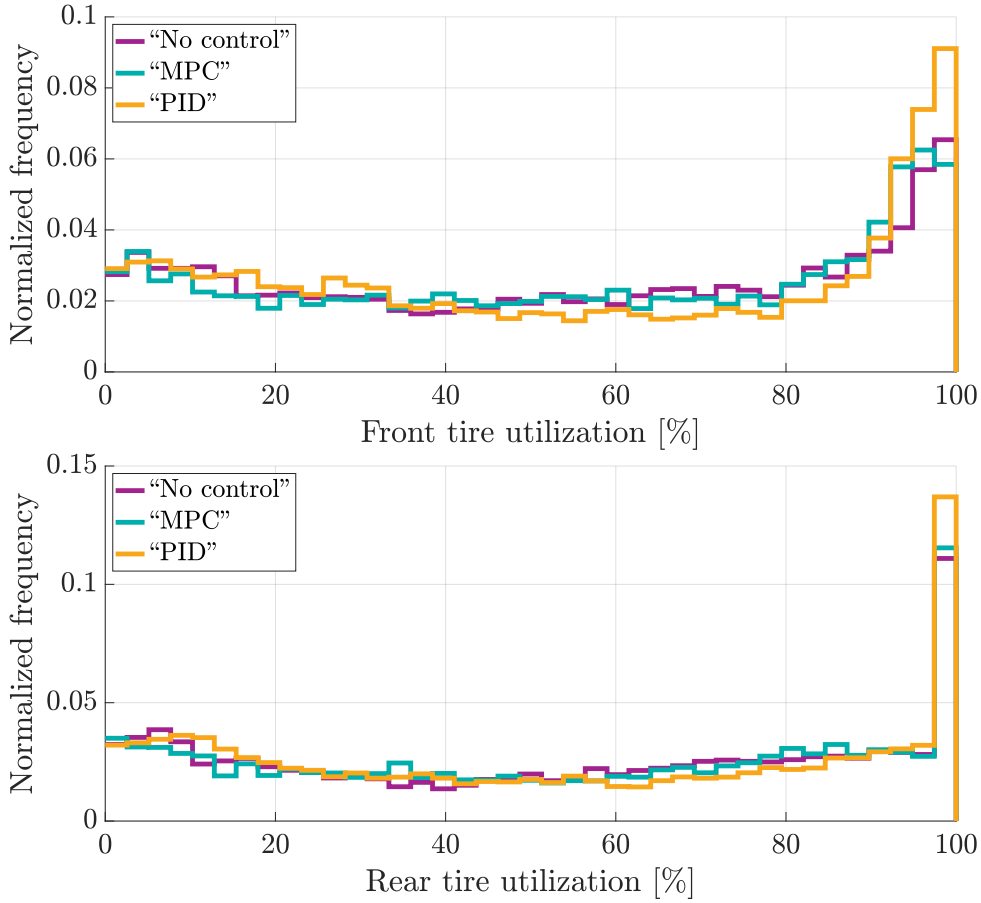

Figure 2.36: Histogram of tire utilization during cornering maneuvers. Tire utilization 100 % means that tires produce the maximal possible lateral force.

This study compared a control strategy with a model predictive control approach, as defined in (2.50), but for hard envelope protection, where the linear tracking term was used instead of quadratic to match the commanded steering angle precisely. The study also included an uncontrolled case where no assistance was given to the driver. Drive tests were conducted using a high-fidelity vehicle dynamics model on a racing simulator called "Live for Speed," with eight subjects of varying driving experiences. The statistical

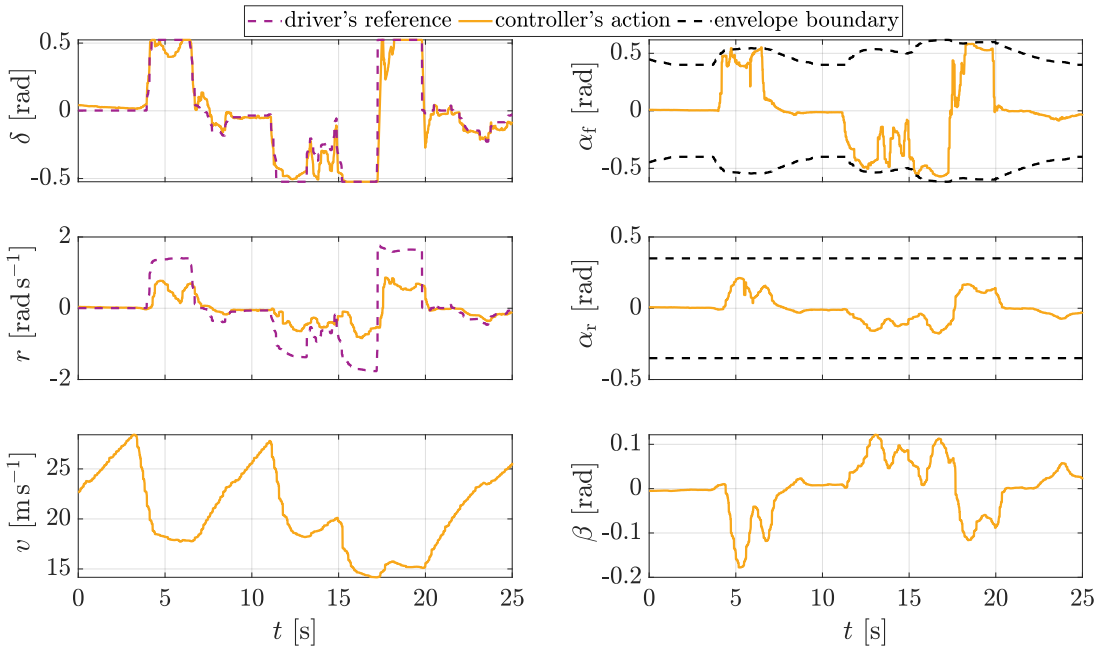

Figure 2.37: The performance of a cascade control structure on a serpentine road segment. In sharp turns, the desired yaw rate setpoint cannot be achieved due to the limitations of vehicle physics. However, the overall lateral dynamics are improved thanks to the preset used. The boundary for the sideslip angle of the front axle is not fixed and varies based on the current vehicle speed.

analysis of the results showed that the subjects preferred the model predictive control approach as it did not alter the vehicle's dynamics, which the human brain is capable of approximating on its own while driving. However, the cascade controller was found to increase tire utilization during cornering maneuvers, as illustrated in Fig. 2.36. These experiments demonstrate that introducing new advanced driver assistance systems can be challenging for automotive engineers. Nonetheless, the author believes that such control augmentation would be beneficial for control elements other than the classical steering wheel, such as, for instance, PC gamepads. Figure 2.37 shows controller functionality during a serpentine road segment. This output was generated using a PC gamepad, which can be seen in the dynamics of reference generation.

2.9 Discussion

This chapter presents a novel approach to characterizing vehicle stability by employing tire force limits and a control strategy that integrates various vehicle stability functions – such as ABS, ESC, TCS, and launch control – into a unified design through a single optimal control problem. The suggested controller exhibits remarkable effectiveness in addressing unstable maneuvers that could lead to wheel-skidding, locking, and spin for individual wheels, ensuring comprehensive stability in both lateral and longitudinal directions for

the entire vehicle.

The conducted experiments highlight the robustness of the controller, particularly its ability to withstand significant variations in driving surface traction characteristics. The controller's independence from the friction property of the driven surface is crucial to the chosen design approach for the stability envelope.

By consolidating all stability functions within a unified MPC framework, this approach resolves hierarchy issues among safety systems and integrates existing control systems. Notably, the definition of physical tire limits (2.25) plays a pivotal role in configuring safety systems and determining the vehicle's response across diverse settings.

Furthermore, the proposed control architecture demonstrates seamless operation on embedded hardware in real-time scenarios, indicating its potential applicability in real-world environments. Its adaptability to various car configurations and driving scenarios positions it as a versatile solution, ready to enhance vehicle stability and safety in different contexts within the automotive realm.

Lastly, the concept of the driving envelope can be applied in various ways and protected using different methods. Experiments conducted in section 2.8 reveal that employing at least the lateral part of the driving envelope concept can enhance tire utilization during cornering maneuvers.

Chapter 3

Environmental Envelope

In this chapter, the environmental envelope and an algorithm for its protection are introduced. The protection algorithm is implemented as a hard envelope protection strategy by the nonlinear model predictive control. Most of this chapter has been submitted and is currently under review for publication in the IEEE Transactions on Intelligent Transportation Systems in 2024 [65].

3.1 Introduction

The study of road accidents can reveal the main causes behind them. Data analysis [66] indicates that 94% of reported road incidents in the United States result from driver-related factors. Notably, 41% of these occurrences arise from errors in recognition, lapses in attention, or distractions, while 33% are attributed to incorrect decisions like driving too fast for the road conditions or misjudging traffic situations [66].

Mitigating these accidents involves two primary approaches. One approach underscores the continuous vigilance of vehicles in verifying and responding to driver commands, proactively preventing collisions, and ensuring adherence to road boundaries, such as [43]. Another solution entails transitioning to automated systems that take charge of decision-making, excluding the driver from the decision loop.

Research [67] demonstrates how the implementation of simple active yaw control can significantly diminish road departure accidents. Additionally, systems like lane-keeping contribute to further reduction of accident numbers [67]. While these systems, incorporating cameras for detecting lane markings [68], accompanied with some collision avoidance strategy, play a pivotal role in safety measures, they tend to focus on larger objects, neglecting smaller road hazards [69].

This dissertation presents an approach that seeks to revolutionize the traditional method by prioritizing vehicle safety from a wheel-centric viewpoint. The inspiration for

this stems from personal experiences navigating densely populated urban environments, where non-ideal road conditions frequently lead to significant vehicle damage and discomfort for occupants. This challenge extends beyond urban environments, impacting global highways [70]–[72]. For example, the research highlighted in paper [70] emphasizes that poor road conditions, particularly characterized by potholes, contribute to approximately 1.5% of road fatalities in India, ominously termed as 'killer potholes.'

Several methodologies exist for the automated detection of road potholes prior to accidents, utilizing technologies such as cameras [71] or ultrasonic sensors [70]. To the best of the author's knowledge, no research in the field of vehicle dynamics control specifically addresses small pothole avoidance. There are works on big pothole avoidance [73], [74], which decide to change a lane if the pothole is detected on the road, which is impractical for regular situations when, for example, only one lane exists. The approach proposed in this chapter not only tackles pothole avoidance but also encompasses smaller road hazards like debris, roadkill, and icy patches – elements that significantly reduce traction. Estimating the size and detecting smaller road objects can be accomplished through camera-based techniques, as suggested in [69]. Moreover, camera-based analysis can discern traction patches, as indicated by research outlined in [75]. Further research [76] employs cameras to estimate surface roughness in front of the vehicle, information that can enhance driving comfort in collaboration with the presented control strategy.

Additionally, this text underscores the adaptability and versatility of the presented control strategy, showcasing its effectiveness not only in addressing potholes and smaller hazards but also in navigating traditional obstacle avoidance scenarios involving larger entities such as vehicles or pedestrians, including obstacle prioritization.

However, considering the main focus on a short prediction horizon of 4-20 meters, a reasonable distance for detecting, classifying, and avoiding hazards, the objective is not to replace traditional collision avoidance systems, which typically involve phase planning. Instead, the goal is to augment overall functionality by serving as a middleware between high-level autonomous systems (or the driver, in the case of human-operated vehicles) and the low-level controller associated with vehicle dynamics or directly with actuators.

This chapter is organized as follows. Section 3.2 delves into the description of the general concept of the environmental envelope. Section 3.3 introduces the augmented vehicle model, which incorporates vehicle positioning and heading information. Section 3.4 explains the mathematical concepts of drivable roads, drivable obstacles, and undrivable obstacles. Section 3.5 focuses on the nonlinear model predictive control used for environmental envelope protection and offers valuable insights into its application. Section 3.6 describes the experiments that were carried out and provides a comprehensive analysis of the results. Finally, the concluding section offers a summary of the environmental

envelope topic, highlighting the key findings and conclusions.

3.2 General Concept

In this chapter, an advanced low-level road-keeping system is introduced, seamlessly integrated with collision avoidance, with the aim of emulating the reflex-like behavior observed in human drivers. Assumptions are made regarding the availability of critical information, including road lane or boundary coordinates in x, y-dimensions, as well as estimates of obstacle sizes, classification classes, and their coordinates on the road— all referenced to the vehicle's center of gravity (CG).

To shed light on the process, it is necessary to establish the terminology underpinning subsequent discussions. Envision the vehicle sensing its environment within a defined range, as illustrated by the green arc in Fig. 3.1. The *drivable road*, visually depicted as a shaded area, encapsulates the space between road boundaries (yellow curves). An *obstacle* is discerned as the part of the drivable road necessitating avoidance, outlined in red circles. Multiple obstacles can collectively represent complex shapes, such as vehicles or other objects.

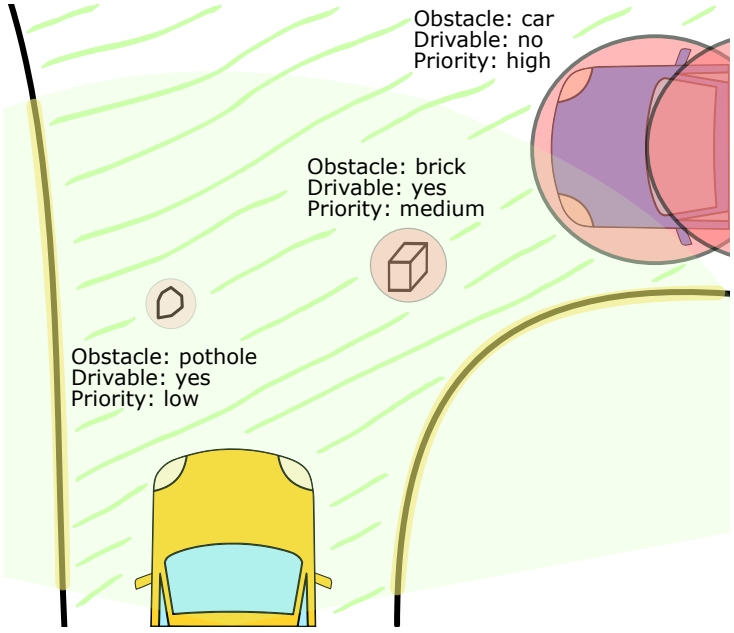

Figure 3.1: General idea behind the environmental envelope protection strategy.

Obstacles are categorized into two types: *drivable* and *undrivable*. A *drivable obstacle* encompasses anything the controlled vehicle can traverse, necessitating adjustments solely to the vehicle's wheels. These are objects with a height below a predetermined value (vehicle clearance). Conversely, *undrivable obstacles* are impassable by the vehicle itself. Each obstacle is assigned a priority, influencing subsequent optimization control,

contingent on its classification.

The proposed control strategy leverages the benefits of the steer-by-wire technology, allowing for fluid adjustments to the commanded steering angle. However, the system extends beyond the confines of steer-by-wire alone; it can be adapted for haptic torque or torque vectoring to accommodate diverse functionalities. The steering angle is optimized, whether directed by the driver or an autonomous driving algorithm, ensuring the car's wheel trajectories align with the drivable road, avoiding collisions with both drivable and undrivable obstacles. Ultimately, the vehicle trajectory is optimized to avoid undrivable obstacles.

The described control law takes the form of an optimal control problem, embodying a nonlinear model predictive control with boundaries defining wheel positions on the road. Named *environmental envelope protection*, this control law utilizes boundaries delineated by the drivable road and obstacles, crafting a so-called *environmental envelope*.

3.3 Vehicle Dynamics with Position and Orientation

The establishment of a dynamical model for a vehicle operating within a planar environment is crucial in understanding the environmental envelope and ensuring its protection. Various approaches exist for vehicle modeling, ranging from kinematic models [8] to highly nonlinear twin-track models [77] incorporating complex or linearized tire models. Therefore, assumptions and guidance criteria need articulation from the outset.

First and foremost, consideration is given to a short, sensible distance of the road in front of the vehicle, resulting in a small prediction horizon. A 0.5-second prediction horizon is adopted for this work, implying two key ideas: constant vehicle velocity over the entire prediction horizon, given the negligible alteration of vehicle dynamics within such a brief timeframe, and a limited heading change not exceeding 30 degrees due to the short prediction horizon.

Both factors mentioned above suggest potential decoupling of vehicle dynamics, allowing utilization of only the lateral part. Additionally, trigonometrical functions related to heading can be effectively linearized using the small angle assumption.

A simple kinematic model is deemed insufficient as it fails to capture vehicle dynamics and may not be suitable for more aggressive maneuvers. Two possible choices of dynamical models emerge: single-track and twin-track. Given the classical steering by the front axle without traction control and independent steering employed in this work, the single-track model is considered appropriate due to its fewer states and lower computational demand inside the control loop. The only requirement from the twin-track model, the calculation of wheel positions in the environment, can be provided within the optimization problem

without involving the twin-track model.

In vehicle path-generation and tracking studies, researchers commonly employ nonlinear mathematical models [78], [79]. However, due to the short prediction horizon and the need for real-time computation on embedded hardware, the linear version of the single track is considered a more suitable dynamical model for this task.

Therefore, as a reference model for the model predictive control, the linearized single-track model from (2.4) with additional states for vehicle position and heading can be incorporated to obtain the necessary mathematical description. The used schematic configuration of the linearized single-track and notation for position and orientation states are depicted in Fig. 3.2 and 3.3, respectively. Variables and parameters of the mathematical model are listed in Table 3.1. The continuous-time dynamics can be represented in the state-space form, which will be used in the text below as:

$$\dot{x}(t) = Ax(t) + Bu(t) + q \tag{3.1}$$

where state and input vectors are combined to

$$x = \begin{bmatrix} \beta & r & p_{\mathrm{x}} & p_{\mathrm{y}} & \psi \end{bmatrix}^{\top}, \quad u = \begin{bmatrix} \delta \end{bmatrix} \tag{3.2}$$

and system matrices are derived as:

$$A = \begin{bmatrix} -\dfrac{c_{\mathrm{f}}F_{\mathrm{zf}} + c_{\mathrm{r}}F_{\mathrm{zr}}}{mv} & \dfrac{l_{\mathrm{r}}c_{\mathrm{r}}F_{\mathrm{zr}} - l_{\mathrm{f}}c_{\mathrm{f}}F_{\mathrm{zf}}}{mv^2} - 1 & 0 & 0 & 0 \\ \dfrac{l_{\mathrm{r}}c_{\mathrm{r}}F_{\mathrm{zr}} - l_{\mathrm{f}}c_{\mathrm{f}}F_{\mathrm{zf}}}{I} & -\dfrac{l_{\mathrm{r}}^2c_{\mathrm{r}}F_{\mathrm{zr}} + l_{\mathrm{f}}^2c_{\mathrm{f}}F_{\mathrm{zf}}}{vI} & 0 & 0 & 0 \\ 0 & 0 & 0 & 0 & 0 \\ v & 0 & 0 & 0 & v \\ 0 & 1 & 0 & 0 & 0 \end{bmatrix}, \tag{3.3}$$

$$B = \begin{bmatrix} \dfrac{c_{\mathrm{f}}F_{\mathrm{zf}}}{mv} & \dfrac{l_{\mathrm{f}}c_{\mathrm{f}}F_{\mathrm{zf}}}{I} & 0 & 0 & 0 \end{bmatrix}^{\top}, \quad q = \begin{bmatrix} 0 & 0 & v & 0 & 0 \end{bmatrix}^{\top}. \tag{3.4}$$

Assuming the vehicle's speed v and load forces for the front F_{zf} and rear F_{zr} axles as time-variant parameters of the model in the matrices above enables broad simulation scenarios. However, they are kept constant for one prediction horizon to simplify the dynamical model.

For the purpose of designing the MPC strategy, the discrete-time vehicle dynamics defined as:

$$x_{k+1} = A_{\mathrm{d}}x_k + B_{\mathrm{d}}u_k + q_{\mathrm{d}} \tag{3.5}$$

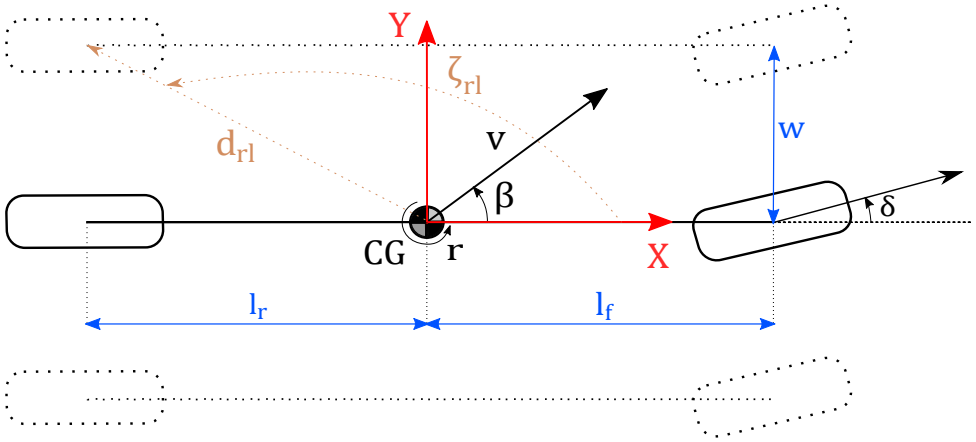

Figure 3.2: The single-track model (CG stands for the center of gravity).

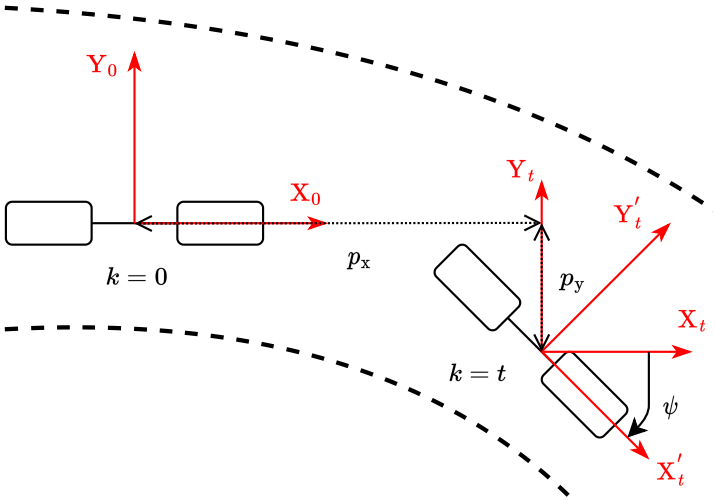

Figure 3.3: The inertial reference frame is always defined from the vehicle's initial position at time $k = 0$. The position of the car p_{x} and p_{y} and its heading ψ are calculated relative to the initial state.

is used, which was obtained by Euler discretization defined by the following equalities:

$$A_{\mathrm{d}} = I + T_{\mathrm{s}}A, \quad B_{\mathrm{d}} = T_{\mathrm{s}}B, \quad \text{and} \quad q_{\mathrm{d}} = T_{\mathrm{s}}q \tag{3.6}$$

of the continuous-time system from (3.1) with sampling time T_{s}.

The position of each wheel is calculated from its placement according to the CG and updated with the change of vehicle states during the simulation as:

$$\begin{bmatrix} p_{\mathrm{x}ij} \\ p_{\mathrm{y}ij} \end{bmatrix} = \begin{bmatrix} p_{\mathrm{x}} \\ p_{\mathrm{y}} \end{bmatrix} + d_{ij} \begin{bmatrix} \cos(\zeta_{ij} + \psi) \\ \sin(\zeta_{ij} + \psi) \end{bmatrix} \tag{3.7}$$

where $i \in \{\mathrm{f}, \mathrm{r}\}$ and $j \in \{\mathrm{l}, \mathrm{r}\}$. Variable d_{ij} stands for the distance between the CG and

Table 3.1: Vehicle Model Notation

Description	Symbol	Units
Vehicle speed at CG	v	$\mathrm{m\,s^{-1}}$
Sideslip angle at CG	β	rad
Yaw rate at CG	r	$\mathrm{rad\,s^{-1}}$
Steering angle of the front axle	δ	rad
[Lateral, longitudinal] position coordinate of the CG w.r.t. inertial frame	$p_{[\mathrm{y,x}]}$	m
Heading of the vehicle w.r.t. inertial heading	ψ	rad
Distance from CG to [front, rear] [left, right] wheel	$d_{[\mathrm{f,r}]\ [\mathrm{l,r}]}$	m
Angle from X-axis to [front, rear] [left, right] wheel	$\zeta_{[\mathrm{f,r}]\ [\mathrm{l,r}]}$	rad
[Lateral, longitudinal] position coordinate of [front, rear] [left, right] wheel w.r.t. inertial frame	$p_{[\mathrm{x,y}]\ [\mathrm{f,r}]\ [\mathrm{l,r}]}$	m
Load force of [front, rear] axle	$F_{\mathrm{z}[\mathrm{f,r}]}$	N
Vehicle mass	m	kg
Yaw moment of inertia at CG	I	$\mathrm{kg\,m^2}$
Distance from CG to [front, rear] axle	$l_{[\mathrm{f,r}]}$	m
Lateral tires nominal stiffness of [front, rear] axle	$c_{[\mathrm{f,r}]}$	$\mathrm{rad^{-1}}$
Half of axle width	w	m

a wheel's anchor point and is computed as:

$$d_{ij} = \sqrt{l_i^2 + w^2} \tag{3.8}$$

while anchor angle ζ is defined as:

$$\zeta_{ij} = \pm \arctan \frac{w}{l_i} \tag{3.9}$$

and becomes positive for the left side of the vehicle and negative for the right side.

A precise calculation of the position of wheels is not necessary, as some inaccuracy can be tolerated by the controller due to the significantly short prediction horizon. In order to reduce computational consumption inside the MPC, the fact that the change in the vehicle's heading for a short prediction horizon is small (less than 30 degrees) can be utilized again. As a result, a linear approximation of (3.7) can be used instead of the nonlinear equation defined as:

$$\begin{bmatrix} p_{\mathrm{x}ij} \\ p_{\mathrm{y}ij} \end{bmatrix} \approx \begin{bmatrix} p_{\mathrm{x}} \\ p_{\mathrm{y}} \end{bmatrix} + d_{ij} \begin{bmatrix} \cos\zeta_{ij} - \psi \sin\zeta_{ij} \\ \sin\zeta_{ij} + \psi \cos\zeta_{ij} \end{bmatrix} \tag{3.10}$$

where sines and cosines become constant parameters as anchor angles are unchanged, and

the following approximations were used:

$$\sin\psi \approx \psi, \quad \cos\psi \approx 1. \tag{3.11}$$

The positions of wheels (3.10) are then used to define the constraints of the environmental envelope inside the MPC.

3.4 Definition of the Environmental Envelope

The concept of the environmental envelope is expressed as a compilation of points within the coordinate frame of the vehicle, representing navigable regions within the environment. These regions encompass pathways accessible to both the vehicle and the wheels. Within this conceptual framework, three essential terms are introduced: *drivable road*, *drivable obstacles*, and *undrivable obstacles*. The focus of this section is on formulating mathematical expressions for these terms. The definition of the environmental envelope sets the boundaries for optimal control protection, serving as a guardian against violations.

3.4.1 Drivable Road Model Representation

Roads typically consist of three primary types of segments: linear sections, circular arcs, and clothoids [80]. The first experiment showcases these road segment types (Fig. 3.6). When modeling drivable roads, the system aims to effectively approximate each segment type, focusing on relatively short distances. Unlike conventional path-planning approaches that often use clothoid approximations for defining smooth vehicle paths over longer distances [80], the proposed system concentrates on significantly shorter distances.

Polynomial approximations of road boundaries are chosen to streamline computational complexity. Linear approximations suffice for modeling straight road segments effectively. However, accurate representation of short circular arcs requires parabolic approximations. A cubic parabola approximation is crucial for intricate design elements like clothoids due to its inflection point connecting two circular arcs with clockwise and anti-clockwise rotation directions. These approximations are widely used in vehicle applications for road lane modeling, including adaptive cruise control, collision warning systems, etc [81]. The experiment section provides a detailed discussion on the accuracy of distinct polynomial approximations across various road segments, with Table 3.3 presenting the precision of different approximations.

In representing the drivable road, a pair of road boundaries described by cubic parabo-

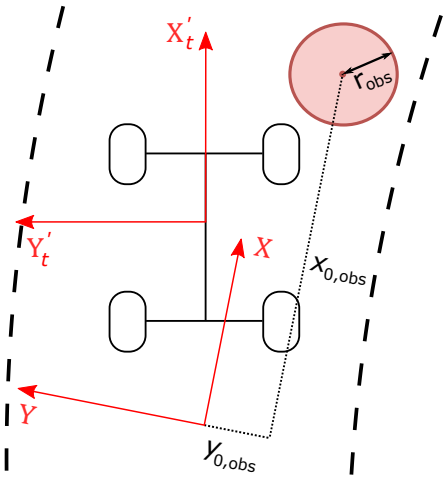

(a) Regular road with left and right boundary. A drivable obstacle (e.g., pothole) is presented as a restricted circle in the vehicle coordinate frame.

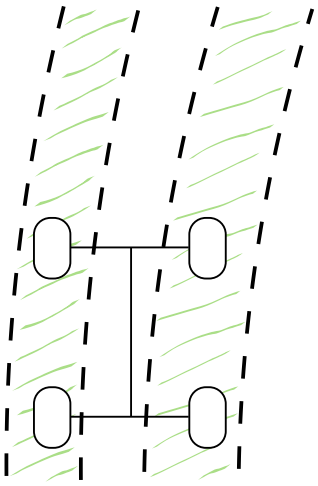

(b) The drivable road is defined as ruts for the left and right sides of the vehicle.

Figure 3.4: Two possibilities of drivable road definition concerning the used modeling technique. The drivable obstacle representation on the drivable road is shown on the left.

las is utilized, defined as:

$$y_{\text{road}} = a_3 x_{\text{road}}^3 + a_2 x_{\text{road}}^2 + a_1 x_{\text{road}} + a_0 \tag{3.12}$$

where coefficients a_n ($n \in [0, 1, 2, 3]$) are derived via curve fitting using the least mean square method with data points collected from vision perception units. Incorporating the constraints of the drivable road into the model predictive control involves considering the boundaries governing the position of each wheel, ensuring they remain within two parabolic constraints. This formulation allows for overarching constraints for the drivable surface while accommodating specific constraints for individual wheels. For instance, it enables redefining certain drivable areas from a wheel perspective, allowing for high-accuracy vehicle guidance. Possible applications include road ruts on snowy terrain or paths within forested rural roads, among others, allowing for more precise vehicle guidance. Both these concepts are illustrated in Fig. 3.4.

3.4.2 Drivable Obstacle Model Representation

In order to introduce a constraint for the drivable obstacle, circles (or ellipses in general) are used and defined as:

$$(x_{\text{obs}} - x_{0,\text{obs}})^2 + (y_{\text{obs}} - y_{0,\text{obs}})^2 = (r_{\text{obs}})^2 \tag{3.13}$$

where $r_{\text{obs}} \in R_{\text{obs}}$ represents the radius of the circle that bounds an obstacle, and $x_{0,\text{obs}} \in X_{0,\text{obs}}$ and $y_{0,\text{obs}} \in Y_{0,\text{obs}}$ are position coordinates with respect to the inertial frame. Sets R_{obs}, $X_{0,\text{obs}}$, and $Y_{0,\text{obs}}$ contain the position and sizes of all detected obstacles. An illustrative representation of such an obstacle is depicted in Fig. 3.4. The circle function was introduced due to its twice differentiable property. Such an obstacle modeling approach can be found in literature, as it is utilized generally in optimization-based and force-field methods [82], [83].

The same modeling principle is utilized if the obstacle cannot be driven over, meaning that it is higher than the height of the chassis. In the case of undrivable obstacles, additional limitations are imposed on the front axle's position to guarantee it resides outside this circle. This serves to increase the "price" in the algorithm for the vehicle traversing such obstacles. Comprehensive explanations of these constraints are provided in the subsequent section.

3.5 Control Strategy for Environmental Envelope Protection

The depicted schematic representation in Fig. 3.5 outlines the proposed control structure, encompassing five crucial steps:

1) Obtaining road boundary data and approximating it through cubic parabolas.

2) Estimating obstacle positions, sizes, heights, and classifications.

3) Measuring and estimating the dynamic signals of the vehicle.

4) Retrieving the commanded driver's steering angle, tracked as the control reference.

5) Actively tracking the commanded steering angle through model predictive control while adhering to constraints related to drivable roads and drivable/undrivable obstacles.

The reference model within MPC initiates at zero initial position and heading in each step, incorporating estimated β_0 and r_0.

This work refrains from delving into the methodology for estimating road boundaries and obstacle properties. For detailed methods, references are made to [68], [69], [71], [75]. In experiments conducted using IPG CarMaker, direct signal measurements for step 3 are relied upon. However, various alternative algorithms exist, proposing diverse approaches to successfully estimate required signals via standard vehicle measurements [84], [85]. The focus is directed toward the mathematical optimization problem outlined in step 5 and the underlying logic behind it.

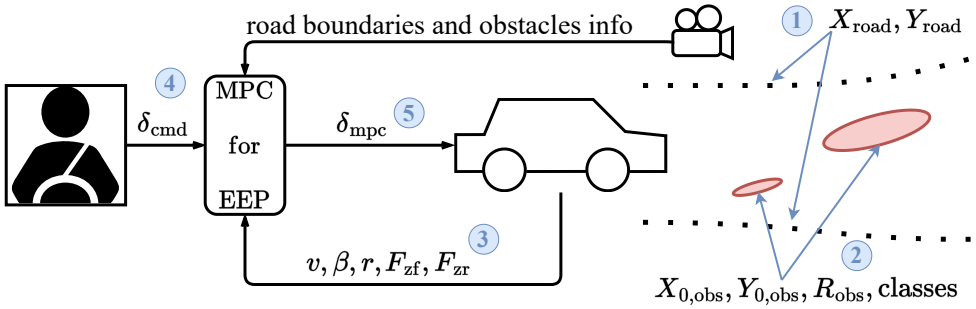

Figure 3.5: Schematic representation of the control strategy. The visual perception system supplies the positions of road boundaries in $X_{\text{road}}, Y_{\text{road}}$, and obstacles in $X_{0,\text{obs}}, Y_{0,\text{obs}}$. The radii of obstacles are encapsulated within the matrix R_{obs}.

The activation of the proposed control strategy is contingent solely upon the vehicle speed surpassing the predetermined limit (for example, this work uses $v \approx 4\,\text{m}\,\text{s}^{-1}$). This precautionary measure aims to prevent division by zero speed in (3.3) and associated numerical issues. Utilizing the kinematic vehicle model, such as described one in Chapter 2 of [8], effectively characterizes vehicle motion, even at such low speeds, enabling the application of this algorithm for lower velocities.

The formulation of the MPC strategy is provided in the form of a nonlinear nonconvex constrained finite time optimal control problem (OCP). The OCP is repeatedly solved in the receding horizon fashion [53]. The OCP is defined as:

$$\min_{u_0,\ldots,u_{N-1}} \sum_{k=0}^{N-1} \Big(R_1 \left|\delta_{\text{cmd}} - u_k\right| + R_2(\delta_{\text{cmd}} - u_k)^2 \tag{3.14a}$$

$$+ R_{\text{du}}(u_k - u_{k-1})^2 + R_u u_k^2 + x_k^\intercal R_x x_k \Big) \tag{3.14b}$$

$$+ \sum_{k=0}^{N} \left[s_{\text{i},k}^\intercal Q_{\text{i}} s_{\text{i},k} + s_{\text{eo},k}^\intercal W Q_{\text{eo}} s_{\text{eo},k} + s_{\text{eb},k}^\intercal Q_{\text{eb}} s_{\text{eb},k} \right] \tag{3.14c}$$

$$\text{s.t.} \quad x_{k+1} = A_{\text{d}} x_k + B_{\text{d}} u_k + q_{\text{d}}, \tag{3.14d}$$

$$|u_k - u_{k-1}| \leq \Delta u_{\max} + s_{\text{i}}, \tag{3.14e}$$

$$|u_k| \leq u_{\max}, \tag{3.14f}$$

$$s_{\text{i},k} \geq 0, \tag{3.14g}$$

$$(p_{\text{x}ij,k}, p_{\text{y}ij,k}) \notin (X_{\text{obs}}, Y_{\text{obs}}), \tag{3.14h}$$

$$s_{\text{eo},k} \geq 0, \tag{3.14i}$$

$$(p_{\text{x}ij,k}, p_{\text{y}ij,k}) \in (X_{\text{road}}, Y_{\text{road}}), \tag{3.14j}$$

$$s_{\text{eb},k} \geq 0, \tag{3.14k}$$

$$x_0 = \begin{bmatrix} \beta(t) & r(t) & 0 & 0 & 0 \end{bmatrix}^\intercal, \tag{3.14l}$$

$$u_{-1} = u(t - T_{\text{s}}) \tag{3.14m}$$

with a linear-quadratic objective function (3.14a) - (3.14c), defined over the prediction horizon N, where k denotes the prediction step. Variable t stands for the time of initialization. As it can be seen from (3.14a) - (3.14c), the size of the control horizon is set to be equal to the prediction horizon N. All parameters used for the control strategy are listed in Table 3.2.

Table 3.2: Control Variables

Parameter	Symbol	Value
Prediction horizon	N	10
Sampling time	T_s	0.05 s
Reference tracking linear weight	R_1	10^3
Reference tracking quadratic weight	R_2	10^3
Fast input change penalty	$R_{\mathrm{d}u}$	10^2
High input penalty	R_u	10^2
High state penalty	R_x	diag([50, 0, 0, 0, 0])
Slew slack penalization	Q_i	10^{10}
Envelope obstacle slack penalization	Q_eo	10^3
Envelope road boundary slack penalization	Q_eb	10^4
Slew rate limit for steering angle	Δu_max	$\frac{4\pi}{3} \cdot T_\mathrm{s}$ rad s^{-1}
Maximum steering angle	u_max	0.65 rad
Safe distance from road border	σ	0.2 m

The primary objective of the controller (3.14) is to closely track the commanded steering angle. The objective function (3.14a) simultaneously incorporates the first and second norms to the reference to achieve this. The quadratic term penalizes significant deviations from the reference signal δ_cmd. In contrast, the linear absolute value term penalizes even the slightest deviations from the reference and aids in precise tracking when envelope boundaries are not breached. Weight $R_{\mathrm{d}u}$ in (3.14b) penalizes rapid changes in control variables to ensure a smoother driving process.

To reduce the optimization algorithm's use of high steering angles, weight R_u penalizes wide input angles, while weight R_x penalizes higher sideslip angles. No penalties are imposed on other states; however, they can be introduced, for instance, by utilizing the driving envelope constraints.

Inequality constraints are augmented with slack variables s_i, s_eo, and s_eb to avoid infeasibility of the OCP, with relatively high penalties Q_i, Q_eo, and Q_eb [54] applied when entering the objective function.

Careful tuning is essential for the weighting matrices Q and R. The matrices in the Q-group necessitate notably high values to prevent constraint violations and ensure the smooth tracking of the commanded steering value without abrupt changes, all within the constraints, a consideration influenced by matrices in the R-group.

A binary diagonal matrix W is utilized to switch on obstacle constraints and minimize them within the objective. The baseline controller formulation used in this study only considers two obstacles on the road ($\eta = 2$), with each obstacle introducing new constraints for every subjected wheel and a new slack variable, which is minimized inside the objective function.

Constraints (3.14d)-(3.14g) are enforced for $k = 0, \ldots, N-1$. Constraints (3.14h)-(3.14k) are enforced for $k = 0, \ldots, N$. Constraint (3.14d) represents the discretized linear single-track dynamics from (3.5). Inequality (3.14e) presents slew protection for control variable and (3.14f) imposes physical constraints as the maximum possible steering angle.

Constraint (3.14h) is represented by a quadratic inequality with soft constraint, where softness is provided with a slack variable as:

$$(p_{\mathrm{x}ij,k} - p_{\mathrm{x}_{\eta_0}})^2 + (p_{\mathrm{y}ij,k} - p_{\mathrm{y}_{\eta_0}})^2 \geq W^{(\eta,\eta)}(r_\eta - s^{(\eta)}_{\mathrm{eo},k})^2 \tag{3.15}$$

where $(p_{\mathrm{x}_{\eta_0}}, p_{\mathrm{x}_{\eta_0}}) \in X_{0,\mathrm{obs}} \times Y_{0,\mathrm{obs}}$ are coordinates of the center of the particular obstacle, $r_\eta \in R_{\mathrm{obs}}$ is a radius of the particular obstacle. By setting $W^{(\eta,\eta)} = 0$, this constraint can be omitted. In the provided implementation, this inequality was applied to the front wheels only. This was done for two reasons: firstly, to reduce computational consumption, and secondly, to allow for greater steering angles under normal operating conditions of a front-steering car, where the sideslip angle β has a small value, resulting in the rear wheels traveling almost in the same position as the front wheels. Otherwise, the utilization of greater steering angles would be prevented due to the imprecise linear approximation of the vehicle dynamics, making the controller too conservative.

For the case of an undrivable obstacle, additional constraints are added to the OCP (3.14) to restrict the controller from allowing the car to go over the obstacle. One such constraint would be added for the position of the whole front axle so that the axle does not go over the detected obstacles. This additional constraint ensures a collision-free trajectory with undrivable obstacles. However, from the numerical optimization point of view, constraints for a set of points lying on the front axle are sufficient. To introduce such a restriction in the MPC, axle points are defined as:

$$p_{x_{\mathrm{axle}}} = p_{\mathrm{xfl}}\kappa + p_{\mathrm{xfr}}(1-\kappa), \tag{3.16}$$

$$p_{y_{\mathrm{axle}}} = p_{\mathrm{yfl}}\kappa + p_{\mathrm{yfr}}(1-\kappa) \tag{3.17}$$

where $\kappa \in (0, 1)$ is a predefined parameter for the optimization problem (for example, $\kappa = 0.5$ defines the position of the middle of the axle). Those positions can be constrained

in the same manner as the position of wheels in (3.15) as;

$$(p_{\mathrm{x}_{\mathrm{axle}},k} - p_{\mathrm{x}_{\eta_0}})^2 + (p_{\mathrm{y}_{\mathrm{axle}},k} - p_{\mathrm{y}_{\eta_0}})^2 \geq W^{(\eta,\eta)}(r_\eta - s^{(\eta)}_{\mathrm{eo},k})^2. \tag{3.18}$$

Constraints for the rear axle or other parts of a vehicle can be omitted because it is assumed that the rear axle (and the whole vehicle body) will travel almost in the same trajectories as the front axle. There is no need to use a high number of axle constraints. Mostly, a couple of the front axle points can be used. For instance, for the experiments provided in this chapter, only one middle point with $\kappa = 0.5$ was introduced in the problem.

The possible positions of wheels on the road, defined by parabolic boundaries, are defined by constraint (3.14j). This constraint is implemented as a set of two soft nonlinear inequality constraints:

$$p_{\mathrm{yl}ij,k} - a_{3\mathrm{l}} p^3_{\mathrm{xl}ij,k} - a_{2\mathrm{l}} p^2_{\mathrm{xl}ij,k} - a_{1\mathrm{l}} p_{\mathrm{xl}ij,k} \leq a_{0\mathrm{l}} - \sigma + s_{\mathrm{eb,l},ij,k} \tag{3.19}$$

for the left side of the road/rut and

$$p_{\mathrm{yl}ij,k} - a_{3\mathrm{l}} p^3_{\mathrm{xl}ij,k} - a_{2\mathrm{r}} p^2_{\mathrm{xl}ij,k} - a_{1\mathrm{r}} p_{\mathrm{xl}ij,k} \geq a_{0\mathrm{r}} + \sigma - s_{\mathrm{eb,r},ij,k} \tag{3.20}$$

for the right side of the road/rut. Inequalities (3.19) and (3.20) contain parameters a_n ($n \in [0, 1, 2, 3]$), which are coefficients of approximations of the road/rut borders, and parameter σ, which serves as a padding distance from the border. Theoretically, these constraints should be applied to all wheels. However, it is sufficient to constrain the front wheels only for the same reasons as for obstacle constraints.

By applying constraints (3.14h)-(3.14k) on the final state, the persistent feasibility property is ensured. The inputs from the previous step u_{N-1} are used to calculate x_{N+1} by setting the decision variable for the last step equal to them ($u_N = u_{N+1}$), as shown in (3.14d). The non-negative slack variables are defined in (3.14g), (3.14i), and (3.14k). The MPC problem is initialized with the initial condition in (3.14l), where the state measurement is denoted by $\beta(t)$ and $r(t)$, and the control action in the previous sampling instance is represented by $u(t - T_\mathrm{s})$.

The OCP (3.14) is calculated at frequency 20 Hz, which fully covers the single-track dynamics (at 3-5 Hz [77]) at that frequency. It is shown in the next section that the OCP can mostly be solved within 0.05 s.

The idea of considering a preview window in front of the vehicle defines the proposed algorithm, and the size of the window is dictated by the camera properties. An observable distance of 4-20 m in front of the vehicle was assumed in the provided implementation.

However, the time taken by the vehicle to pass that distance is significantly affected by its speed. For this implementation, a prediction horizon of $N = 10$ and a sampling time of $T_s = 0.05$ were used, resulting in a prediction time of 0.5 s. This means that the controller will only be able to look ahead for 4 m in front of the car for a velocity of around $30\,\mathrm{km\,h^{-1}}$ and 10 m when it travels at $70\,\mathrm{km\,h^{-1}}$.

The maximum possible viewable obstacle size is also determined by the velocity and the sampling time. For example, when the vehicle travels at $30\,\mathrm{km\,h^{-1}}$, and the sampling time is 0.05 s, obstacles smaller than 42 cm in diameter would not be visible to the controller. However, at $70\,\mathrm{km\,h^{-1}}$, the controller would be able to "see" only significantly larger objects, specifically 97 cm in diameter. Therefore, the proposed controller would require different settings for the number of prediction steps and sampling periods for different velocities in real-world applications.

3.6 Experimental Validation

Vehicle dynamics simulations across diverse scenarios were performed using IPG CarMaker software [55], integrated with MATLAB/Simulink. The controller outlined in the previous section was incorporated into Simulink through the CasADi framework [86], and the OCP was solved, yielding optimal control input via the IPOPT solver [87] and MA27 internal linear solver [88]. A range of road scenarios was examined to validate the controller's potential by subjecting the vehicle to challenges that deviate from a secure environmental envelope.

Various road-keeping scenarios, drivable obstacle avoidance, and tests for undrivable obstacle avoidance were executed at different speeds, affirming the controller's efficiency across dynamic changes. Results and discussions pertaining to the tests are detailed in dedicated subsections. Additionally, experiment time requirements were explored to assess the algorithm's potential for real-time operation on NVIDIA Jetson Xavier, as presented in the concluding subsection.

To provide a comparison with a baseline controller, which constraints the safe envelope utilizing the middle-line of a lane and regular formulation of obstacles, adjustments to the drivable road definition (3.19) and (3.20) were made to align with [43]. Constraints for the middle of the front axle were defined, ensuring it stays between the maximum and minimum possible distances from the centerline, described as a cubic parabolic function. Unlike other solutions, the presented controller allows for the independent definition of boundaries for the left and right drivable road boundaries. However, the general concept remains consistent. The baseline controller integrated a traditional obstacle avoidance algorithm, treating all obstacles as undrivable. Constraints for the middle of the front

axle were set to avoid obstacles similarly to (3.18), but with an increased obstacle radius by at least half of the axle width distance w. Adjustments to the weighting factor $Q_{\text{eo}} = 10^5$ and prediction horizon $N = 20$ were made to enhance the baseline controller's ability to navigate tests without collisions.

For reproducibility, the "DemoCar" was selected as the test vehicle for the same reasons as for driving envelope tests. Car parameters are detailed in Table 2.4. The entire project, encompassing control strategy implementation in MATLAB/Simulink, is accessible at [57]. The test vehicle is operated by the standard driver from CarMaker. Videos of all driving tests are available on the YouTube channel [58] for enhanced clarity.

3.6.1 Drivable Road Keeping

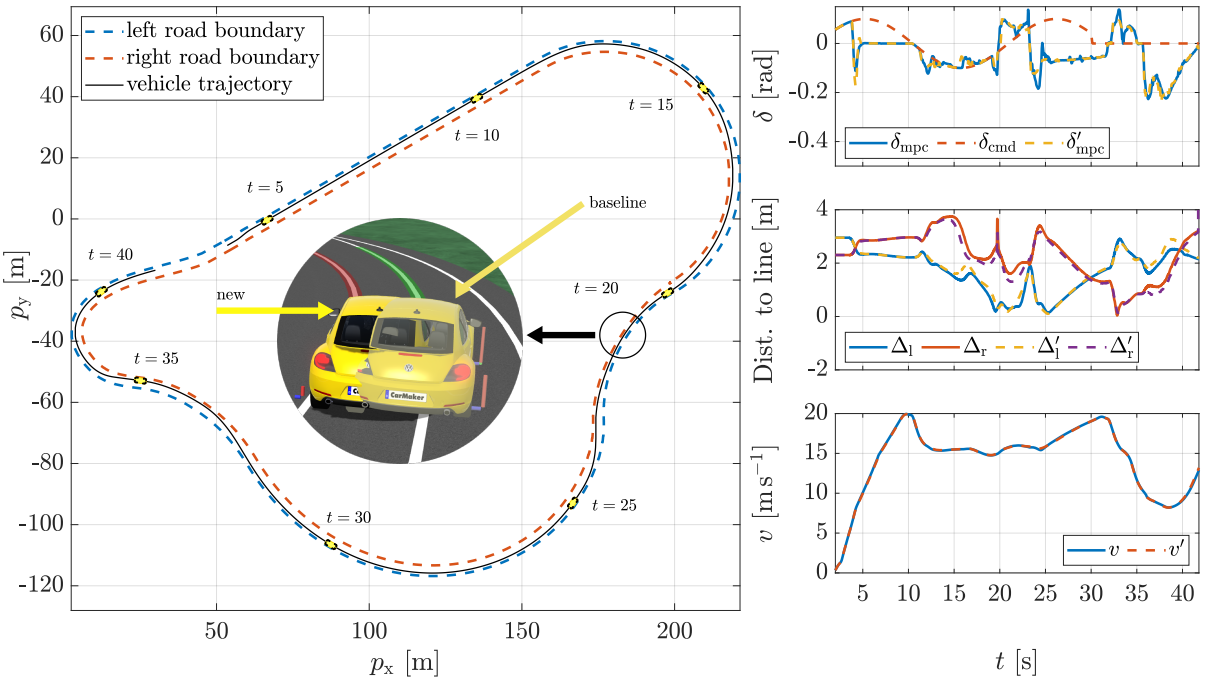

Figure 3.6: Comparison of dynamic road protection at varying speeds on a test track, contrasting with the baseline control denoted by primes. The driver applied sinusoidal input and released the steering wheel. The vehicle navigates within road boundaries, allowing driver control on the track.

The drivable road-keeping functionality underwent testing in two driving scenarios. In the initial scenario, a test track was devised, encompassing a straight line, a circle arc, two distinct clothoids, and a polynomial point-to-point connection. The latter element is commonly encountered on challenging terrains or racing tracks, necessitating a reduction in speed before executing cornering actions. Figure 3.6 presents a comparison between the proposed controller, denoted as "new," and the baseline controller. The results indicate that both controllers effectively maintain lane-keeping in these challenging

scenarios. Notably, all line borders were parallel, except for one intentionally designed segment with an unparallel line. In this instance, the baseline controller, guided by the centerline, deviated out of the right border, whereas the presented controller successfully provided road-keeping even on narrow, drivable roads.

Table 3.3: Mean RMS Error of a Polynomial Approximation during Each Track Segment in Meters

Track Part	1st degree	2nd	3rd	4th	5th
Straight	1.5e−9	1.1e−9	7.4e−10	4.3e−10	2.2e−10
180 deg turn	0.1212	0.0033	0.0012	6.1e−4	4.2e−4
Clothoid 1	0.0506	0.0035	0.0012	6.4e−4	3.8e−4
Clothoid 2	0.0665	0.0032	0.0012	6.3e−4	3.9e−4
Polynomial point-to-point	0.1161	0.0194	0.0058	0.0024	0.0013

This test also aimed to assess the precision of approximating lines with cubic parabolas. Table 3.3 demonstrates that the 3rd-order polynomial offers a precise approximation compared to lower orders. Simultaneously, maintaining precision within one centimeter highlights the unnecessary use of higher degrees, as it could increase the computational time for the OCP without an increase in control precision.

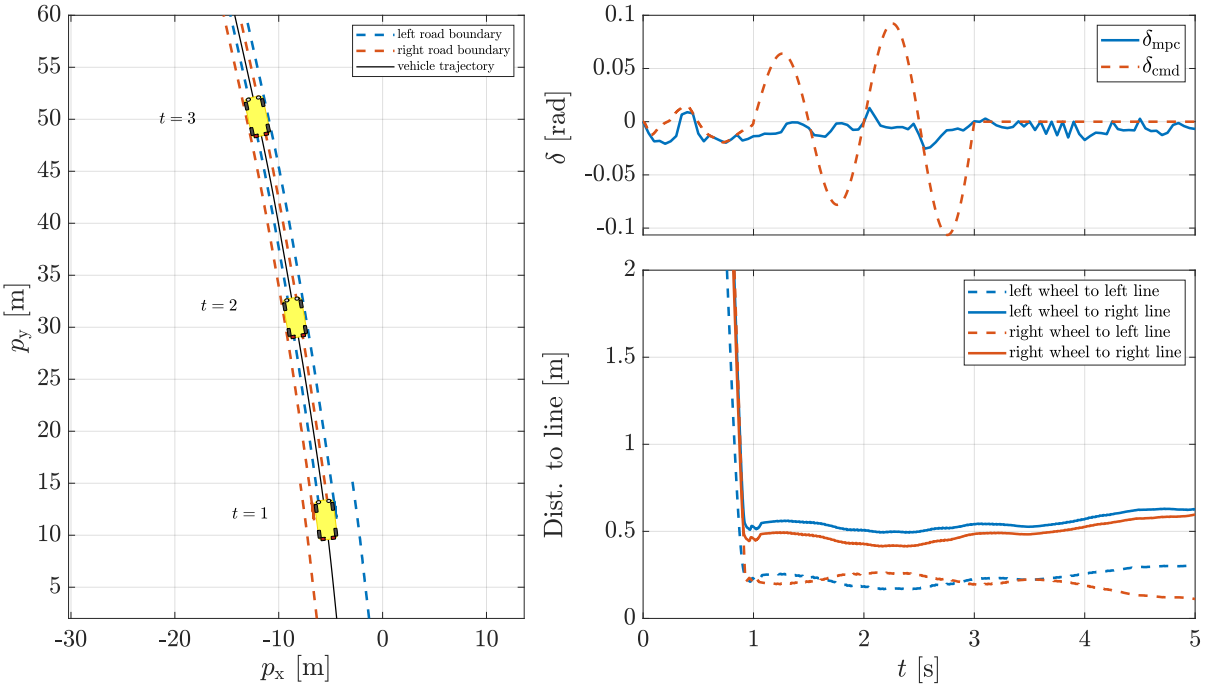

Figure 3.7: Drivable road protection at 70 km h^{-1}, simulating road ruts. The controller detects ruts at $t = 0$ and adjusts the steering to align with the tracks. The protection system allows steering wheel adjustments until the vehicle stays within the predefined constraints.

The second experiment highlights a functionality unattainable for standard lane-keeping systems: defining the drivable road as a pair of tracks simulating scenarios such

as road ruts or rural road driving. In the experiment depicted in Fig. 3.7, the system detects ruts on the road and adjusts the steering action from the driver to guide the wheels within the ruts (assuming an asphalt surface with a higher friction and surrounded by snow). The system effectively maintains this drivable road within the experiment while the driver makes small deviations of the steering wheel to the left and right in a sine-like manner (as an input disturbance to test the functionality) and then returns the steering wheel to the neutral position. The controller permits these actions until the wheels reach the predefined boundaries.

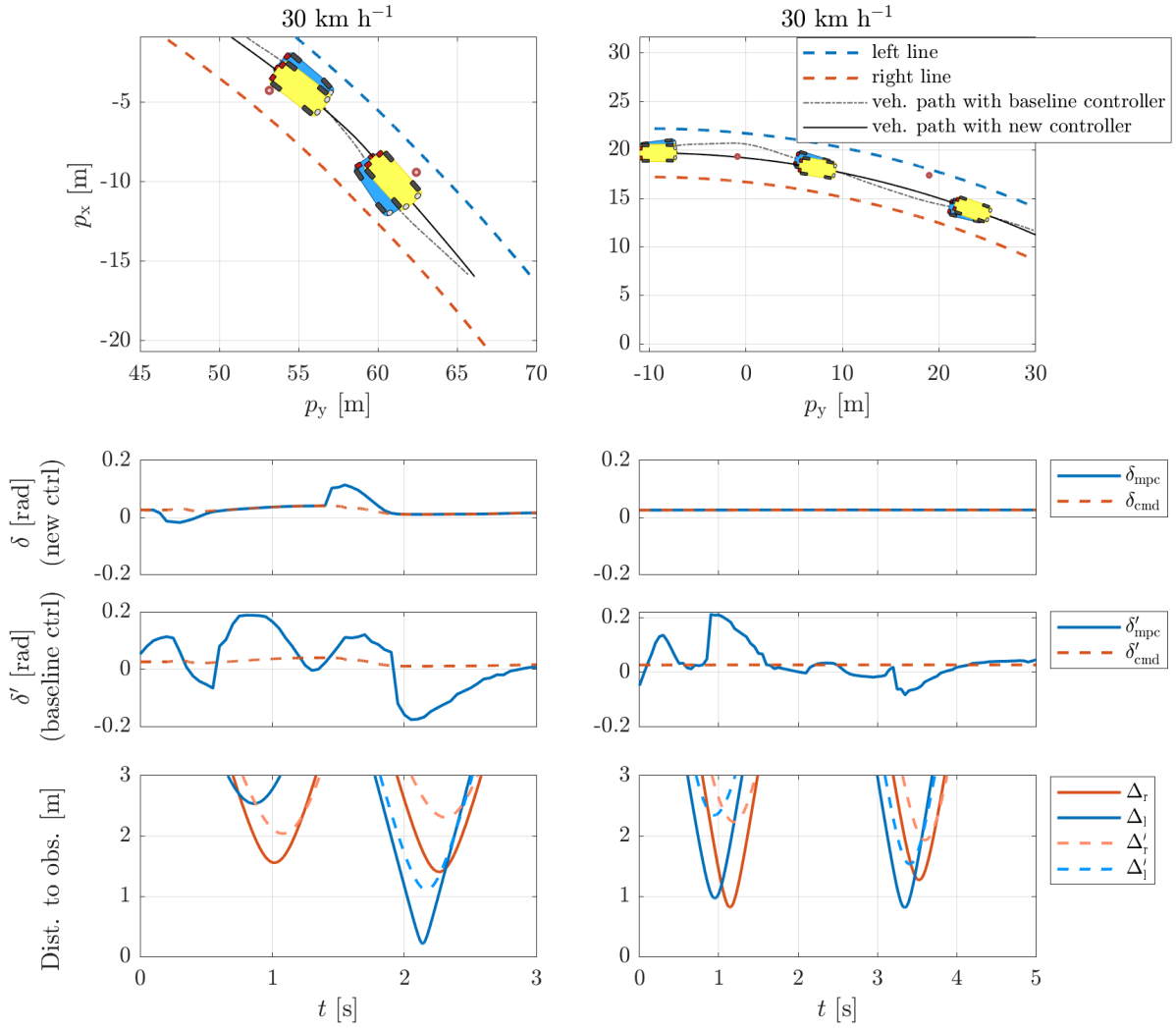

Figure 3.8: Comparison of obstacle avoidance between the proposed and baseline controllers (primed) at 30 km h^{-1}. Tests involve two obstacles and settings. Rows two and three show commanded and actual steering positions for both solutions. The last row displays the distances of the front wheels to obstacles.

3.6.2 Drivable Obstacle Avoidance

The second test aimed at validating the controller's ability to navigate drivable obstacles in various configurations and speeds (30 and 70 km h^{-1}), comparing it with a traditional obstacle avoidance formulation. The results are presented in Fig. 3.8 and Fig. 3.8, where the last row illustrates distances from both front wheels to the center of the obstacles. These obstacles were modeled with a radius of $r = 0.5$ m, comprising a 0.3 m actual obstacle radius and an additional 0.2 m. This adjustment is necessary because a wheel is modeled as a single point, requiring an increased safety distance to prevent wheel rim contact with obstacles. For the baseline controller, the modeled radius was set to $r = 2$ m.

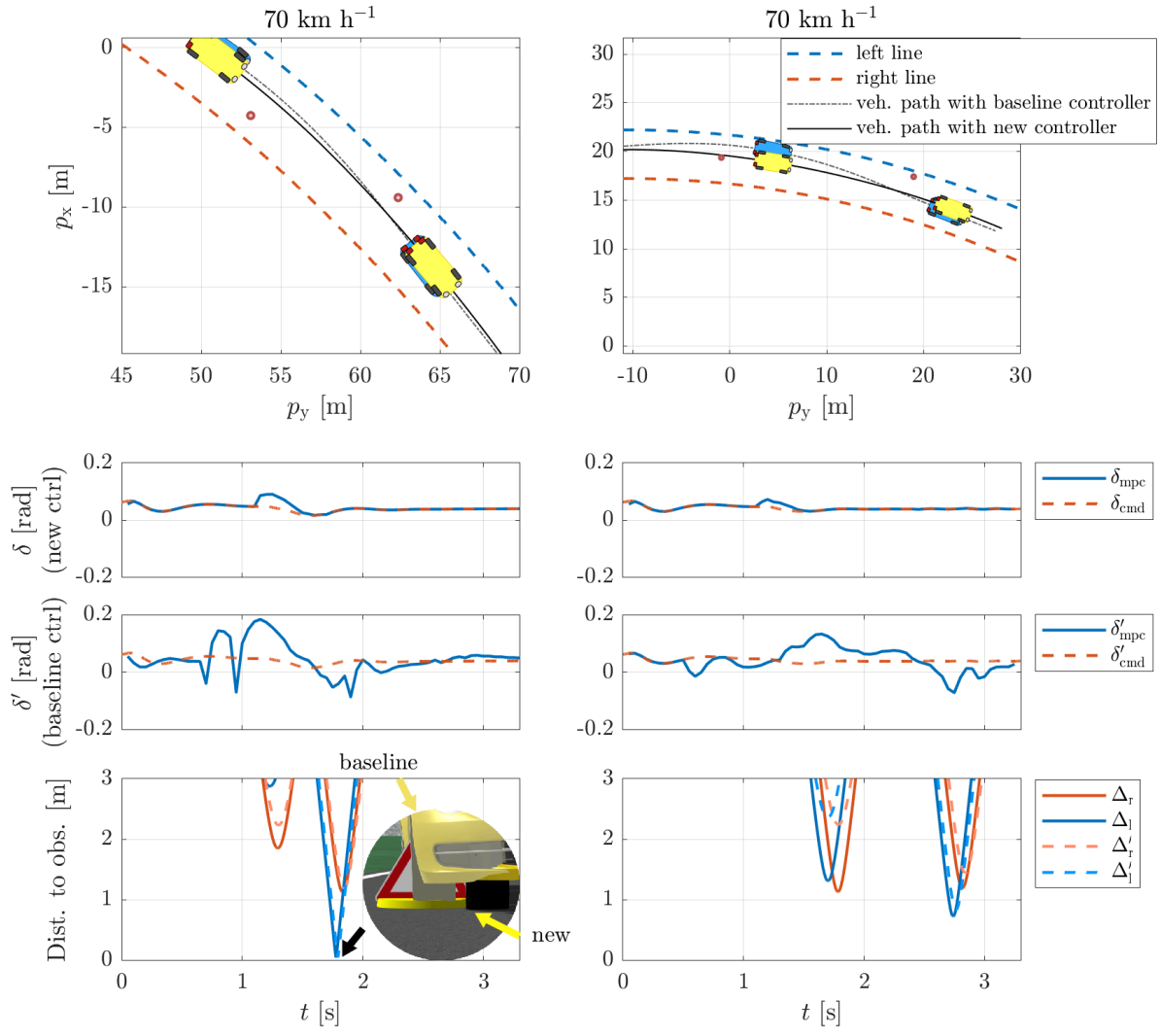

Figure 3.9: Comparison of obstacle avoidance between the proposed and baseline controllers (primed) at 70 km h^{-1}. Tests involve two obstacles and settings. Rows two and three show commanded and actual steering positions for both solutions. The last row displays the distances of the front wheels to obstacles.

In the initial section of the road (first columns in Fig. 3.8 and Fig. 3.8), with one obstacle on the right and the other on the left, both controllers swiftly executed steering actions

to avoid obstacles at both slow and higher speeds. The proposed controller demonstrated smaller control alterations due to a smaller slack penalization Q_{oe} (this adjustment was made for the baseline controller because, in the subsequent section of the test, the baseline controller struggled with a smaller weight). Additionally, the baseline controller faced difficulty avoiding the second obstacle at a higher speed and passed over it by the right wheel, as shown in Fig. 3.8. Simultaneously, the proposed controller successfully avoided the obstacle.

In the designed section (second columns in Fig. 3.8 and Fig. 3.8), where the first obstacle was positioned between the wheels, allowing the vehicle to pass with minimal steering wheel adjustment, the baseline controller, implemented in the standard way, required the entire vehicle to avoid the obstacle.

Comparing both controllers, one can acknowledge that the proposed definition offers more flexibility for the controller to operate a car safely and with smaller steering wheel adjustments on a significantly shorter prediction horizon.

3.6.3 Undrivable Obstacle Avoidance

This test scenario validates the controller's ability to navigate undrivable obstacles. In this arrangement, a blue car in Fig. 3.10 serves as such an obstacle. The parked car is enclosed by two circles with a radius of 2 m, represented as constraints (3.14i) in the OCP. With the introduction of an undrivable obstacle, the OCP (3.14) was expanded with additional axle constraints (3.18). The algorithm anticipated a future violation of the obstacle constraints, assisting the driver in avoiding a collision with another vehicle and maintaining the predefined drivable path.

Due to the soft constraints in the OCP, the controlled vehicle deviated from the circle obstacle constraint but successfully avoided colliding with the blue car. Consequently, implementing this approach requires reasonable buffering around objects on the road within the circle-bound boxes or increasing the weighting factor, especially for undrivable obstacles, as demonstrated in the next test scenario.

3.6.4 Obstacle Prioritization

The mathematical formulation of the obstacle avoidance problem provides an advantage by allowing the prioritization of obstacles through the definition of weighting factors associated with obstacle classes. These factors assign varying degrees of importance and danger to different objects. For instance, driving over an icy surface may pose a greater risk due to poor traction compared to asphalt. Simultaneously, potholes may be considered more hazardous than ice patches. Undrivable obstacles, in contrast, present a higher

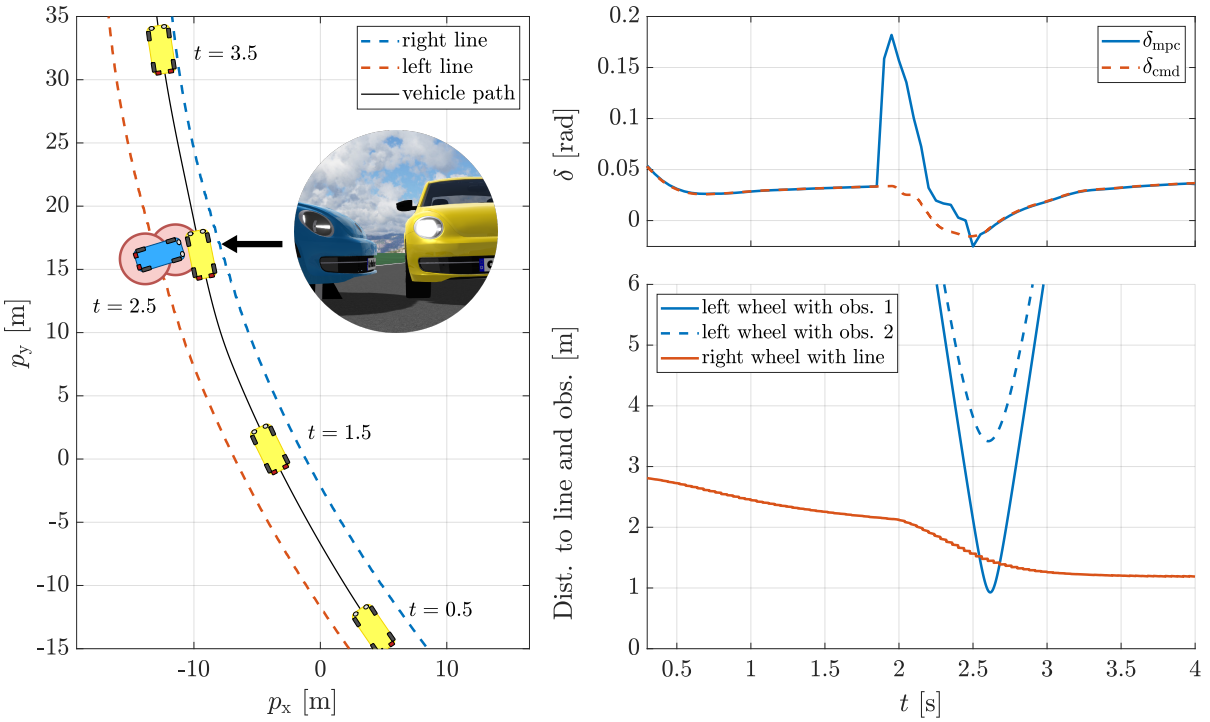

Figure 3.10: Undrivable obstacle avoidance at a speed of 60 km h^{-1}. Red circles indicate obstacles in the MPC formulation. Distances to objects are computed relative to their centers.

level of danger than any drivable obstacle, as they have the potential to cause damage to the vehicle.

In a specific test scenario, two obstacles were introduced on the road: a road irregularity to the right (yellow spot) and a cardboard box (treated as a drivable obstacle for this scenario to avoid additional constraints of undrivable obstacles) that fell from a cargo vehicle. Both obstacles were modeled with a radius of $r = 1.5\,\text{m}$. Recognizing that the road irregularity is less harmful, it was assigned a lower priority with a corresponding lower weighting factor, Q_{eo}, set to 10^3, compared to 10^6 for the box. To illustrate, the same experiment was also conducted without the cardboard box, demonstrating that, in this scenario, the vehicle would successfully avoid the road irregularity.

The simulation experiment results, presented in Fig. 3.11, confirm the hypothesis that obstacle prioritization is achievable. When the controller faces difficulty finding a clear path, it prioritizes navigating over the less significant obstacle. This prioritization concept can also be applied to drivable road constraints. For example, assigning a higher weight to the main lane boundary than to road ruts or prioritizing physical boundaries like concrete borders over mere lines enhances the adaptability of the controller in navigating complex road scenarios.

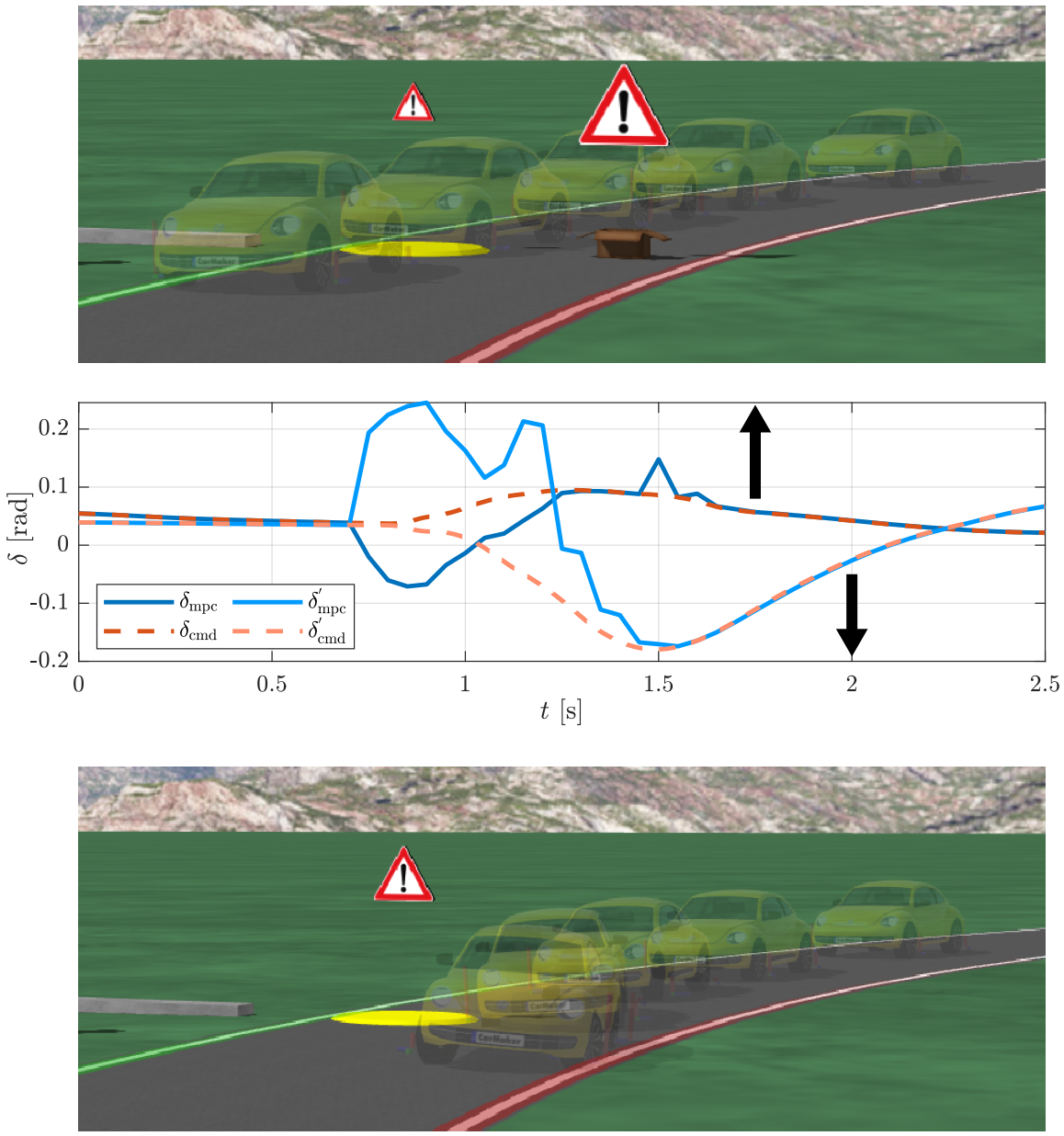

Figure 3.11: Test on obstacle prioritization at $50\,\mathrm{km\,h^{-1}}$. Prime notations illustrate the controller's input and output signals for the second scenario, featuring only the presence of a road irregularity.

3.6.5 Computational Time Demands of the Experiments

The evaluation of execution time for each iteration in the previously outlined test scenarios aimed to ascertain the real-time feasibility of the proposed algorithm on embedded hardware. These measurements offer insights into both the algorithm's problem definition robustness and the solver's capability to handle numerical challenges, particularly in complex scenarios. The computationally intensive segments of the algorithm, including OCP implementation and solver execution, were coded in C++. The entire implementation is accessible on the open GitHub [57]. These assessments utilized closed-loop precomputed data from the aforementioned simulations in Simulink. The code ran on the NVIDIA Jetson AGX Xavier, a hardware choice often employed in autonomous driving control frameworks for its graphic modules dedicated to image processing. However, this algorithm utilizes only the CPU.

Throughout the evaluations, the entire algorithm ran in a single thread on a CPU with a maximum frequency of 2.2 GHz. Elapsed time was recorded for each iteration, and the results are visually presented in Fig. 3.12, with statistical data available in Table 3.4. The experiment naming convention includes A for drivable road keeping, A1 for lane protection, and A2 for rut-road; B for drivable obstacle avoidance, with B1 and B2 corresponding to specific columns in Fig. 3.8 and B3 and B4 corresponding to specific columns in Fig. 3.9; C for undrivable obstacle avoidance, and D for obstacle prioritization, with D1 indicating scenarios with both obstacles presented and D2 for situations with only one obstacle.

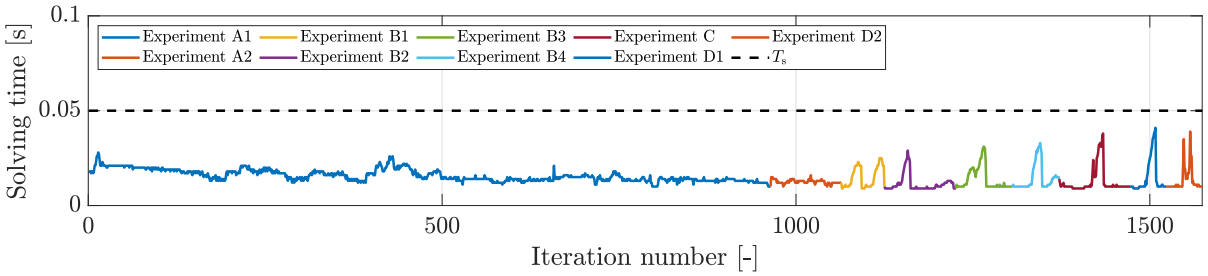

Figure 3.12: Individual step solution times of MPC for environmental envelope protection across corresponding experiments.

An initial observation reveals that all iterations required less time than the specified sampling period T_s, set at 0.05 s. This emphasizes the well-defined nature of the OCP, suggesting that the solver swiftly converges to an optimal solution without extended computational efforts. Notably, both the mean and median time values are even smaller, demonstrating the solver's rapid convergence when dealing with unviolated envelope boundaries.

Further investigation into obstacle avoidance exposes spikes in the time consumption

Table 3.4: Statistics on Time Consumption

Experiment	Mean [s]	Median [s]	Max [s]
A1	0.0158	0.0150	0.0280
A2	0.0125	0.0120	0.0160
B1	0.0150	0.0110	0.0250
B2	0.0114	0.0100	0.0290
B3	0.0139	0.0100	0.0310
B4	0.0144	0.0110	0.0330
C	0.0125	0.0100	0.0380
D1	0.0149	0.0100	0.0410
D2	0.0133	0.0100	0.0390

plot, indicating slower convergence of the solver for used obstacle definitions. However, these spikes still occurred within the sampling time and solver call duration (which were the same).

These results affirm the robust performance of the chosen OCP definition and suggest the potential adoption of such a control law for real-world scenarios.

3.7 Discussion

This chapter presents a novel approach to delineating safe space boundaries for a vehicle, considering the perspective of the wheels. This approach holds the potential to navigate small road obstacles and areas with reduced friction or high roughness. Its mathematical adaptability allows for application in standard lane-keeping and obstacle-avoidance scenarios. Building on the environmental envelope methodology, it is possible to introduce a new category of safety systems that can act as middleware between traditional path planning and tracking systems (or human drivers) and lower-level control systems. This ensures maneuver safety for both vehicle and wheel security. During this work, a comparative analysis of this approach against traditional systems that define lane boundaries based on the middle lane and treat each obstacle as requiring avoidance by the entire vehicle was conducted.

The resulting safety systems have undergone successful testing in various driving scenarios and operate in real-time on embedded hardware. However, a limitation of this approach serves as a potential avenue for future work - the algorithm presented in this chapter assumes each obstacle is static. Therefore, addressing the incorporation of moving obstacles into the optimization problem emerges as a primary target for future research in this field.

Chapter 4

Conclusion

In conclusion, the development of future driver assistance systems will go beyond vehicle stabilization and encompass considerations of environmental and stability threats to vehicle safety. With advancements in sensing and actuation capabilities, automated systems can take on more responsibility in ensuring vehicle safety, alleviating human drivers from the pressure of achieving flawless control.

This dissertation introduces a straightforward and effective approach to defining safety and stability criteria for vehicles. The discussed paradigm shift moves away from a vehicle-centric perspective to a wheel-level perspective (by projection of the wheel states to the vehicle level) in defining stability and safety criteria. The driving envelope specifies desired vehicle maneuvers that maintain both vehicle and wheel stability, allowing for the tuning of vehicle behavior based on wheel stability regions. Simultaneously, the environmental envelope, also introduced in this work, defines a safety space based on vehicle dynamics and vehicle perception. This safety space considers drivable and undrivable obstacles, enabling prioritization between them.

The controllers presented in this research, known as envelope protectors, employ a pathless model predictive control approach that enables fast, real-time optimization on embedded hardware. Extensive experiments conducted on a high-fidelity vehicle dynamics simulator demonstrate that driving envelope protection combines the functionalities of commonly used systems, such as anti-lock braking, traction control, and electronic stability programs, into a single optimization problem. This approach could serve as an additional safety layer for other advanced driver assistance systems, enhancing their functional safety. Additionally, environmental envelope protection provides the functionalities of lane-keeping and collision-avoidance systems. It can be utilized as a standalone ADAS or integrated into complex ADAS systems to enhance overall safety.

In summary, the proposed control framework presents a compelling alternative to existing stability control systems and the prevalent path tracking and following paradigm

employed in automated vehicle control. It offers a comprehensive solution that addresses safety, stability, and obstacle prioritization, contributing to the advancement of autonomous and human-governed driving technologies. With the integration of envelope control, future driver assistance systems can provide enhanced safety and control in a variety of driving scenarios.

4.1 Future Work

The research project can make an impact and contribute to the field by inspiring innovative and thought-provoking research directions. The envelope control framework, introduced in this dissertation, may serve as the foundation for several new research projects addressing various vehicle control issues.

4.1.1 Autonomous and Semi-autonomous Vehicles

The primary focus of the proposed control framework's design revolves around its collaboration with a human driver or its mathematical equivalent. Nonetheless, this framework holds potential for application in the control of autonomous or semi-autonomous vehicles. By effectively integrating both envelopes (along with their protective controllers) into a control scheme for driverless vehicle operation, they can act as robustness providers at a lower level for the path and trajectory planners and trackers at the upper level. Developing a fully autonomous vehicle is a significant endeavor, but these adapted envelope controllers are well-suited to serve as coordinators for steering, braking, and throttle commands, enabling the accomplishment of higher-level objectives in a fully autonomous vehicle. This transformation simplifies the control problem by converting the complex task of generating safe and feasible trajectories in the environment into higher-level objectives, such as the desired path or desired longitudinal and lateral forces that can be transformed into the actuation of the control elements while simultaneously ensuring vehicle safety.

4.1.2 Application for Other Wheeled Vehicles

The concept behind these envelopes can be applied beyond just passenger cars. In theory, any wheeled vehicle experiences the same physics related to wheel slipping and positioning during motion. This means that any mobile robot propelled by wheels can benefit from the approaches discussed. Additionally, other motorized vehicles like tracks, buses, and motorbikes can also adopt the same theory of envelope control, albeit with suitable modifications. The existing controller can be readily enhanced, such as by incorporating

rollover prevention measures, to accommodate the operation of taller vehicles like SUVs, buses, and tracks.

4.1.3 Ethics of Obstacle Prioritization

The proposed controller employed for protecting the environmental envelope relies on multiple objectives to guarantee secure operation. Through experimental observations, it has been demonstrated that these objectives occasionally clash, necessitating the establishment of a hierarchical structure with tiered costs. This structure serves as an objective hierarchy, enabling the controller to navigate such situations effectively. In essence, the envelope controller incorporates an ethical framework, and ongoing research seeks to investigate the potential impact on the design of these control systems when evaluated from different established ethical perspectives. This interdisciplinary endeavor aims to bridge the gap between the realms of philosophy and engineering.

4.1.4 Application on V2X

V2X technology allows vehicles to gather additional information about their surroundings. This includes data from the environment and other vehicles, providing valuable insights into road conditions, friction, movement, and future paths. This information can be used to enhance control algorithms by imposing new constraints. For instance, the environmental envelope protection system can utilize the predicted movement of undrivable obstacles and the position of drivable obstacles on the road from far away, while the driving envelope protection system can assess friction ahead of the vehicle and adjust tuning parameters to improve performance.

4.2 Outlook

By leveraging recent advancements in vehicle actuation and sensing, the proposed envelope control framework demonstrates significant potential in guaranteeing vehicle stability and safety. This research emphasizes the capabilities and possibilities of next-generation driver assistance systems, which aim to protect drivers from unwanted vehicle movements and environmental hazards. These systems will assume a more active role in driving, alleviating the current burden on drivers and enhancing vehicle safety. By delegating some of the responsibilities to an envelope controller like the one presented, it becomes possible to combine the precision and attentiveness of machines with the critical thinking skills of humans or to reduce the complexity of the problem for the higher-level automation system. These advanced driver assistance systems will revolutionize the driving experi-

ence, improving both the nature and safety of driving while preserving the mobility and flexibility that automobiles offer to drivers.

Bibliography

[1] Center for Sustainable Systems, University of Michigan, "Personal transportation factsheet, Pub. No. CSS01-07," Tech. Rep., 2022.

[2] A. Tilford and M. Megna, "Car ownership statistics 2023," Tech. Rep., 2023. [Online]. Available: `https://www.forbes.com/advisor/car-insurance/car-ownership-statistics/`.

[3] P. Hu, R. R. Schmitt, R. Robinson, *et al.*, "Transportation statistics annual report 2022," Tech. Rep., 2022.

[4] Airbus S.A.S, "A statistical analysis of commercial aviation accidents 1958-2020," Tech. Rep., 2021.

[5] A. G. Ulsoy, H. Peng, and M. Çakmakci, *Automotive control systems*. Cambridge University Press, 2012.

[6] C. J. Kahane and J. N. Dang, "The long-term effect of ABS in passenger cars and LTVs," Tech. Rep., 2009.

[7] J. N. Dang, "Statistical analysis of the effectiveness of electronic stability control (ESC) systems-final report," Tech. Rep., 2007.

[8] R. Rajamani, *Vehicle dynamics and control*. Springer Science & Business Media, 2011.

[9] Apex.AI, Inc. "Apex.ai webpage." (2024), [Online]. Available: `https://www.apex.ai/`.

[10] R. C. Nelson *et al.*, *Flight stability and automatic control*. WCB/McGraw Hill New York, 1998, vol. 2.

[11] D. Efremov, "Unstable ground vehicles and artificial stability systems," M.S. thesis, Czech Technical University in Prague, 2018.

[12] H. Walgemoed, "Flight envelope," *Introduction to Flight Test Engineering*, 1995.

[13] T. Lombaerts, G. Looye, J. Ellerbroek, and M. R. y. Martin, "Design and piloted simulator evaluation of adaptive safe flight envelope protection algorithm," *Journal of Guidance, Control, and Dynamics*, vol. 40, no. 8, pp. 1902–1924, 2017.

[14] "Road vehicles – functional safety," International Organization for Standardization, Geneva, CH, Standard, Dec. 2018.

[15] "Taxonomy and definitions for terms related to driving automation systems for on-road motor vehicles," Society of Automotive Engineers, Warrendale, Pennsylvania, USA, Standard, Apr. 2021.

[16] Audi Australia. "Audi AI traffic jam pilot." (2024), [Online]. Available: `https://magazine.audi.com.au/article/audi-ai-traffic-jam-pilot`.

[17] Amazon Web Services, Inc. "Amazon Robotics uses Amazon SageMaker and AWS Inferentia to enable ML inferencing at scale." (2024), [Online]. Available: `https://aws.amazon.com/solutions/case-studies/amazon-robotics-case-study/`.

[18] Motional, Inc. "Motional website." (2024), [Online]. Available: `https://motional.com/technology`.

[19] C. Hong, G. Xun, H. Yun-Feng, L. Qi-Fang, G. Bing-Zhao, and G. Hong-Yan, "Automotive control: The state of the art and perspective," *Acta Automatica Sinica*, vol. 39, no. 4, pp. 322–346, 2013.

[20] V. Ivanov, B. Shyrokau, D. Savitski, *et al.*, "Design and testing of ABS for electric vehicles with individually controlled on-board motor drives," *SAE International Journal of Passenger Cars-Mechanical Systems*, vol. 7, no. 2, pp. 902–913, 2014.

[21] F. Pretagostini, L. Ferranti, G. Berardo, V. Ivanov, and B. Shyrokau, "Survey on wheel slip control design strategies, evaluation and application to antilock braking systems," *IEEE Access*, vol. 8, pp. 10 951–10 970, 2020.

[22] V. Ivanov, D. Savitski, and B. Shyrokau, "A survey of traction control and antilock braking systems of full electric vehicles with individually controlled electric motors," *IEEE Transactions on Vehicular Technology*, vol. 64, no. 9, pp. 3878–3896, 2014.

[23] K. Koibuchi, M. Yamamoto, Y. Fukada, and S. Inagaki, "Vehicle stability control in limit cornering by active brake," SAE technical paper, Tech. Rep., 1996.

[24] S. Zheng, H. Tang, Z. Han, and Y. Zhang, "Controller design for vehicle stability enhancement," *Control Engineering Practice*, vol. 14, no. 12, pp. 1413–1421, 2006.

[25] C. Keatmanee, S. Jakborvornphan, C. Potiwanna, W. San-Uml, and M. N. Dailey, "Vision-based lane keeping-a survey," in *2018 International Conference on Embedded Systems and Intelligent Technology & International Conference on Information and Communication Technology for Embedded Systems (ICESIT-ICICTES)*, IEEE, 2018, pp. 1–6.

[26] R. Utriainen, M. Pöllänen, and H. Liimatainen, "The safety potential of lane keeping assistance and possible actions to improve the potential," *IEEE Transactions on Intelligent Vehicles*, vol. 5, no. 4, pp. 556–564, 2020.

[27] Volvo Car Corporation. "Pilot assist and lane keeping aid." (2024), [Online]. Available: `https://www.volvocars.com/uk/support/topics/article/3395a91b40bddd9ac0a801511916dab3`.

[28] J. N. Yasin, S. A. Mohamed, M.-H. Haghbayan, J. Heikkonen, H. Tenhunen, and J. Plosila, "Unmanned aerial vehicles (UAVS): Collision avoidance systems and approaches," *IEEE Access*, vol. 8, pp. 105 139–105 155, 2020.

[29] D. Soudbakhsh and A. Eskandarian, "Steering control collision avoidance system and verification through subject study," *IET Intelligent Transport Systems*, vol. 9, no. 10, pp. 907–915, 2015.

[30] B. Paden, M. Čáp, S. Z. Yong, D. Yershov, and E. Frazzoli, "A survey of motion planning and control techniques for self-driving urban vehicles," *IEEE Transactions on Intelligent Vehicles*, vol. 1, no. 1, pp. 33–55, 2016.

[31] Y. Wang, Z. Liu, Z. Zuo, Z. Li, L. Wang, and X. Luo, "Trajectory planning and safety assessment of autonomous vehicles based on motion prediction and model predictive control," *IEEE Transactions on Vehicular Technology*, vol. 68, no. 9, pp. 8546–8556, 2019.

[32] T. Wongpiromsarn, K. Slutsky, E. Frazzoli, and U. Topcu, "Minimum-violation planning for autonomous systems: Theoretical and practical considerations," in *2021 American Control Conference (ACC)*, IEEE, 2021, pp. 4866–4872.

[33] D. Vosahlik, P. Turnovec, J. Pekar, and T. Hanis, "Vehicle trajectory planning: Minimum violation planning and model predictive control comparison," in *2022 IEEE Intelligent Vehicles Symposium (IV)*, IEEE, 2022, pp. 145–150.

[34] C. G. Bobier-Tiu, S. M. Koehler, M. Brown, and M. Ahumada, "A unified MPC envelope control formulation for toyota guardian and chauffeur," *IFAC-PapersOnLine*, vol. 55, no. 16, pp. 19–24, 2022.

[35] S. Inagaki, I. Kushiro, and M. Yamamoto, "Analysis on vehicle stability in critical cornering using phase-plane method," *JSAE Review*, vol. 2, no. 16, p. 216, 1995.

[36] C. E. Beal, "Applications of model predictive control to vehicle dynamics for active safety and stability," Ph.D. dissertation, 2011.

[37] C. E. Beal and J. C. Gerdes, "Model predictive control for vehicle stabilization at the limits of handling," *IEEE Transactions on Control Systems Technology*, vol. 21, no. 4, pp. 1258–1269, 2012.

[38] M. Ataei, A. Khajepour, and S. Jeon, "Model predictive control for integrated lateral stability, traction/braking control, and rollover prevention of electric vehicles," *Vehicle System Dynamics*, vol. 58, no. 1, pp. 49–73, 2020.

[39] S. Thrun, M. Montemerlo, H. Dahlkamp, *et al.*, "Stanley: The robot that won the DARPA Grand Challenge," *Journal of Field Robotics*, vol. 23, no. 9, pp. 661–692, 2006.

[40] F. Von Hundelshausen, M. Himmelsbach, F. Hecker, A. Mueller, and H.-J. Wuensche, "Driving with tentacles: Integral structures for sensing and motion," *Journal of Field Robotics*, vol. 25, no. 9, pp. 640–673, 2008.

[41] A. Gray, Y. Gao, T. Lin, J. K. Hedrick, H. E. Tseng, and F. Borrelli, "Predictive control for agile semi-autonomous ground vehicles using motion primitives," in *2012 American Control Conference (ACC)*, IEEE, 2012, pp. 4239–4244.

[42] S. J. Anderson, S. B. Karumanchi, and K. Iagnemma, "Constraint-based planning and control for safe, semi-autonomous operation of vehicles," in *2012 IEEE Intelligent Vehicles Symposium*, IEEE, 2012, pp. 383–388.

[43] S. M. Erlien, "Shared vehicle control using safe driving envelopes for obstacle avoidance and stability," Ph.D. dissertation, 2015.

[44] D. Efremov, T. Haniš, and M. Klaučo, "Vehicle and wheels stability defined using driving envelope protection algorithm," *IEEE Transactions on Intelligent Transportation Systems*, pp. 1–13, 2024.

[45] Y. Judy Hsu, "Estimation and control of lateral tire forces using steering torque," Ph.D. dissertation, 2009.

[46] H. Pacejka, *Tire and vehicle dynamics*. Elsevier, 2005.

[47] J. Svendenius, "Tire modeling and friction estimation," Ph.D. dissertation, Lund University, 2007.

[48] D. Efremov, M. Klaučo, T. Haniš, and M. Hromčik, "Driving envelope definition and envelope protection using model predictive control," in *2020 American Control Conference (ACC)*, IEEE, 2020, pp. 4875–4880.

[49] D. Vošahlík and T. Haniš, "Traction control allocation employing vehicle motion feedback controller for four-wheel-independent-drive vehicle," *IEEE Transactions on Intelligent Transportation Systems*, vol. 24, no. 12, pp. 14 570–14 579, 2023.

[50] F. Borrelli, A. Bemporad, and M. Morari, *Predictive control for linear and hybrid systems*. Cambridge University Press, 2017.

[51] M. Herceg, M. Kvasnica, C. N. Jones, and M. Morari, "Multi-parametric toolbox 3.0," in *2013 European Control Conference (ECC)*, IEEE, 2013, pp. 502–510.

[52] P. Zegelaar and H. Pacejka, "Dynamic tyre responses to brake torque variations," *Vehicle System Dynamics*, vol. 27, no. S1, pp. 65–79, 1997.

[53] D. Q. Mayne, J. B. Rawlings, C. V. Rao, and P. O. Scokaert, "Constrained model predictive control: Stability and optimality," *Automatica*, vol. 36, no. 6, pp. 789–814, 2000.

[54] J. M. Maciejowski, *Predictive Control with Constraints*. PEARSON Prentice-Hall, 2002.

[55] IPG Automotive GmbH. "Carmaker official website." (2024), [Online]. Available: `https://ipg-automotive.com/en/products-solutions/software/carmaker/`.

[56] H. J. Ferreau, C. Kirches, A. Potschka, H. G. Bock, and M. Diehl, "qpOASES: A parametric active-set algorithm for quadratic programming," *Mathematical Programming Computation*, vol. 6, no. 4, pp. 327–363, 2014.

[57] D. Efremov. "Source-code of the driving envelope protection and environmental envelope protection algorithms and carmaker projects used for tests." (2024), [Online]. Available: `https://github.com/SDS-RC-FEE-CTU-in-Prague`.

[58] SDS, FEE, CTU in Prague. "Smart Driving Solution's YouTube channel." (2024), [Online]. Available: `https://www.youtube.com/@smartdrivingsolutions3633`.

[59] M. Bahnik, D. Filyo, D. Pekarek, *et al.*, "Visually assisted anti-lock braking system," in *2020 IEEE Intelligent Vehicles Symposium (IV)*, IEEE, 2020, pp. 1219–1225.

[60] M. Mondek and M. Hromčık, "Linear analysis of lateral vehicle dynamics," in *2017 21st International Conference on Process Control (PC)*, IEEE, 2017, pp. 240–246.

[61] D. Efremov, T. Haniš, and M. Klaučo, "Haptic driver guidance for lateral driving envelope protection using model predictive control," in *2020 IEEE Intelligent Vehicles Symposium (IV)*, IEEE, 2020, pp. 1992–1997.

[62] "Passenger cars — Test track for a severe lane-change maneuver — Part 1: Double lane-change," International Organization for Standardization, Geneva, CH, Standard, Dec. 2018.

[63] N. Tekles, J. Chongvisal, E. Xargay, *et al.*, "Design of a flight envelope protection system for NASA's transport class model," *Journal of Guidance, Control, and Dynamics*, vol. 40, no. 4, pp. 863–877, 2017.

[64] D. Efremov, Y. Zhyliaiev, B. Kashel, and T. Haniš, "Lateral driving envelope protection using cascade control," in *2021 21st International Conference on Control, Automation and Systems (ICCAS)*, IEEE, 2021, pp. 1440–1446.

[65] D. Efremov, T. Haniš, and M. Klaučo, "Wheel-centric protection: A paradigm shift in vehicle safety with low-level wheel trajectory control," *sumbitted to IEEE Transactions on Intelligent Transportation Systems*, 2024.

[66] S. Singh, "Critical reasons for crashes investigated in the national motor vehicle crash causation survey," National Highway Traffic Safety Administration, Tech. Rep., 2015.

[67] B. Olofsson and L. Nielsen, "Using crash databases to predict effectiveness of new autonomous vehicle maneuvers for lane-departure injury reduction," *IEEE Transactions on Intelligent Transportation Systems*, vol. 22, no. 6, pp. 3479–3490, 2020.

[68] D. Schreiber, B. Alefs, and M. Clabian, "Single camera lane detection and tracking," in *Proceedings. 2005 IEEE Intelligent Transportation Systems, 2005.*, IEEE, 2005, pp. 302–307.

[69] X. Yu and M. Marinov, "A study on recent developments and issues with obstacle detection systems for automated vehicles," *Sustainability*, vol. 12, no. 8, p. 3281, 2020.

[70] R. Madli, S. Hebbar, P. Pattar, and V. Golla, "Automatic detection and notification of potholes and humps on roads to aid drivers," *IEEE Sensors Journal*, vol. 15, no. 8, pp. 4313–4318, 2015.

[71] N. Camilleri and T. Gatt, "Detecting road potholes using computer vision techniques," in *2020 IEEE 16th International Conference on Intelligent Computer Communication and Processing (ICCP)*, IEEE, 2020, pp. 343–350.

[72] C. H. Yang, J. G. Kim, and S. P. Shin, "Road hazard assessment using pothole and traffic data in South Korea," *Journal of Advanced Transportation*, vol. 2021, pp. 1–10, 2021.

[73] C.-W. Kuan, W.-H. Chen, and Y.-C. Lin, "Pothole detection and avoidance via deep learning on edge devices," in *2020 International Automatic Control Conference (CACS)*, 2020, pp. 1–6.

[74] G. Raja, S. Anbalagan, S. Senthilkumar, K. Dev, and N. M. F. Qureshi, "SPAS: Smart pothole-avoidance strategy for autonomous vehicles," *IEEE Transactions on Intelligent Transportation Systems*, vol. 23, no. 10, pp. 19 827–19 836, 2022.

[75] D. Vosahlik, J. Cech, T. Hanis, *et al.*, "Self-supervised learning of camera-based drivable surface friction," in *2021 IEEE International Intelligent Transportation Systems Conference (ITSC)*, IEEE, 2021, pp. 2773–2780.

[76] J. Cech, T. Hanis, A. Kononisky, T. Rurtle, J. Svancar, and T. Twardzik, "Self-supervised learning of camera-based drivable surface roughness," in *2021 IEEE Intelligent Vehicles Symposium (IV)*, IEEE, 2021, pp. 1319–1325.

[77] D. Schramm, M. Hiller, and R. Bardini, *Vehicle dynamics, Modeling and Simulation*. Springer, 2014.

[78] J. Liu, P. Jayakumar, J. L. Stein, and T. Ersal, "Combined speed and steering control in high-speed autonomous ground vehicles for obstacle avoidance using model predictive control," *IEEE Transactions on Vehicular Technology*, vol. 66, no. 10, pp. 8746–8763, 2017.

[79] F. Cosimi, P. Dini, S. Giannetti, M. Petrelli, and S. Saponara, "Analysis and design of a non-linear MPC algorithm for vehicle trajectory tracking and obstacle avoidance," in *Applications in Electronics Pervading Industry, Environment and Society: APPLEPIES 2020 8*, Springer, 2021, pp. 229–234.

[80] M. Brezak and I. Petrović, "Real-time approximation of clothoids with bounded error for path planning applications," *IEEE Transactions on Robotics*, vol. 30, no. 2, pp. 507–515, 2013.

[81] D. A. Schwartz, "Clothoid road geometry unsuitable for sensor fusion clothoid parameter sloshing," in *IEEE IV 2003 Intelligent Vehicles Symposium*, IEEE, 2003, pp. 484–488.

[82] K. Liu, H. Wang, Y. Fu, G. Wen, and B. Wang, "A dynamic path-planning method for obstacle avoidance based on the driving safety field," *Sensors*, vol. 23, no. 22, p. 9180, 2023.

[83] J. Ji, A. Khajepour, W. W. Melek, and Y. Huang, "Path planning and tracking for vehicle collision avoidance based on model predictive control with multiconstraints," *IEEE Transactions on Vehicular Technology*, vol. 66, no. 2, pp. 952–964, 2016.

[84] A. Rezaeian, A. Khajepour, W. Melek, S.-K. Chen, and N. Moshchuk, "Simultaneous vehicle real-time longitudinal and lateral velocity estimation," *IEEE Transactions on Vehicular Technology*, vol. 66, no. 3, pp. 1950–1962, 2016.

[85] R. B. GmbH, *Bosch Automotive Handbook*. Wiley, 2018.

[86] J. A. E. Andersson, J. Gillis, G. Horn, J. B. Rawlings, and M. Diehl, "CasADi – A software framework for nonlinear optimization and optimal control," *Mathematical Programming Computation*, vol. 11, no. 1, pp. 1–36, 2019.

[87] A. Wächter and L. T. Biegler, "On the implementation of an interior-point filter line-search algorithm for large-scale nonlinear programming," *Mathematical programming*, vol. 106, pp. 25–57, 2006.

[88] I. S. Duff and J. K. Reid, *MA27-a set of Fortran subroutines for solving sparse symmetric sets of linear equations*. UKAEA Atomic Energy Research Establishment, 1982.

Appendix A

List of publications

This chapter presents a list of the author's publications and patents that are connected to this study.

Journal Publications

Vehicle and wheels stability defined using driving envelope protection algorithm in *IEEE Transactions on Intelligent Transportation Systems (IF = 8.5)*. Citations in Google Scholar **0** | WoS **0** | Scopus **0**.

Conference Papers

Introduction of driving envelope and full-time-full-authority control for vehicle stabilization systems in *22nd International Conference on Process Control (PC19)*. Citations in Google Scholar **17** | WoS **5** | Scopus **6**.

Driving envelope definition and envelope protection using model predictive control in *2020 American Control Conference (ACC)*. Citations in Google Scholar **10** | WoS **4** | Scopus **5**.

Haptic driver guidance for lateral driving envelope protection using model predictive control in *2020 IEEE Intelligent Vehicles Symposium (IV)*. Citations in Google Scholar **4** | WoS **3** | Scopus **3**.

Lateral driving envelope protection using cascade control in *2021 21st International Conference on Control, Automation and Systems (ICCAS)*. Citations in Google Scholar **2** | WoS **0** | Scopus **0**.

Driving envelope: On vehicle stability through tire capacities in *2022 IEEE Intelligent Vehicles Symposium (IV)*. Citations in Google Scholar **2** | WoS **0** | Scopus **0**.

Submitted Papers

Wheel-centric protection: a paradigm shift in vehicle safety with low-level wheel trajectory control submitted to *IEEE Transactions on Intelligent Transportation Systems (IF = 8.5)* in 2024.

Filled Patents

Methods and systems for calculating control variables of a vehicle, EPO No. *EP22207286*, filed November 14, 2022.

Method and apparatus for driver assistance of a moving vehicle, EPO No. *EP23182777*, filed June 30, 2023.